Departamento de
Ingeniería Mecánica
Universidad de Concepción

Analytical Solution for Optimal Stiffness and Damping for Comfort and Road-Holding in the Half Car Model

Por

Haidar Manuel Gutiérrez Burgos

Tesis presentada a la Facultad de Ingeniería de la Universidad de Concepción para optar al grado de Magíster en Ciencias de la Ingeniería con Mención en Ingeniería Mecánica

Profesor Guía:
PhD Felix Leaman Weiffenbach

Agosto 2025
Concepción, Chile

ACKNOWLEDGEMENTS

Este trabajo es el resultado de un largo camino recorrido, y hay muchas personas sin las cuales nunca habría sido posible alcanzar esta meta. En primer lugar, mi más profundo agradecimiento a mis padres. Su apoyo incondicional, motivación y sacrificio durante estos seis años han sido el pilar fundamental que me ha sostenido en cada etapa de mi formación académica. Cada logro es también suyo.

A mis amigos de la universidad, los "watones mecánica" —Nico, JP, Vale, Capi y Benk—, les agradezco infinitamente por todas las noches de estudio, risas y momentos compartidos. Los recuerdos que construimos juntos son un tesoro que llevaré siempre conmigo.

También a mis compañeros del *FIRT* -Guss, Nico, Joaco, Alonso, Felipe, Jota, Max, Jorge y Rodolfo-, quienes hicieron de mi último año universitario una experiencia extraordinaria, permitiendome incluir uno de mis hobbies personales dentro de mi vida universitaria.

Por último, un agradecimiento especial a los profesores guía de este trabajo, Felipe y Bernardo. A Felipe, por no dejarme rendir, siempre proponiendo ideas para sacar adelante esta investigación. A Bernardo, por ser un excelente guía y docente, respondiendo mis dudas a cualquier hora. No puedo imaginar haber realizado este trabajo sin su apoyo.

Dedicada a mis padres y a todos los que formaron parte de este viaje.

Resumen

Esta investigación explora el análisis de covarianza en el Modelo de Medio Vehículo (*HCM*) para derivar parámetros óptimos de suspensión que maximicen, por separado, el confort y la adherencia. Se modelan las irregularidades del camino como perturbaciones de ruido blanco Gaussiano, excluyendo acciones del conductor y eventos discretos.

La investigación comienza reproduciendo técnicas existentes de optimización de la suspensión para el Modelo de Cuarto de Vehículo (*QCM*, por sus siglas en inglés) utilizando análisis tanto en el dominio del tiempo como en el dominio de la frecuencia. Estos enfoques complementarios producen expresiones analíticas idénticas para parámetros óptimos enfocados en adherencia y confort.

Posteriormente, la investigación extiende estas metodologías analíticas al Modelo de Medio Vehículo de un solo eje, incorporando explícitamente una barra estabilizadora como elemento de interconexión. Esta extensión da como resultado expresiones analíticas para los indicadores de rendimiento y coeficientes óptimos de la suspensión. Las ecuaciones derivadas ilustran explícitamente la influencia de la barra estabilizadora, demostrando que los parámetros de la suspensión deben optimizarse considerando las rotaciones angulares del chasis. Se identifican desviaciones significativas en los parámetros óptimos en comparación con soluciones más simples del *QCM*, lo que resalta la necesidad de tener en cuenta la dinámica del chasis incluso en escenarios sin barra estabilizadora.

Para el *HCM* de dos ejes, se adoptan métodos numéricos debido a la complejidad analítica, especialmente por la correlación con desfase de tiempo. Los resultados revelan configuraciones óptimas asimétricas dependientes de la velocidad, incluso en vehículos simétricos. Un análisis de sensibilidad destaca que la estimación precisa de parámetros impacta más que la modelación del desfase.

Este análisis integral supera las limitaciones de modelos simplificados e introduce metodologías avanzadas para optimizar el diseño de suspensiones en términos de confort y adherencia.

Palabras clave: Confort de marcha, Adherencia al camino, Barra estabilizadora, Modelo de Medio Vehículo, Optimización de suspensiones

Abstract

This research explores covariance analysis applied to the Half Car Model (Half Car Model (HCM)) to derive optimal suspension parameters that independently maximize comfort and road-holding. By characterizing road irregularities as continuous Gaussian white noise disturbances, and excluding driver inputs and discrete events, the study aims to characterize the system's response to these excitations.

The research begins by reproducing existing suspension optimization techniques for the Quarter Car Model (QCM) using both time-domain and frequency-domain analyses. These complementary approaches yield consistent analytical expressions for optimal parameters targeting road holding and comfort.

Subsequently, the investigation extends these analytical methodologies to the single-axle Half Car Model, explicitly incorporating an anti-roll bar as an interconnecting element. This extension results in analytical expressions for performance indicators and optimal suspension parameters. The derived equations explicitly illustrate the anti-roll bar's influence, demonstrating that suspension parameters must be optimized with consideration of roll dynamics. Notably, significant deviations in optimal parameters are identified compared to simpler QCM solutions, underscoring the necessity of accounting for chassis dynamics even in scenarios without an anti-roll bar.

For the two-axle Half Car Model, the complexity of analytically deriving optimal solutions required the adoption of numerical approaches, especially due to correlated and time-delayed road inputs. Optimal suspension configurations are evaluated across various scenarios, revealing asymmetric optimal parameters contingent upon vehicle speed, even in symmetrical vehicle setups. A sensitivity analysis further emphasizes that precise parameter estimation significantly influences suspension performance, potentially surpassing the impact of model complexity.

This comprehensive analysis addresses limitations inherent in simplified suspension models and presents advanced methodologies to optimize vehicle suspension systems, offering substantial improvements in design strategies for ride comfort and road holding.

Keywords: ride comfort, road holding, anti roll bar, Half Car Model, suspension optimization

Contents

List of Figures

List of Tables

Chapter 1

Introduction

The suspension of a vehicle serves two main functions. Firstly, it must isolate the chassis from terrain irregularities, which is known as comfort or *ride comfort*. Secondly, it must ensure an efficient connection between the road and the wheel, to maintain maneuverability, a concept known as adherence or *road holding* Milliken & Milliken (1994). Achieving a balance between these two objectives, comfort and adherence, is a significant challenge. Its complexity lies in the fact that it is mathematically impossible to optimize both objectives simultaneously, as they require different levels of stiffness and damping, making it necessary to find a compromise between them Guiggiani (2014).

The optimization of suspensions refers to adjusting the stiffness and damping values of the system to increase the suspension's performance based on comfort and adherence metrics. The most common and studied model for vehicle suspensions is the Quarter Car Model (QCM) Jazar (2008). This model represents a quarter of the vehicle through a two Degrees of Freedom (oF) system, as shown in Figure 1.1 Wang et al. (2017). The QCM provides a fundamental basis for the analysis and design of suspension systems, allowing for an estimation of comfort and adherence performance. It emerges as a response to the need to study both the vertical accelerations of the chassis, to quantify comfort, and the relative displacement between the wheel and the road, to quantify adherence.

Regarding the use of metrics to evaluate comfort and adherence, driver comfort is closely related to the vertical accelerations of the chassis, so the vertical accelerations of the chassis

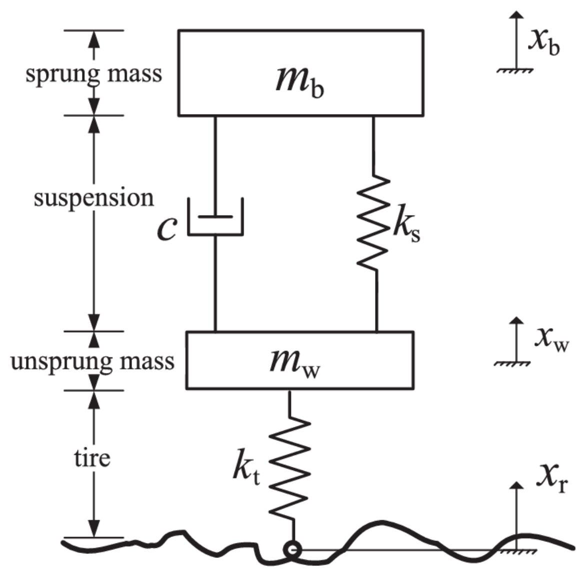

Figure 1.1: Quarter Car Model with lumped parameters Wang et al. (2017). The notation used in the figure corresponds to that of the referenced source.

are a representative magnitude of comfort ISO (1997). On the other hand, adherence depends on the normal contact forces in the tires, so adherence is generally evaluated through the variation of the normal tire force, due to the unfavorable behavior of tires under transient conditions.

To quantify these magnitudes, various indices have been proposed. For example, for adherence, some authors use the peak value of the normal tire force Segers (2014), others use the standard deviation Gobbi et al. (1999b, 2005), and the most commonly used is the Root Mean Square (RMS) value Milliken & Milliken (1994); Scheibe & Smith (2009); Limebeer & Massaro (2018); Georgiou et al. (2007); Baumal et al. (1998). Among these authors, the work of Scheibe & Smith (2009) and GOBBI & MASTINU (2001) stands out, where they develop analytical expressions that allow minimizing these indicators (consequently maximizing performance), in other words, their study provides equations that enable the optimization of the QCM for any vehicle based on the system's lumped parameters.

Despite its utility, the QCM has three inherent limitations. Primarily, as a two oF vertical model, it cannot capture the angular dynamics of the chassis—specifically roll and pitch motions—which significantly influence both comfort and road holding Kaldas & Soliman (2014). Second, the QCM has only a single input, overlooking any correlation between the road irregularities affecting different wheels of the vehicle. Finally, the QCM framework is structurally incapable of incorporating suspension interconnection elements, such as anti-roll bars, which connect left and right suspensions of an axle, resulting in semi-dependent suspension behavior Zhang et al. (2010).

The anti-roll bar (ARB) is a widely used mechanical components that mitigate the vehicle's body roll during cornering or over uneven surfaces Ramakrishna et al. (2017). They resist differences in vertical motions of the wheels by torsionally linking opposite suspension arms, generating a resisting roll moment that reduces roll, which improves handling and stability when properly tuned Le & Pieper (2014). Their primary advantage lies in offering significant roll stiffness without requiring overly stiff main suspension springs, preserving ride comfort under straight-line driving Lu et al. (2024).

Traditional analytical design approaches for anti-roll bars often recommend achieving a target vehicle roll gradient during cornering or establishing a desired front-to-rear roll couple distribution to influence handling balance Milliken & Milliken (1994); Segers (2014); Pütz & Serné (2022); Trzesniowski (2023); Frömmig (2023). In such methodologies, springs and dampers are often selected independently based on QCM analysis. This reveals a clear opportunity to improve upon existing design guidelines by developing an integrated approach that incorporates the ARB's influence within a representative model of the vehicle's suspension.

To address this limitation, the QCM has been extended to the Half Car Model (HCM), as shown in Figure 1.2, and to the Full Car Model (FCM). These models allows the incorporation of chassis roll and pitch motions, as well as the possibility of including interconnection elements. While optimization studies do exist, they predominantly rely on numerical techniques Le & Pieper (2014), such as Particle Swarm Optimization Drehmer et al. (2015); Yaghoubi & Ghanbarzadeh (2024) and genetic algorithms applied to specific vehicles Bideleh et al. (2016); Tan et al. (2022); Zhao et al. (2016). Although these methods yield conclusive results, they cannot be readily generalized to other vehicles because the relationship between suspension parameters and performance is not expressed explicitly—an inherent drawback of purely numerical approaches. Consequently, to establish general suspension design guidelines within the HCM framework, an analytical solution is essential.

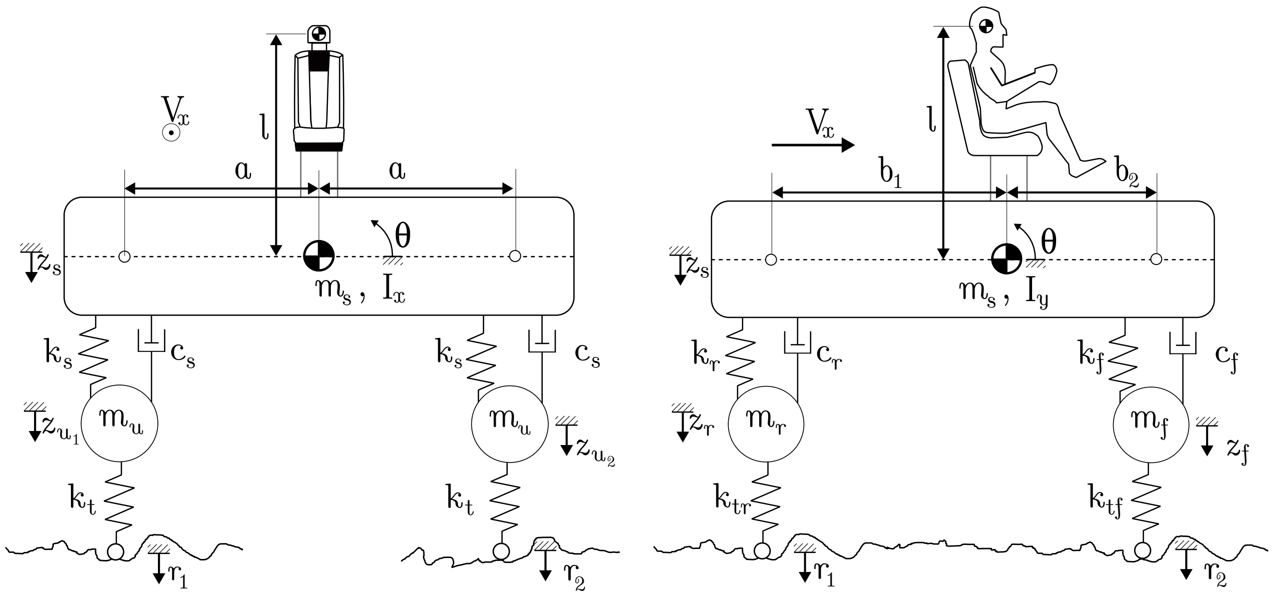

(a) Half Car Model for a single axle, with uncorrelated inputs.

(b) Half Car Model for two axles, with correlated inputs.

Figure 1.2: Representative schematic of the HCM for modeling one or both axles of the vehicle, the nomenclature is detailed on Chapter 4. The model allows for the analysis of vertical and angular dynamics under two types of disturbances, either correlated or uncorrelated (r_1 and r_2).

Investigation gap

In multi-degree-of-freedom models applicable to four-wheeled vehicles, no methodology or analytical expression has been developed to compute the optimal suspension stiffness and damping values while taking into account an interconnection element, based on the vehicle's lumped parameters and the statistical correlation of road excitations.

Proposal

This work proposes a comprehensive framework for vehicle suspension optimization using the Half Car Model HCM, which will be analyzed in both single-axle and two-axle configurations.

Initially, the single-axle HCM is employed to derive analytical expressions for the optimal suspension stiffness and damping. This analysis explicitly accounts for the influence of the anti-roll bar (ARB) and aims to independently optimize comfort and road-holding under uncorrelated road inputs. Subsequently, the study extends to the more complex two-axle HCM to investigate the effects of time-correlated road inputs and pitch dynamics. Due to the analytical intractability of this configuration, a numerical optimization approach is adopted. To provide a quantitative reference for the solutions, the results from both HCM analyses will be systematically compared against the baseline optima derived from the simpler QCM

1.1 Objectives

1.1.1 General Objectives

Develop closed-form expressions for the optimal stiffness and damping coefficients for comfort and road holding in the Half Car Model (HCM), based on vehicle parameters and road characteristics.

1.1.2 Specific Objectives

SO1: Mathematically adapt the single axle HCM with four degrees of freedom to enable the analytical study of the oscillatory behavior of interconnected suspension systems.

SO2: Establish performance metrics and formulate analytical expressions to quantify ride comfort and road holding, based on the system's lumped parameters, within both single-axle and two-axle HCM configurations.

SO3: Derive algebraic expressions to calculate the optimal suspension stiffness and damping coefficients, incorporating an interconnection element, in the single-axle HCM, aiming to independently maximize ride comfort and road holding performance.

SO4: Conduct a numerical study to evaluate the optimal suspension stiffness and damping parameters in the two-axle HCM with independent suspension systems, with the objective of independently maximizing ride comfort and road holding performance.

1.2 Hypothesis

Analytical suspension design guidelines in the HCM are necessary to provide foundations for anti-roll bar design akin to those provided by the QCM in standard passive suspensions.

1.3 Methodology

Mathematically adapt the single axle HCM with four degrees of freedom to enable the analytical study of the oscillatory behavior of interconnected suspension systems

Based on the illustrations shown in Figure 1.2, two half-vehicle models are proposed: one with a single axle and another with two axles. Both models will feature four degrees of freedom, two for the vertical displacements of the wheels, and two for the vertical and angular motion of the chassis. In the single-axle model, an anti-roll bar will be assumed to act as the interconnection element providing stiffness. In contrast, the two-axle model will assume independent suspensions without interconnection.

Only excitations due to road irregularities will be analyzed, excluding driver-induced inputs. According to the reviewed literature, the road profile will be modeled as a white noise stochastic process. Regarding the correlation between irregularities r_1 and r_2, and in accordance with Popp & Schiehlen (2010), uncorrelated inputs will be assumed for the single-axle HCM, whereas correlated inputs with a time delay will be considered for the two-axle model.

To derive the equations of motion, lumped parameter models will be used with ideal elements for suspension stiffness and damping, and an ideal stiffness anti-roll bar in the interconnected suspension configuration. Small displacements will be assumed to preserve system linearity. Additionally, installation ratios will be embedded within the lumped stiffness and damping parameters, in order to avoid unnecessarily complicating the equations.

Given the analytical complexity of the Half Car Model, this research begins by revisiting the Quarter Car Model to replicate established methodologies for comfort and road-holding optimization. This step serves both as a benchmark and a foundation for the subsequent development of the more complex single-axle and two-axle HCM.

Establish performance metrics and formulate analytical expressions to quantify ride comfort and road holding, based on the system's lumped parameters, within both single-axle and two-axle HCM configurations

First, the definitions of performance indices, such as P_{C_2} for comfort and P_{N_2} for road holding previously used by Lot & Sadauckas (2021) in the QCM, will be adapted and extended for the HCM configurations. The ride comfort metric denoted as J_1, will be defined as the Root Mean Square (RMS) value of the net acceleration experienced at the driver's head location Standarization (2001). This calculation accounts for the effects of both vertical displacement and pitch rotation of the sprung mass. Concurrently, the road holding metric, denoted as J_2, will be quantified as RMS value of the combined dynamic load variation exhibited by both wheels on the road surface.

These objective functions (J_1 and J_2) will be derived using covariance analysis Müller & Schiehlen (2012). This methodology necessitates solving the algebraic Lyapunov equation to determine the state covariance matrix ($\mathbf{P_x}$). The covariance matrix encapsulates information regarding the statistical dispersion (variances and covariances) of the system's states when subjected to stochastic road profile inputs. Subsequently, the RMS values corresponding to the objective functions (J_1, J_2) are computed from the elements of the covariance matrix ($\mathbf{P_x}$) through the application of specific weighting vectors (output matrices), as detailed in Wijker (2009).

The strategy for solving the Lyapunov equation will vary depending on the model's complexity. For the single-axle HCM, an analytical approach, facilitated by the symbolic computation software Maple, will be employed. Conversely, due to the increased complexity inherent in the two-axle HCM, a numerical approach will be adopted to solve its respective Lyapunov equation. With respect to the solution method, although Müller & Schiehlen (2012) describes three approaches, including the polynomial matrix method employed in that study, this research adopts the direct method. This technique reformulates the Lyapunov matrix equation, which has order $n = 8$ in the single-axle HCM, into an equivalent system of $n(n+1)/2 = 36$ linear algebraic equations. These equations are then solved simultaneously to obtain the unique elements of the symmetric state covariance matrix P_x.

Derive algebraic expressions to calculate the optimal suspension stiffness and damping coefficients, incorporating an interconnection element, in the single-axle HCM, aiming to independently maximize ride comfort and road holding performance

Using the gradient of each objective function, two separate single-objective optimizations—one for comfort and another for road holding—will be conducted to derive the analytical expressions for the optimal suspension stiffness ($k_s^\star$) and damping ($c_{s,}^\star$) coefficients for the single-axle Half Car Model incorporating an anti-roll bar. These expressions correspond to the parameters that independently minimize the ride comfort J_1 and road holding J_2 objective functions, respectively. The resulting optimal parameters will be explicit functions of the vehicle's lumped parameters (m_u, m_s, I_x, a, k_t) as well as the stiffness of the selected anti-roll bar (k_r as defined in Chapter 4).

The relationship between the optimal parameters derived from this HCM analysis and those obtained from the simpler QCM will be investigated in detail. This comparison aims to characterize the deviation of the proposed model's optima from the baseline QCM results and to specifically isolate the effect of incorporating the anti-roll bar on these optimal suspension settings.

Furthermore, the impact of including the anti-roll bar on the actual performance indicators will be characterized. While the detrimental effect on comfort is well documented in the literature, the specific quantitative effect on road holding under these conditions—a topic less explored—will also be analyzed based on the derived expressions.

Additionally, the inherent trade-off between the comfort and road holding objectives will be addressed through the concept of the Pareto front. This analysis will highlight the mathematical impossibility of simultaneously achieving the absolute minimum for both performance metrics with a single set of passive suspension parameters (k_s, c_s).

Conduct a numerical study to evaluate the optimal suspension stiffness and damping parameters in the two-axle HCM with independent suspension systems, with the objective of independently maximizing ride comfort and road holding performance

For the two-axle Half-Car Model, the Lyapunov equation will be solved numerically, leveraging the covariance analysis framework established earlier. This analysis will focus on a configuration employing independent suspension systems at both axles. The same optimization model will be maintained for this case. The primary goal is to characterize the deviation of the optimal suspension parameters (k_s, c_s) obtained from this more complex model compared to the baseline optima derived from the QCM. Furthermore, the results will be interpreted to potentially corroborate practical suspension design recommendations.

Regarding the correlation between the road profile inputs experienced by the front and rear axles, two distinct scenarios will be investigated. The first scenario assumes simultaneous and identical disturbances at both axles (zero time delay), approximating conditions encountered during high-speed driving where the time lag between axle excitations is negligible. The second scenario incorporates an exact model of the time delay based on the vehicle's wheelbase and speed, enhancing the model's representativeness, albeit at the cost of increased mathematical complexity in the input modeling.

Finally, a sensitivity analysis is proposed. This analysis aims to provide a quantitative assessment comparing the relative importance of two factors: first, the accuracy of the estimated lumped parameters used in the model (e.g., masses, inertias, stiffnesses), and second, the impact of employing a more sophisticated mathematical model (the two-axle HCM) versus the simpler QCM. The goal is to understand whether potential inaccuracies in parameter estimation or the choice of model fidelity has a greater influence on the predicted optimal suspension design and performance outcomes.

1.4 Gantt Chart

The Gantt chart corresponding to the project's organization is attached below **Not updated**.

			Meses									
Objetivo	Actividad	Resultado esperado	1	2	3	4	5	6	7	8	9	10
OE1	Replicar parte del estado del arte para el *QCM*	Bases matemáticas para el estudio de suspensiones interconectadas	x									
	Construir un *HCM* con 4 grados de libertad y diferentes tipos de correlación en las perturbaciones			x								
	Derivar ecuaciones del movimiento y formulación espacio estado del sistema			x								
OE2	Extrapolar indicadores de confort y adherencia del *QCM* al HCM.	Excpresiones algebraicas para los indicadores de desempeño de la suspensión en el *HCM*			x							
	Aplicar análisis de covarianza y definir vectores de ponderación para los indicadores				x							
	Resolver analíticamente la ecuación de Lyapunov utilizando Maple				x	x						
OE3	Derivar los coeficientes óptimos de la suspensión para un caso con suspensiones independientes	Excpresiones algebraicas para los coeficientes óptimos en el *HCM*					x					
	Derivar los coeficientes óptimos de la suspensión para un caso con suspensiones interconectadas						x					
	Comparar aumento en el desempeño utilizando optimos del *QCM* vs *HCM*						x					
OE4	Parametrizar un vehículo en específico en CarMaker.	Verificar la representatividad y efectividad del modelo propuesto.						x				
	Construir camino con sinusoidales de distinta longitud de onda entre 0.5 y 20 [Hz]							x				
	Comparar el desempeño utilizando los óptimos del *QCM* vs los propuestos en esta investigacion.							x				
Redacción	Redacción de Tesis	Exponer resultados de forma clara y publicable							x	x	x	
	Redacción de artículo científico											x

Figure 1.3: Work plan not updated.

1.5 Chapter Layout

To familiarize the reader with the organization of the content, the chapter layout is described as follows: each chapter, excluding the introduction, begins with an italicized section summarizing the topics covered and the chapter's objective within the context of this research. At the end of each chapter, a summary recaps the main points discussed.

Chapter 2 establishes the theoretical framework, presenting the mathematical properties used to characterize road profiles and introducing two mathematical methods—spectral analysis and covariance analysis—employed to describe the system's response. These tools provide the foundation for the subsequent development of analytical and numerical models.

Chapter 3 formally introduces the Quarter Car Model (QCM), deriving analytical expressions for the comfort and road-holding indicators through both time-domain and frequency-domain analyses. This chapter sets the stage for understanding the behavior of vehicle suspensions using a simplified, two-degree-of-freedom model. Chapter 4 presents the single-axle Half Car Model HCM, defines its performance indicators, and develops an analytical framework for vehicles with either independent suspensions or interconnected suspension elements such as anti-roll bars, showing their influence in the optimal suspension.

Chapter 5 carries out a numerical analysis of the two-axle HCM, determining optimal suspension parameters under the assumption of time-delayed correlated road inputs. Finally, Chapter 6 presents the conclusions and outlines directions for future research.

Chapter 2

Theoretical framework

This chapter presents the theoretical foundations that underpin the analysis carried out in this investigation. First, the mathematical description of road profile, which is the model excitation, is introduced. Next, the performance indicators commonly used in the literature are described, along with their corresponding physical interpretations. Finally, the the spectral and covariance analyses are detailed which enable the study of the vehicle's response to any road profile, aiming to justify the developments presented in the next's chapters.

2.1 Road characterization

To optimize the system's performance, it is essential to first characterize the inputs or disturbances acting on it. In this research, driver inputs (such as braking and cornering) and discrete disturbances (like potholes) are excluded. Instead, continuous road irregularities are considered exclusively, as these can be characterized by consistent properties over time, allowing various mathematical approaches to be applied.

The road irregularities are considered as a random input, which implies that no two road profiles are identical, reflecting a level of complexity and uncertainty to the problem. However, randomness does not mean that roads can have any profile. For the suspension model implemented in this research, as in many others, the road can be approximated using a one-dimensional analysis. where the **road profile** is defined as the irregularity or elevation (r) as a function of the distance traveled (x) over time (t) and at a given speed (v) Robson

& Kamash (1977). Figure 2.1 illustrates a road profile based on the ISO 8608 standard Standardization (1995).

$$r(x) = r(vt) \tag{2.1}$$

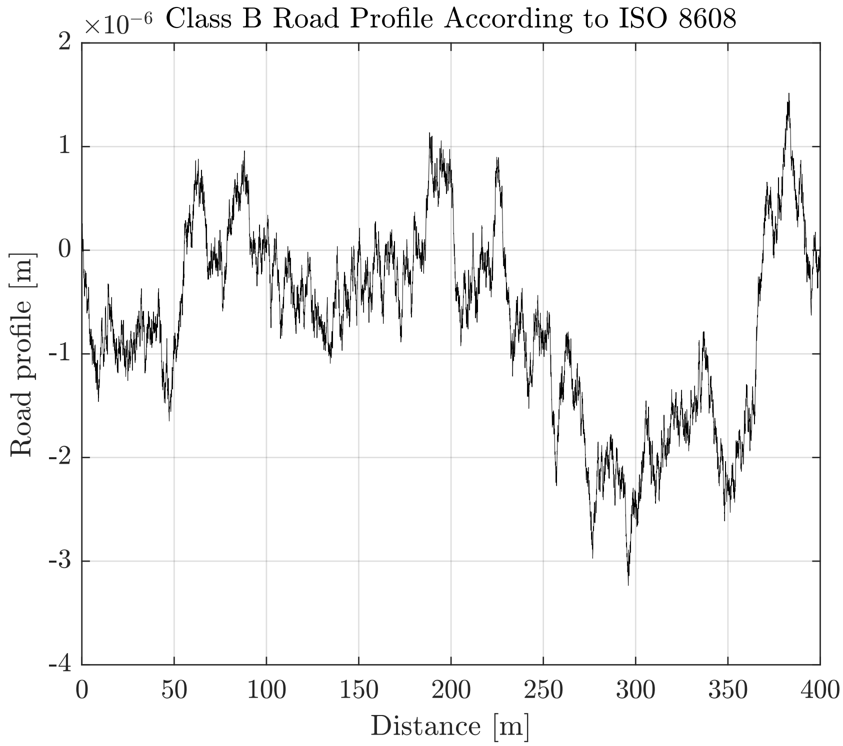

Figure 2.1: Random road profile of Class B, according to the ISO 8608 Standard.

In general, roads are also considered to be ergodic and stationary profiles. As a road becomes sufficiently long, it can be treated as a periodic process with a long period, which allows for frequency domain analysis using the Fourier transform. The Fourier transform enables the conversion of a road profile ($r(x)$) in the time domain to the **road spectrum** ($R(n)$) in the frequency domain, as follows:

$$R(n) = \int_{-\infty}^{+\infty} r(x) e^{-2i\pi n x}\, dx \tag{2.2}$$

One of the key characteristics of the road is its energy (E), which can be calculated in both the spatial and frequency domains, according to the following expression:

$$E = \int_{-\infty}^{+\infty} |r(x)|^2 \, dx = \int_{-\infty}^{+\infty} |R(n)|^2 \, dn = \int_{0}^{+\infty} 2|R(n)|^2 \, dn \tag{2.3}$$

It is important to note that, due to the properties of complex numbers, a symmetry condition is used, which is known as single-sided Energy Spectral Density (ESD). As mentioned earlier, since long roads will be considered, the energy of these will tend to infinity. To obtain a representative measure of road irregularities, the PSD is used, which corresponds to the energy per unit length. It is denoted as $\hat{G}_{dd}(n)$ and is measured in [m^2/cycles/m], as follows:

$$\text{PSD} = \lim_{L\to\infty} \left(\frac{1}{L} \int_{-L/2}^{L/2} |r(x)|^2 \, dx \right) = \int_{0}^{\infty} \hat{G}_{dd}(n) \, dn \tag{2.4}$$

In this way, the area under the curve of the PSD on a linear scale is equivalent to the power of the original signal within the frequency range considered. The importance of the PSD lies in the fact that roads are classified according to their PSD into eight categories, as outlined by the ISO 8608 standard Standardization (1995). This standard provides the following expression to define the limits of the octave bands used for classifying the road spectrum:

$$\hat{G}_{dd}(n) = \hat{G}_{d0} \left(\frac{n_0}{n} \right)^{-2} \tag{2.5}$$

Where $\hat{G}_{d0}$ is a constant that depends on the type of road, according to the standard, and n_0 is the reference frequency, set at $n_0 = 0.1$ [cycles/m]. Additionally, many authors use the circular spatial frequency or wave number Ω, expressed in [rad/m], which in turn has its own reference frequency, $\Omega_0 = 1$ [rad/m]. The variable change is shown below, while Table 1 presents the road classification for both types of frequency, and Figure 2.2 illustrates the spectrum of seven of the eight different road classes.

Additionally, the RMS of the road, according to the standard, is given by:

$$r_{\text{rms}}^2 = \int_{n_{\min}}^{n_{\max}} \hat{G}_{dd}(n) \, dn = \int_{\Omega_{\min}}^{\Omega_{\max}} G_{dd}(\Omega) \, d\Omega \tag{2.6}$$

Lastly, another important characteristic of the road is its rate of change ($\dot{r}(x)$). Differential operations in the time domain translate to simple multiplications in frequency domain. Thus,

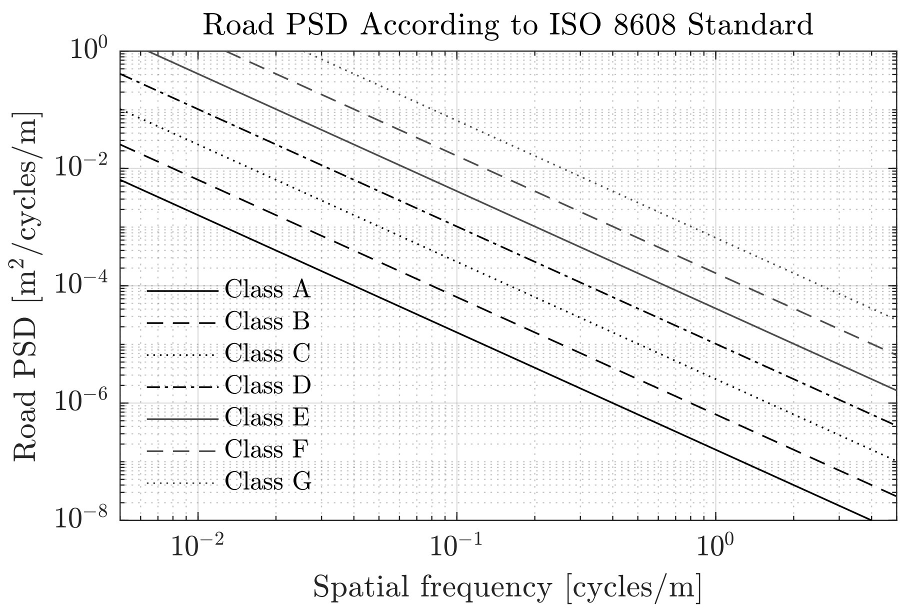

Figure 2.2: PSD of different road classes (A to G) according to the ISO 8608 Standard. This figure depicts the classification limits for roads, where each contour curve represents the upper boundary of the PSD of road roughness across a range of spatial frequencies. For example, roads with a PSD falling between the Class B and Class C contour lines, correspond to a Class C road.

the PSD of the road's rate of change is shown in Figure 2.3 and is given by:

$$G_{vv} = \Omega^2 G_{dd}(\Omega) = \Omega^2 G_{d0} \left(\frac{\Omega_0}{\Omega}\right)^2 = \Omega_0^2 G_{d0} \tag{2.7}$$

The change of variable between spatial and circular frequencies can be extrapolated for this definition. Analyzing equation (2.9), it is concluded that the PSD of the road's velocity is constant across all frequencies. In other words, the velocity of the external disturbance for a vehicle traveling on a road represented according to ISO 8608 at a constant traveling speed v is equivalent to a white noise input. This is a fundamental characteristic of the road for the frequency analysis presented in section **2.4** and for the remainder of the research.

2.2 Vehicle performance indices

To evaluate the performance of the suspension in relation to comfort and road holding requirements, it is essential to have metrics that quantify these objectives. On one hand, h!

Table 2.1: Simplified road classification based on ISO 8608 [17].

Road class	$r_{\text{rms}} = \sqrt{P}$ [mm]	G_{d0} $\left[\frac{\text{mm}^2}{\text{rad/m}}\right]$	G_{vv} $\left[\frac{\text{mm}}{\text{rad}}\right]$	$\hat{G}_{d0}$ $\left[\frac{\text{mm}^2}{\text{cycle/m}}\right]$	$\hat{G}_{vv}$ $\left[\frac{\text{mm}}{\text{cycle}}\right]$
A	4	1	0.001	16	0.006
B	8	4	0.004	64	0.025
C	15	16	0.016	256	0.101
D	30	64	0.064	1024	0.404
E	60	256	0.256	4096	1.617
F	120	1024	1.024	16384	6.47
G	250	4096	4.096	65536	25.84
H	500	16384	16.38	262144	103.49

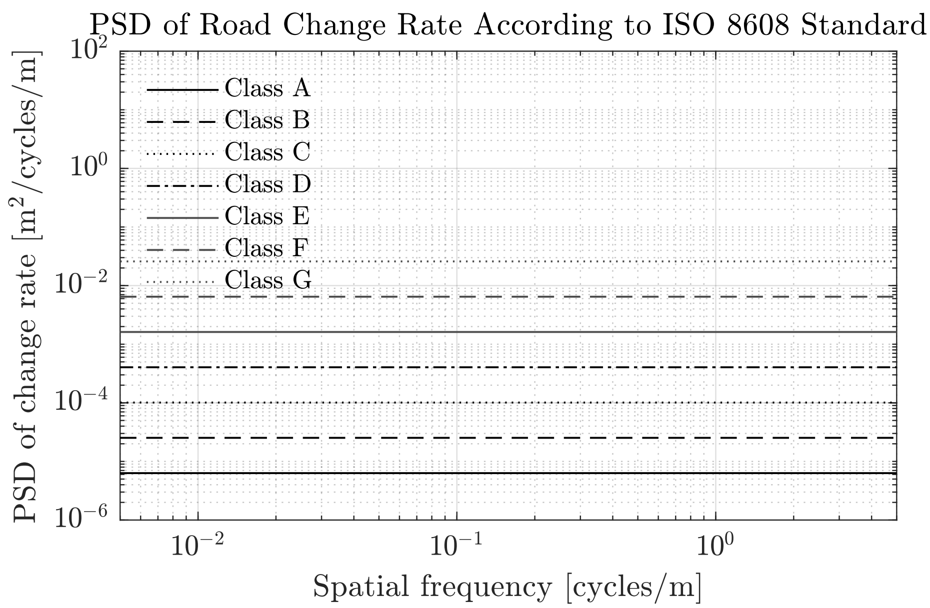

Figure 2.3: PSD of the road change rate for different road classes (A to G) according to the ISO 8608 Standard. The figure illustrates the variation in roughness change rate across spatial frequencies for each class, providing insights into the impact of road class on the rate of surface irregularities.

humans are highly sensitive to accelerations, and driver comfort is closely related to the accelerations experienced by the chassis. Therefore, it is logical to measure discomfort through the magnitude of accelerations. With this in mind, the discomfort indicator P_{C_2} is often assumed as the RMS value of the accelerations, given by:

$$P_{C_2} = \sqrt{\frac{1}{T}\int_0^T \left(a_x^2 + a_y^2 + a_z^2\right) dt} = \sqrt{\int_0^\infty \left(S_{xx}(\omega) + S_{yy}(\omega) + S_{zz}(\omega)\right) d\omega} \tag{2.8}$$

Where a_x, a_y, and a_z correspond to the three orthogonal components of acceleration in the time domain, while S_{xx}, S_{yy}, and S_{zz} are the PSDs corresponding to these accelerations in the frequency domain. In addition to the RMS value, other authors use different indicators derived from accelerations. For example, Georgiou et al. (2007) and Jonasson & Roos (2008) use the peak value of accelerations, while Gobbi et al. (2005) employs the standard deviation of this magnitude. However, the RMS value is the most commonly used, also referred to as the 2-norm of the system Green & Limebeer (2012).

Since the perception of accelerations varies with frequency, the ISO 2631-1 standard Standardization (1995) defines the indicator P_{C_2w}, which involves a frequency-based weighting of accelerations. Additionally, studies such as Gobbi et al. (1999b) have proposed indicators for the angular accelerations of roll and pitch, although no single indicator is used to combine longitudinal and angular accelerations.

On the other hand, road holding depends on the contact forces at the tires; generally, a higher normal force results in greater adhesion. However, due to the non-linearities and transient behavior of the tires, a high variation in contact force can translate into lower grip ref (2006). With this in mind, the usual adherence indicator P_{N_2} is the RMS value of the variation in tire normal force.

$$P_{N_2} = \sqrt{\frac{1}{T}\int_0^T \left[N(t) - N_0\right]^2 \, dt} = \sqrt{\int_0^\infty S_{nn}(\omega)\, d\omega} \tag{2.9}$$

Where $N(t)$ corresponds to the tire normal force, N_0 represents the mean force in the time domain, and S_{nn} is the PSD corresponding to the variation in normal force in the frequency domain. In addition to the RMS value, other authors use different indicators derived from this magnitude. For example, Segers (2014) uses the peak value of tire deflection (deflection is proportional to contact force), while Gobbi et al. (2005) and Gobbi et al. (1999a) employ the standard deviation of this quantity. Again, the RMS value is the most commonly used.

For this research, the indicators P_{C_2} and P_{N_2} defined in Lot & Sadauckas (2021) will be used as design objectives for the vehicle suspension. In a subsequent optimization process, the aim will be to minimize both the P_{C_2} and P_{N_2} indicators independently, process also known as single-objective optimization Karnopp (2013).

2.3 State equations of the system

2.3.1 Equation of motion

For the mathematical modeling of an oscillatory system, a set of differential equations is used to capture the dynamic behavior of the system. In particular, the mathematical relationships between the generalized coordinates of the system, along with their velocity and acceleration, are called equations of motion Limebeer & Massaro (2018). To model vehicle suspensions, a system known as mass-spring-damper with n oF is used. By assuming linear behavior and small displacements, the following general expression for the equations of motion is obtained:

$$M\ddot{x}(t) + C\dot{x}(t) + Kx(t) = F_0 f(t) \tag{2.10}$$

Where $x(t)$ is the displacement vector of dimensions $(n \times 1)$; M, C, and K correspond to the mass, damping, and stiffness matrices for lumped parameters, respectively, with dimensions $(n \times n)$. On the other hand, $F(t) = F_0 f(t)$ is the vector of external forces applied to the system, with dimensions $(n \times 1)$. For this research, linear behavior will be assumed, although not necessarily uncoupled Slotine & Li (1991).

2.3.2 State-space modeling

The state-space representation is a compact and convenient way to model systems with multiple inputs and outputs, for both linear and nonlinear systems. A state-space representation is a mathematical form of describing a physical system through a set of inputs, outputs, and state variables related by differential equations of any order, which are combined into a first-order matrix differential equation Bavafa-Toosi (2017). In particular, for the linear case of the second-order system with n oF, the state-space modeling is performed using a matrix equation of the form:

$$\dot{x}(t) = Ax(t) + Bu(t) \tag{2.11}$$

$$\underbrace{\begin{bmatrix} \dot{x} \\ \ddot{x} \end{bmatrix}}_{\dot{x}(t)} = \underbrace{\begin{bmatrix} 0 & I \\ -M^{-1}K & -M^{-1}C \end{bmatrix}}_{A} \underbrace{\begin{bmatrix} x \\ \dot{x} \end{bmatrix}}_{x(t)} + \underbrace{\begin{bmatrix} 0 \\ M^{-1}F_0 \end{bmatrix}}_{B} \underbrace{f(t)}_{u(t)} \tag{2.12}$$

Where A is the state matrix of dimensions $(2n \times 2n)$ that incorporates the mass, damping, and stiffness matrices; B is the input matrix of dimensions $(2n \times q)$, which relates the q external forces to the system; $u(t)$ is the input vector containing the forces applied to the system. The remaining variables in the equation were described previously. For chapters 3 and 4, minor modifications to this nomenclature will be added as appropriate.

2.4 System response to a random excitation

Random processes are characterized by their unpredictable behavior; although they cannot be predicted exactly, they can be treated statistically. As previously mentioned, the road profile is a random process and also stochastic. This implies that certain statistical measures describe its behavior. In particular, road profiles follow a Gaussian probability distribution, are defined such that the mean $\mu = 0$ and a standard deviation σ, and are governed by the following formula:

$$\sigma^2 = E\{(x-\mu)^2\} = E\{x^2\} = (\mathrm{RMS}(x))^2 \tag{2.13}$$

Given the characteristics of linear systems, if the random excitation adheres to these properties, the system's oscillatory response will do so as well. For this reason, statistical measures such as variance or RMS are widely used to characterize the system's response to random excitation. Additionally, the RMS of a signal serves as a measure of its total energy, making it highly useful not only for characterizing responses to random inputs but also for harmonic or discrete inputs.

In this section, two mathematical methods are analyzed to characterize the system's response to random excitation. First, spectral density analysis is introduced, performed in the frequency domain. Second, covariance analysis is presented, performed in the time domain. Both methods provide insights into the stationary response of the system.

2.4.1 Spectral density analysis

The spectral density analysis is a tool used to study the power of a signal within a given frequency range. With the objective of deriving an analytical expression for comfort and grip indicators, spectral density analysis can be applied to the system's response Wijker (2018). Assuming a stochastic disturbance defined as white noise, the RMS value of the system's response is given by:

$$y_{\text{rms}} = \sigma_y = \sqrt{\int_0^\infty S_{yy}(\omega)\, d\omega} \tag{2.14}$$

$$S_{yy}(\omega) = |H_y(i\omega)|^2 S_{vv} \tag{2.15}$$

where H_y represents the system's transfer function, which relates the input to the output of the physical quantity of interest; S_{yy} is the single-sided PSD of the system's response; and S_{vv} is the PSD of the road, given by $S_{vv} = G_{vv}V_x$, where, as mentioned earlier, G_{vv} is a characteristic of the road and V_x is the speed.

This analysis can be extended to Multiple Input Multiple Output (MIMO) systems using different methods, such as the modal displacement method indicated in Wijker (2009). However, for practical purposes, these analyses present significant challenges when attempting to derive an analytical solution, especially due to the improper integral. For this reason, covariance analysis is used, which bypasses the need for transfer functions and integrals, and further extends the analysis to nonlinear cases.

2.4.2 Covariance analysis

Covariance analysis is a fundamental statistical tool for studying correlations between different random variables in a given process. In the area of linear vibrations, the covariance matrix provides valuable information about the expected value of a specific variable, or more precisely, about its dispersion or root mean square Müller & Schiehlen (2012).

For a stable system excited by a white noise signal, the covariance matrix of the stationary response satisfies the following equation, known as the Lyapunov equation:

$$AP_x + P_x A^T + BQ_W B^T = 0 \tag{2.16}$$

Where, A is the state matrix of the system; B is the input matrix; P_x is the covariance matrix, equivalent to the mathematical expectation of the system $\mathbb{E}\{xx^T\}$; Q_W is the intensity matrix of the white noise. An extensive demonstration of the relationship between the Lyapunov equation and the dispersion of the system's stationary response can be found in Müller & Schiehlen (2012) and Wijker (2009).

Once the covariance matrix is known, it is possible to determine the variance of a given quantity σ_i^2 using the weighting vectors w_i^TWijker (2009). These vectors weight the variances of the system states contained in P_x, to obtain a physical quantity of interest, as described by:

$$\sigma_i^2 = w_i^T P_x w_i \tag{2.17}$$

As mentioned at the beginning of section **2.4**, for linear systems excited by a random disturbance with mean $\mu = 0$ and standard deviation σ (white noise input), their response is such that their variance σ^2 coincides with the square of the RMS value (equation 2.13). For this reason, covariance analysis significantly simplifies the process of calculating the RMS value of the system response, reducing it to solving the Lyapunov equation.

2.5 Summary

In this chapter, the theoretical framework was constructed to support the mathematical properties necessary to understand the optimization process that will be carried out in this investigation. First, the road profile was characterized by approximating it as a stochastic process according to ISO 8608, which models road irregularities as a white-noise process. Subsequently, performance indicators were selected based on a literature review to quantify road-holding and comfort.

The general dynamic equations of suspension systems were presented, emphasizing state-space modeling as a tool to study responses to random excitations. Two mathematical approaches, spectral analysis and covariance analysis, were explored to link road irregularities with the vibratory response of the system. These methods provide the basis for deriving analytical expressions of comfort and road-holding indicators in subsequent models.

The methodologies developed in this chapter provide the justification for their application in later chapters, where these tools will be used to derive analytical expressions for comfort and road-holding in the QCM and HCM, enabling the determination of algebraic expressions for the optimal suspension coefficients in each model.

Chapter 3

Suspension optimization for Quarter Car Model

In this chapter, the quarter car model is formally presented. First, the dynamic equations of the system are derived and the definitions of both performance indices are shown. Next we analyse the system's response to random excitation, in both the time and frequency domains, leading to explicit expressions for the performance indices in terms of the system parameters. Finally, a single-objective optimization is performed, determining the design parameters that maximize the suspension performance for each indicator independently. Some general conclusions are drawn regarding the optimal values for each indicator, and reference is made to previous works found in the literature.

3.1 Quarter Car Model

The Quarter Car Model is one of the most widely studied approaches for simplifying vehicle suspension analysis. This model represents one-quarter of a vehicle through sprung and unsprung masses connected by a suspension system, characterized by its lumped parameters. It emerged from the need to study both the vertical accelerations of the chassis (to quantify comfort) and the relative displacement between the wheel and road (to quantify grip), being the most fundamental model that allows the analysis of these variables. Since its main objective is to capture the system's vertical displacements, while horizontal motion is ignored, providing a simplified representation of the oscillatory behavior that results from the interaction between the vehicle and road irregularities. Figure 3.1 shows a diagram of the model. In this lumped

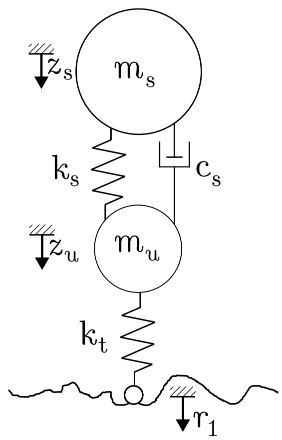

Figure 3.1: Schematic representation of the Quarter Car Model with lumped parameters.

parameter model, the sprung mass m_s corresponds to one-quarter of the chassis, and the unsprung mass m_u represents the equivalent mass of the wheel and suspension arms. The suspension is modeled by its stiffness k_s and damping coefficient c_s, while the tire is represented as an ideal spring with stiffness k_t.

Implied in these definitions, as in subsequent models, it is assumed that the lumped parameters follow linear behavior. The equations of motion for this system are given by:

$$m_s\ddot{z}_s + c_s\dot{z}_s - c_s\dot{z}_u + k_s z_s - k_s z_u = 0 \tag{3.1}$$

$$m_u\ddot{z}_u - c_s\dot{z}_s + c_s\dot{z}_u - k_s z_s + (k_t + k_s)z_u = k_t r_1 \tag{3.2}$$

Expressed in matrix form, the system of equations can be understood as:

$$M\{\ddot{z}\} + C\{\dot{z}\} + K\{z\} = Fr_1 \tag{3.3}$$

where each term is as follows:

$$M = \text{diag}[m_s\ m_u]\ , \quad F = [0\ k_t]^{\mathrm{T}}$$

$$C = \begin{bmatrix} c_s & -c_s \\ -c_s & c_s \end{bmatrix}; \quad K = \begin{bmatrix} k_s & -k_s \\ -k_s & k_s + k_t \end{bmatrix}$$

Following the indications in Chapter 2 and in accordance with Popp & Schiehlen (2010), first the system is expressed in the state-space formulation and then its first derivative is considered. This allows the system to be excited by the disturbance $\dot{r}(t)$ instead of $r(t)$, which, as discussed previously, results in a white noise input.

$$\underbrace{\begin{bmatrix} \ddot{z} \\ \dddot{z} \end{bmatrix}}_{\ddot{x}} = \underbrace{\begin{bmatrix} 0_{2\times2} & I_{2\times2} \\ -M^{-1}K & -M^{-1}C \end{bmatrix}}_{A} \underbrace{\begin{bmatrix} \dot{z} \\ \ddot{z} \end{bmatrix}}_{\dot{x}} + \underbrace{\begin{bmatrix} \mathbf{0}_{2\times1} \\ M^{-1}F \end{bmatrix}}_{B} \underbrace{\dot{r}(t)}_{w(t)} \tag{3.4}$$

By substituting the terms of the matrices and applying a variable change to simplify the notation, the system's A and B matrices are obtained:

$$a = \frac{k_s}{m_s}, \quad b = \frac{k_s}{m_u}, \quad c = \frac{k_t}{m_u}, \quad d = \frac{c_s}{m_s}, \quad e = \frac{c_s}{m_u} \tag{3.5}$$

$$A = \begin{bmatrix} 0 & 0 & 1 & 0 \\ 0 & 0 & 0 & 1 \\ -a & a & -d & d \\ b & -b-c & e & -e \end{bmatrix}, \quad B = \begin{bmatrix} 0 \\ 0 \\ 0 \\ c \end{bmatrix}$$

3.2 Performance indices to the QCM

Before analyzing the system's response, it is necessary to formally select the performance indices. In Chapter 2, the indices P_{C_2} and P_{N_2} were introduced in Equations (2.8) and (2.9). For the QCM, the comfort and road-holding indicators have already been defined by other authors as the RMS of the acceleration of the sprung mass and the variation in contact force, respectively Lot & Sadauckas (2021). Accordingly, the following expressions are used for the performance indices in the QCM:

$$J_1 = \text{RMS}(\ddot{z}_s(t)) \tag{3.6}$$

$$J_2 = \text{RMS}(F_{contact}) = \text{RMS}(k_t(r(t) - z_u(t))) \tag{3.7}$$

While for the QCM this definition is rather trivial, this process will become more relevant in subsequent models, where the system's oF do not directly correspond to the physical quantities being measured (see **4.2**).

3.3 Response to a random excitation: Covariance Analysis to the QCM

As mentioned in Section **2.1**, the road profile can be modeled as a random input with an approximately Gaussian distribution Múčka et al. (2019). Although other types of inputs, such as driver inputs, can excite the suspension of a vehicle, only road irregularities are analyzed due to their simplicity and mathematical properties. In this section, the covariance analysis is performed to obtain an analytical expression of the system's RMS response through the covariance matrix.

The covariance matrix contains the covariances between the elements of the state vector Sherman (2011), where the diagonal elements represent the variance of the vibratory response. By using weighting vectors, it is possible to calculate the variance of a magnitude of interest and, consequently, its RMS value. To obtain an analytical expression for the indicators J_1 and J_2, the following formulation is used:

$$J_1^2 = \sigma^2_{\ddot{z}_s} = w_1^T P_{\dot{x}} w_1 \tag{3.8}$$

$$J_2^2 = \sigma^2_{k_t(r-z_u)} = w_2^T P_{\dot{x}} w_2 \tag{3.9}$$

For stable linear dynamic systems that are excited by a white noise input, the system's response satisfies the Lyapunov equation. This equation relates the covariance matrix $P_{\dot{x}}$, to the white noise matrix Q_w. In this particular case, with a single-input system, the white noise intensity matrix corresponds to a scalar q with a magnitude of $\pi G_{dd} V_x$, as indicated in Popp & Schiehlen (2010). Thus, the Lyapunov equation takes the following form:

$$AP_{\dot{x}} + P_{\dot{x}}A^T + BQ_wB^T = 0 \Longleftrightarrow \underbrace{AP_{\dot{x}} + P_{\dot{x}}A^T}_{\textit{Left hand side}} = \underbrace{-qBB^T}_{\textit{Right hand side}} \Longleftrightarrow \underbrace{X}_{\textit{Left hand side}} = \underbrace{-qBB^T}_{\textit{Right hand side}} \tag{3.10}$$

Thus, the Lyapunov equation becomes a linear matrix equation. To solve this equation, Müller & Schiehlen (2012) proposes three methods, with the polynomial matrix method being the most commonly used. However, this method requires calculating the Hurwitz matrix and its determinant. Since the methodology is pretended to be applied in a model with four degrees of freedom, analytically computing the determinant of an 8×8 matrix becomes impractical.

For this reason, in this research, the **direct method** will be employed, which, by taking advantage of the symmetry of $P_{\dot{x}}$ and X, reduces the linear equation of dimension $2n \times 2n$ into a system of linear equations of dimension $2n(2n+1)/2$, where the unknowns correspond to the P_{ij} terms of the covariance matrix and n the degrees of freedom of the system. In particular, this is done considering the equivalence between the left hand side and the right hand side, a linear system of equations is constructed, equating each term on the left hand side (X_{ij}) with its respective term on the right hand side ($-qBB^T{}_{ij}$). For the left hand side, the following is obtained:

$$
\begin{aligned}
X_{11} &= 2P_{13} \\
X_{12} &= P_{14} + P_{23} \\
X_{13} &= -aP_{11} + aP_{12} - dP_{13} + dP_{14} + P_{33} \\
X_{14} &= bP_{11} - (b+c)P_{12} + eP_{13} - eP_{14} + P_{34} \\
X_{22} &= 2P_{24} \\
X_{23} &= -aP_{12} + aP_{22} - dP_{23} + dP_{24} + P_{34} \\
X_{24} &= bP_{12} - (b+c)P_{22} + eP_{23} - eP_{24} + P_{44} \\
X_{33} &= -2aP_{13} + 2aP_{23} - 2dP_{33} + 2dP_{34} \\
X_{34} &= bP_{13} - aP_{14} - (b+c)P_{23} + aP_{24} + eP_{33} - (d+e)P_{34} + dP_{44} \\
X_{44} &= 2bP_{14} - 2(b+c)P_{24} + 2eP_{34} - 2eP_{44}
\end{aligned}
$$

While for the right hand side, the following is obtained:

$$
\begin{array}{lll}
-qBB^T{}_{11} = 0 & -qBB^T{}_{12} = 0 & -qBB^T{}_{13} = 0 \\
-qBB^T{}_{14} = 0 & -qBB^T{}_{22} = 0 & -qBB^T{}_{23} = 0 \\
-qBB^T{}_{24} = 0 & -qBB^T{}_{33} = 0 & -qBB^T{}_{34} = 0
\end{array}
$$

$$-qBB^T{}_{44} = -qc^2$$

Finally, by reorganizing the terms, the system of linear equations with 10 unknowns is obtained:

$$\begin{bmatrix} 0 & 0 & 2 & 0 & 0 & 0 & 0 & 0 & 0 & 0 \\ 0 & 0 & 0 & 1 & 0 & 1 & 0 & 0 & 0 & 0 \\ -a & a & -d & d & 0 & 0 & 0 & 1 & 0 & 0 \\ b & -b-c & e & -e & 0 & 0 & 0 & 0 & 1 & 0 \\ 0 & 0 & 0 & 0 & 0 & 0 & 2 & 0 & 0 & 0 \\ 0 & -a & 0 & 0 & a & -d & d & 0 & 1 & 0 \\ 0 & b & 0 & 0 & -b-c & e & -e & 0 & 0 & 1 \\ 0 & 0 & -2a & 0 & 0 & 2a & 0 & -2d & 2d & 0 \\ 0 & 0 & b & -a & 0 & -b-c & a & e & -e-d & d \\ 0 & 0 & 0 & 2b & 0 & 0 & -2b-2c & 0 & 2e & -2e \end{bmatrix} \begin{bmatrix} P_{11} \\ P_{12} \\ P_{13} \\ P_{14} \\ P_{22} \\ P_{23} \\ P_{24} \\ P_{33} \\ P_{34} \\ P_{44} \end{bmatrix} = \begin{bmatrix} 0 \\ 0 \\ 0 \\ 0 \\ 0 \\ 0 \\ 0 \\ 0 \\ 0 \\ -qc^2 \end{bmatrix} \tag{3.11}$$

To solve the system of equations, the symbolic algebra software Maple was used, resulting in the terms P_{ij} in the following form (only two are shown for explanatory purposes):

$$P_{11} = \frac{q}{2}\frac{a^2\,d + a^2\,e + c\,d^3 + c\,d^2\,e + a\,b\,d + a\,b\,e + a\,c\,e}{(b\,d^2 - a\,e^2 - a\,d\,e + b\,d\,e + c\,d\,e)}$$

$$P_{33} = \frac{q}{2}\frac{c\,(a^2\,d + e\,a^2 + c\,d^3)}{(b\,d^2 - a\,e^2 - a\,d\,e + b\,d\,e + c\,d\,e)}$$

Then, replacing with the corresponding definitions of a, b, c, d y e defined in (3.5), the terms of the covariance matrix are obtained:

$$
\begin{aligned}
P_{11} &= q_{\dot{r}} \frac{k_s^2(m_s+m_u)^2 + k_t(c_s^2(m_s+m_u) + k_s m_s^2)}{2c_s k_t m_s^2} \\
P_{12} &= q_{\dot{r}} \frac{k_s^2(m_s+m_u)^2 + k_t(c_s^2(m_s+m_u) - k_s m_s m_u)}{2c_s k_t m_s^2} \\
P_{13} &= 0 \\
P_{14} &= q_{\dot{r}} \frac{-k_t}{2m_s} \\
P_{22} &= q_{\dot{r}} \frac{k_s^2(m_s+m_u)^2 + c_s^2 k_t(m_s+m_u) + k_t m_s^2(k_t - k_s - 2k_s m_u/m_s)}{2c_s k_t m_s^2} \\
P_{23} &= q_{\dot{r}} \frac{k_t}{2m_s} \\
P_{24} &= 0 \\
P_{33} &= q_{\dot{r}} \frac{k_s^2(m_s+m_u) + c_s^2 k_t}{2c_s m_s^2} \\
P_{34} &= q_{\dot{r}} \frac{k_s^2(m_s+m_u) + k_t(c_s^2 + k_s m_s)}{2c_s m_s^2} \\
P_{44} &= q_{\dot{r}} \frac{k_s^2(m_s m_u + m_u^2 - 2k_t m_s m_u/k_s) + k_t(k_t m_s^2 + c_s^2 m_u)}{2c_s m_s^2 m_u}
\end{aligned}
$$

According to section **2.4.2**, with the obtained covariance matrix, it is possible to determine the variance of the system states (and consequently the indicators P_{C_2} and P_{N_2}) using the weighting vectors w_i^T. Therefore, it is necessary to define the appropriate weighting vectors to calculate the physical quantities of interest from the state vector $\dot{x}(t)$. Since the comfort and road holding indicators require the chassis acceleration $\ddot{z}_s$ and the contact force $k_t(r - z_u)$, respectively, the weighting vectors are defined as follows:

$$
\ddot{z}_s = [0 \quad 0 \quad 1 \quad 0] \begin{bmatrix} \dot{z}_s \\ \dot{z}_u \\ \ddot{z}_s \\ \ddot{z}_u \end{bmatrix} = w_1^T \dot{x} \tag{3.12}
$$

$$k_t(r - z_u) = [0 \quad 0 \quad m_s \quad m_u] \begin{bmatrix} \dot{z}_s \\ \dot{z}_u \\ \ddot{z}_s \\ \ddot{z}_u \end{bmatrix} = w_2^T \dot{x} \tag{3.13}$$

It is worth mentioning that equation (3.13) arises from a linear combination of equations (3.1) and (3.2). This relationship is also known as the invariant equation, as it does not depend on the suspension parameters k_s and c_s Limebeer & Massaro (2018). Finally, based on the relationship between the state variance and the comfort and grip indicators,the analytical expressions for the performance indicators are given by:

$$J_1^2 = \sigma_{\ddot{z}_s}^2 = w_1^T P_x w_1 = P_{33} \tag{3.14}$$

$$J_2^2 = \sigma_{k_t(r-z_u)}^2 = w_2^T P_x w_2 = m_s^2 P_{33} + 2m_s m_u P_{34} + m_u^2 P_{44} \tag{3.15}$$

And substituting the obtained expressions for the elements of the covariance matrix:

$$J_1 = \sqrt{(\pi G_{dd} V_x) \cdot \frac{k_s^2(m_s + m_u) + c_s^2 k_t}{2c_s m_s^2}} \tag{3.16}$$

$$J_2 = \sqrt{(\pi G_{dd} V_x) \cdot \frac{(m_s + m_u)^2(k_s^2(m_s + m_u) + c_s^2 k_t) + k_t m_s m_u(k_t m_s - 2k_s(m_s + m_u))}{2c_s m_s^2}} \tag{3.17}$$

This result coincides with that obtained by Limebeer & Massaro (2018), who conducted a covariance analysis using a different set of coordinates to describe the degrees of freedom. Although this approach led to a different state vector components and the covariance matrix, but the indicators P_{C_2} and P_{N_2} yielded the same results. With the analytical expressions of the performance indicators, it is possible to conduct a parametric analysis of the influence of the lumped parameters, while also enabling an optimization process. In the following section, the spectral density analysis will be presented as an alternative tool for obtaining these performance indicators. Special emphasis will be placed on the complexities of this approach and the additional challenges it poses compared to covariance analysis.

3.4 Response to a random excitation: Power Spectral Density analysis to the QCM

This section briefly addresses the method of power spectral density analysis presented in **2.4.1**. Frequency domain analysis is a mathematical tool used to analyze the dynamic response of any time-invariant system. Specifically, for linear time-invariant systems, two relevant properties are observed. First, when a system is excited with a harmonic oscillatory perturbation, its response will also be harmonic. On the other hand,the superposition principle holds, which helps if the input is not harmonic, it can be converted into a series of harmonics (similar to the principle applied in (2.2)), the response to each harmonic can be evaluated and then combined using the superposition principle Lot & Sadauckas (2021).

By applying the Laplace transform to the equations of motion (3.1) and (3.2) in the time domain, it is possible to find the system's response in the frequency domain to a harmonic excitation from road profile irregularities. Without delving into the manipulation of the equations using complex algebra, the following relationships are obtained:

$$z_s(s) = \frac{[c_s(s) + k_s]k_t}{\mathbf{D}(s)} r(s) \tag{3.18}$$

$$z_u(s) = \frac{[m_s(s)^2 + c_s(s) + k_s]k_t}{\mathbf{D}(s)} r(s) \tag{3.19}$$

Where:

$$\begin{aligned} \mathbf{D}(s) &= |(s)^2\mathbf{M} + (s)\mathbf{C} + \mathbf{K}| && (3.20) \\ &= m_s m_u (s)^4 + c_s(m_s + m_u)(s)^3 \\ &\quad + [(k_s + k_t)m_s + k_s m_u](s)^2 \\ &\quad + (c_s k_t)(s) + k_t k_s && (3.21) \end{aligned}$$

In accordance with the analysis carried out in section **3.3** and equations (3.6) and (3.7), transfer functions are defined to relate the physical quantities of interest to a respective external disturbance. Thus, with the aim of evaluating performance indicators, the following transfer functions are defined, relating road irregularities to the physical quantities of interest:

$$\mathbf{H}_{J_1} = \frac{\ddot{z}_s(s)}{\dot{r}(s)} = \frac{[c_s(s) + k_s]k_t(s)}{\mathbf{D}(s)} \tag{3.22}$$

$$\mathbf{H}_{J_2} = \frac{z_u(s) - r(s)}{\dot{r}(s)} = -\frac{[m_s m_u(s)^2 + (c_s(m_s + m_u))(s) + k_s(m_s + m_u)]k_t(s)}{\mathbf{D}(s)} \tag{3.23}$$

Figures 3.2a and 3.2b show the magnitude of the FRF for a generic vehicle. These figures illustrate the magnitude of the system's harmonic response when subjected to harmonic excitation at various frequencies. As discussed in **Section 2.1**, the road profile can be decomposed into a series of harmonics within a specific frequency range. This decomposition, combined with the superposition principle, enables the transfer functions to provide valuable insights into the system's dynamic behavior.

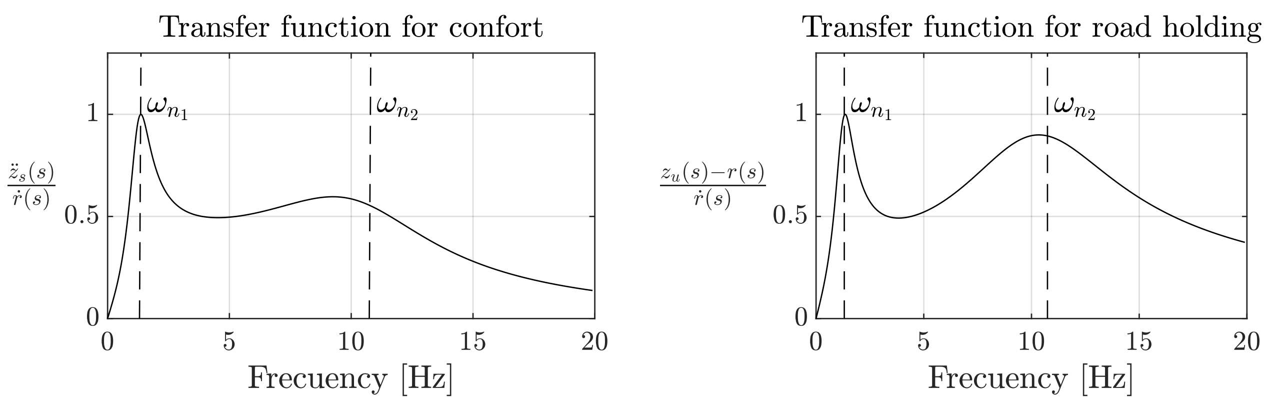

(a) Transfer function for comfort, within the frequency range of 0 to 20 Hz.

(b) Transfer function for road holding, within the frequency range of 0 to 20 Hz.

Figure 3.2: Frequency Response Functions (FRF's) for a generic vehicle using the Quarter Car Model. Both figures are normalized with respect to their peak values. Resonant zones near the system's natural frequencies are observed in both cases.

Following the previous statement, if the system input is random, its response will also be random. Just as the PSD is used to characterize system disturbance, it is also used to characterize its response through equation (2.15). However, this research aims to characterize the RMS of the vibratory response, which, for time-invariant systems, is given by the improper integral of its PSD, as indicated in (2.14). Based on these properties, the performance indicators can be derived as:

$$J_1 = \mathrm{RMS}(\ddot{z}_s(t)) = \sqrt{\int_0^\infty |\mathbf{H}J_1(s)|^2 ds G_{vv} V_x} \tag{3.24}$$

$$J_2 = \mathrm{RMS}(k_t(r(t) - z_u(t))) = \sqrt{\int_0^\infty |\mathbf{H}J_2(s)|^2 ds GvvV_x} \tag{3.25}$$

When the respective transfer function definitions are substituted, it is obtained:

$$J_1 = \sqrt{\int_0^\infty \left| \frac{[c_s(s) + k_s]k_t(s)}{\mathbf{D}(s)} \right|^2 ds G_{vv} V_x} \tag{3.24}$$

$$J_2 = \sqrt{\int_0^\infty \left| \frac{[m_s m_u (s)^2 + (c_s(m_s + m_u))(s) + k_s(m_s + m_u)]k_t(s)}{\mathbf{D}(s)} \right|^2 ds G_{vv} V_x} \tag{3.25}$$

By solving each integral, according to Lot & Sadauckas (2021), the following is obtained:

$$J_1 = \sqrt{(\pi G_{dd} V_x) \cdot \frac{k_s^2(m_s + m_u) + c_s^2 k_t}{2c_s m_s^2}} \tag{3.26}$$

$$J_2 = \sqrt{(\pi G_{dd} V_x) \cdot \frac{(m_s + m_u)^2(k_s^2(m_s + m_u) + c_s^2 k_t) + k_t m_s m_u (k_t m_s - 2k_s(m_s + m_u))}{2c_s m_s^2}} \tag{3.27}$$

This result aligns with those obtained from the covariance analysis in (3.16) and (3.17). However, upon analyzing expressions (3.24) and (3.25), their complexity immediately stands out, making analytical resolution of the improper integral challenging. While complex calculus theorems, such as the residue theorem Kreyszig (2010), facilitate the process, it remains complicated. A comprehensive development of these integrals is available in Green & Limebeer (2012) and Limebeer & Massaro (2018), although the step-by-step process falls outside the scope of this research. Considering that the subsequent chapters aim to use more complex models with additional degrees of freedom, spectral density analysis becomes impractical. Therefore, for the following models, only covariance analysis will be used.

3.5 Suspension optimization for the QCM

This section addresses suspension optimization through the minimization of performance indicators J_1 and J_2 (where minimizing these indicators leads to improved performance). These indicators depend on road parameters G_{dd} and vehicle velocity V_x, as well as various vehicle parameters such as m_s, m_u, k_t, k_s, and c_s. Since this research focuses on suspension optimization, we will determine the values $k_{s,\text{opt}}$ and $c_{s,\text{opt}}$ that optimize suspension performance, while the remaining parameters are considered design constraints.

3.5.1 Suspension optimization for comfort in the QCM

Using multivariable calculus properties, it can be demonstrated that, for $c_s \neq 0$, the indicator J_1, now referred to as the objective function, presents an absolute minimum when:

$$\nabla J_1(k_s, c_s) = 0 \tag{3.28}$$

Thus, for the first partial derivative:

$$\frac{\partial J_1}{\partial k_s} = \pi G_{dd} V_x \frac{k_s(m_u + m_s)}{c_s m_s^2} = 0 \Longrightarrow k^\star_{s,J_1} = 0 \tag{3.29}$$

Where $k^\star_{s,J_1}$ corresponds to the suspension stiffness value that minimizes discomfort. For real applications, it is impossible to use a suspension with zero stiffness, therefore we will seek to satisfy the second partial derivative $\frac{\partial J_1}{\partial c_s} = 0$ for $k_s \neq 0$. Thus, for the second:

$$\frac{\partial J_1}{\partial c_s} = \pi G_{dd} V_x \frac{c_s^2 k_t - k_s^2(m_u + m_s)}{2 c_s^2 m_s^2} = 0 \Longrightarrow c^\star_{s,J_1} = k_s \sqrt{\frac{m_u + m_s}{k_t}} \tag{3.30}$$

Where, $c^\star_{s,J_1}$ corresponds to the damping coefficient value that minimizes discomfort when $k_s \neq 0$. Notably, the optimal suspension coefficients are independent of road roughness or vehicle speed, and so a suspension optimized for comfort will remain effective under any driving condition, as long as the system remains linear.

Figures 3.3a and 3.3b show the discomfort indicator J_1 as a function of suspension coefficients, clearly demonstrating the presence of k_{s,opt,J_1} and c_{s,opt,J_1} that minimize this indicator. Figure 3.4 show the optimal damping as a function of the suspension stiffness. A generic case is modeled using parameters $m_u = 35$ $[kg]$, $m_s = 250$ $[kg]$, $k_t = 150$ $[kN/m]$, which correspond to reference values used by Scheibe & Smith (2009), while for driving conditions, a class C road is assumed, with $G_{dd} = 2.54 \cdot 10^{-}4$ $[m^2/(cycle/m)]$ and $V_x = 25$ $[m/s]$. Analyzing Eq. (3.30)

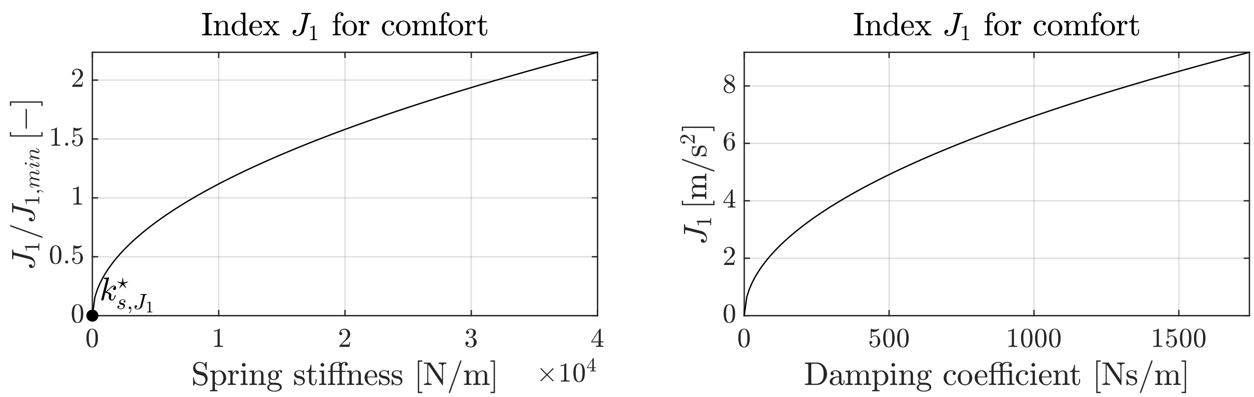

(a) J_1 index as a function of k_s with optimal damping.

(b) J_1 index as a function of c_s with $k_s = 8000$ [N/m].

Figure 3.3: Global optimum for J_1 as a function of k_s and c_s.

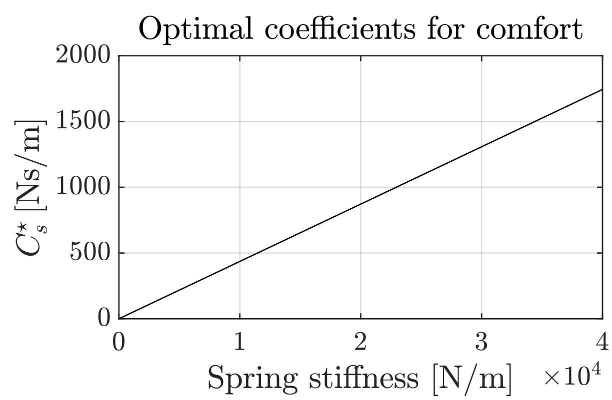

Figure 3.4: Optimal damping coefficient.

and Figure 3.4, it can be observed that the optimal damping coefficient is proportional to the stiffness of the suspension. The following section presents a similar analysis for the tyre grip performance indexJ_2.

3.5.2 Suspension optimization for road holding in the QCM

Using multivariable calculus properties, it can be demonstrated that, for $c_s \neq 0$, the indicator J_2 presents a global minimum when:

$$\nabla J_2(k_s, c_s) = 0 \tag{3.31}$$

Thus, for each partial derivative we have:

$$\frac{\partial J_2}{\partial k_s} = \pi G_{dd} V_x \frac{(m_u + m_s)^3 k_s - k_t m_s m_u (m_u + m_s)}{c_s m_s^2} = 0 \tag{3.32}$$

$$\frac{\partial J_2}{\partial c_s} = \pi G_{dd} V_x \frac{((m_u + m_s)^2 (k_s^2 (m_u + m_s) - k_t c_s^2)) + k_t m_s m_u (k_t m_s - 2k_s (m_u + m_s))}{2 c_s^2 m_s^2} = 0 \tag{3.33}$$

Thus, by solving for k_s and c_s that satisfy (3.32) and (3.33), the optimal road holding coefficients $k^\star_{s,J_2}$ and $c^\star_{s,J_2}$ are obtained:

$$(m_u + m_s)^3 k_s - 2k_t m_s m_u (m_u + m_s) = 0 \iff k^\star_{s,J_2} = \frac{k_t m_s m_u}{(m_s + m_u)^2} \tag{3.34}$$

$$c_s^2 k_t (m_s + m_u)^2 + \frac{k_t^2 m_s^2 m_u^2}{m_s + m_u} - k_t^2 m_s^2 m_u = 0 \iff c^\star_{s,J_2} = \sqrt{\frac{k_t m_s^3 m_u}{(m_s + m_u)^3}} \tag{3.35}$$

As with comfort optimization, it is observed that the optimal values do not depend on road roughness or vehicle speed, and so a suspension optimized for road holding will remain effective under any driving condition, provided that the system remains linear. Another notable conclusion is that the optimal damping value is independent of suspension stiffness. This finding contradicts certain design recommendations that suggest optimal damping for road holding should be based on critical damping, and therefore on suspension stiffness, as noted in Pütz & Serné (2022). This contradiction is explained by the oversimplifications of the QCM, which assume a linear system, steady-state response, and Gaussian distribution of road irregularities.

Figures 3.5a and 3.5b show the road holding index as a function of the suspension coefficients, where it can be observed that for a given coefficient k_s or c_s, there exists an optimal combination

($k_s^\star$ and $c_s^\star$) that minimizes the index. The same generic case used for the comfort index is modeled, obtaining the following results.

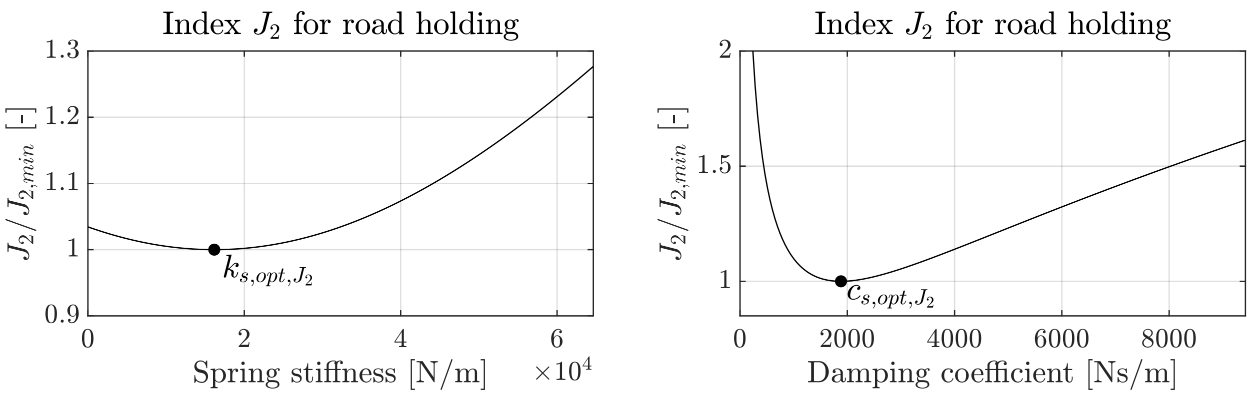

(a) J_2 index as a function of k_s with optimal damping.

(b) J_2 index as a function of c_s with optimal damping.

Figure 3.5: Global optimum for J_2 as a function of k_s and c_s

At comparing the optima of both indicators, it is observed that the optimal values for road holding are larger in magnitude than those for comfort. However, since it is usually desirable to achieve both, when optimizing suspensions, it is necessary to find a balance between comfort and road holding—a trade-off that has been previously addressed by other authors, such as Limebeer & Massaro (2018). Another key conclusion from this analysis is that both indicators cannot be minimized simultaneously, resulting in a Pareto front in the optimization process that demarcates a boundary of optimal values and a region of suboptimal solutions.

The Figure 3.6 illustrates this phenomenon, showing the Pareto front in the optimization of indicators J_1 and J_2. The values are normalized with respect to their optimal values, thus the point $(1, 1)$ represents an unattainable point when both indicators are minimized. The suboptimal region for different stiffness and damping coefficients is shown with black markers. Three contour curves are indicated, each showing the value of both indicators for a given stiffness level and varying damping coefficients. The point at which these contour curves intersect with the Pareto front is where the damping coefficient is optimal, according to the suspension stiffness. This visualization clearly highlights the compromise between comfort and road holding.

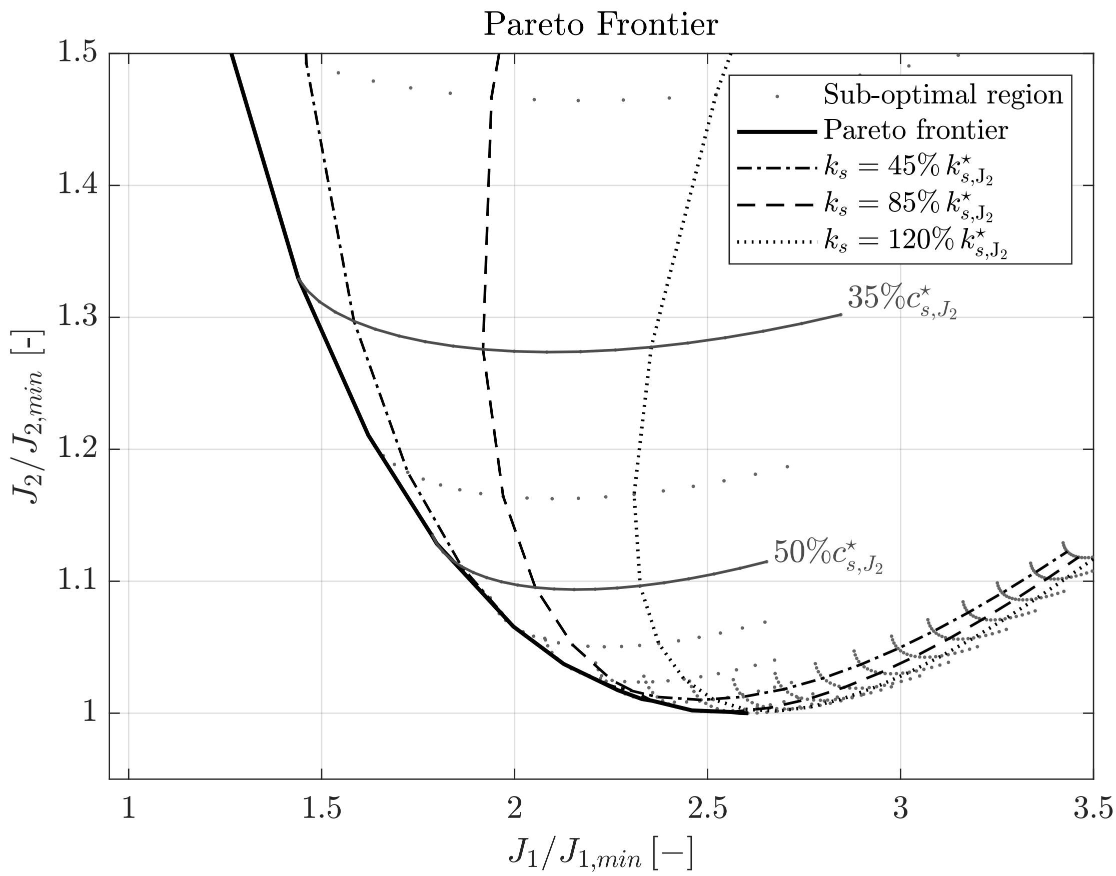

Figure 3.6: Frontier optimization between J_1 and J_2

3.6 Summary

In this chapter, the quarter car model was introduced as a mathematical model to study suspension performance based on specific performance indicators, with its advantages and limitations being briefly discussed. Using two mathematical methods, analytical expressions were developed to calculate the RMS value of the system's vibratory response when subjected to random excitation, directly addressing the need to find an analytical expression for the previously defined performance indicators, arriving at the same expressions through time-domain and frequency-domain formulations.

Based on the algebraic expressions for each indicator, a single-objective optimization was conducted, and the global optimums were derived and discussed. Lastly, the existence of a Pareto front was highlighted, showing that simultaneous optimization of both objectives is not possible. This front defines a boundary of optimal solutions and a region of suboptimal solutions.

Although these results have already been described in the literature, it is important to explain both the mathematical foundations and the step-by-step process of the single-objective optimization, as this is necessary for its application to a more complex model in the following chapter.

Chapter 4

Suspension optimization for the single axle Half Car Model

This chapter introduces the single-axle Half Car Model (HCM), extending the concepts developed for the Quarter Car Model. First, we formally present the model, detailing its degrees of freedom and the incorporation of an anti-roll bar as an interconnection element. Then, performance indicators for ride comfort (J_1) and road holding (J_2) are redefined to reflect the added complexity of the model, explicitly accounting for chassis rotation. Covariance analysis is applied to derive analytical expressions for these performance indicators. Finally, the chapter develops novel analytical solutions for the optimal suspension stiffness (k_s) and damping (c_s) that independently minimize J_1 and J_2, explicitly considering the influence of the anti-roll bar stiffness (k_r). The resulting optima are then compared to those derived from the QCM to quantify the impact of including roll dynamics and interconnection elements in suspension design.

4.1 Half Car Model

The Half Car Model (HCM) is an extension of the classical Quarter Car Model (QCM), offering a more comprehensive representation of a vehicle's dynamic behavior. While the QCM is limited to analyzing the vertical motion of a single wheel and one-quarter of the chassis, the HCM expands this framework by incorporating both vertical motion and chassis rotation, as well as the vertical displacement of two wheels. These two wheels can belong either to the same axle (see Figure 4.2a) or to different axles (see Figure 4.2b), enabling the study of roll and pitch dynamics, respectively.

This chapter focuses on the single-axle configuration of the model, which analyzes the vehicle from a frontal perspective under the assumption of lateral symmetry.

The single-axle HCM introduces two additional degrees of freedom, increasing the number of lumped parameters from five to eight (described later). Furthermore, this model allows for the inclusion of interconnection elements (semi-independent suspensions). Such is the case of anti-roll bars, which modify the oscillatory behavior predicted by the QCM by adding stiffness and/or damping. These interconnection elements cannot be modeled in the QCM due to its limited set of degrees of freedom.

Figure 4.1 illustrates a schematic representation of the single-axle HCM in a frontal view. The sprung mass m_s and its rotational inertia I_x represent half of the vehicle chassis, while the unsprung mass m_u corresponds to the equivalent mass of the wheels and their suspension arms, separated by a track width $t = a + a$. Each suspension arm is modeled with symmetric stiffness k_s and damping c_s, and is interconnected by an anti-roll bar of stiffness k_r. Tires are assumed to be identical and are modeled as ideal vertical springs with stiffness k_t. Road disturbances $r_1(t)$ and $r_2(t)$ act on each wheel, leading to a total of seven vehicle parameters and three driving scenario parameters (V_x, r_1, r_2).

One of the key advantages of this model is the inclusion of the Anti-roll bar (ARB), a widely used mechanical component specifically designed to reduce lateral body roll during cornering or when driving over uneven terrain Ramakrishna et al. (2017). By linking the left and right suspension components, an ARB uses its torsional stiffness to resist differential vertical wheel movements, thereby generating a restoring roll moment. This improves vehicle stability, reduces roll angles during maneuvers, and contributes to more precise handling Le & Pieper (2014). A major advantage of ARBs is that they allow achieving substantial roll stiffness without requiring excessively stiff main suspension springs, thus preserving ride comfort during straight-line driving Lu et al. (2024).

Another important assumption of this model concerns the correlation between road excitations $r_1(t)$ and $r_2(t)$. According to Popp & Schiehlen (2010), the excitations on the left and right

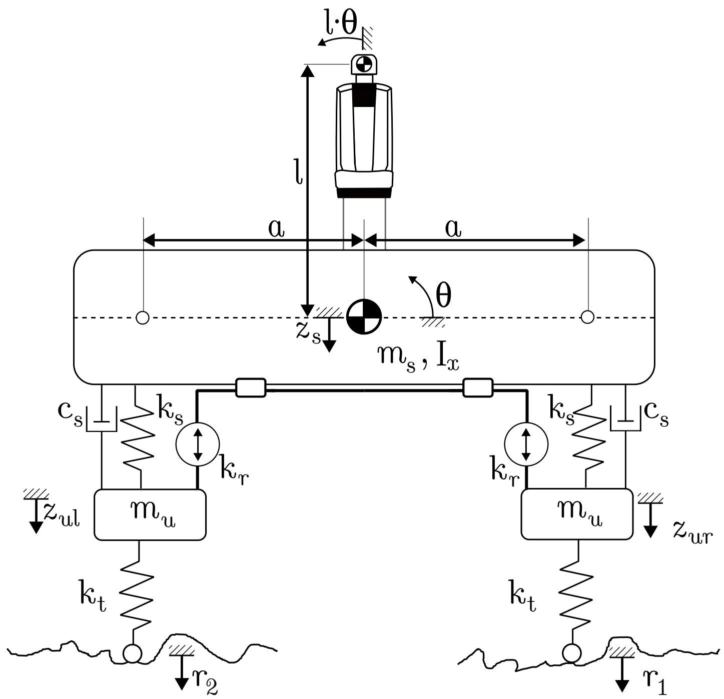

Figure 4.1: Schematic representation of the single-axle Half Car Model. The figure shows a frontal view of half the vehicle, assuming symmetry between left and right sides. Chassis roll motion is highlighted, along with the assumption of uncorrelated random excitations.

sides of the vehicle are supposed to be uncorrelated. However, for the two-axle HCM, two types of correlation will be considered to represent different driving scenarios. In this chapter, the covariance analysis is carried out assuming uncorrelated inputs. The case involving correlated disturbances, which introduces additional mathematical complexity, is addressed in the following chapter.

This section aims to analytically study the single-axle HCM by incorporating an ARB. A covariance analysis is then performed to evaluate the effect of the bar's torsional stiffness on the system's dynamic behavior. Analytical expressions for the corresponding performance indicators are derived, along with optimal formulations for suspension parameters that account for the ARB's influence.

4.2 Mathematical formulation of the single axle HCM with ARB

For this study, U-shaped ARB is assumed, reflecting a common configuration in passenger vehicles Milliken & Milliken (1994). While some authors model the ARB force as proportional solely to the chassis roll angle (e.g., Jazar (2008)), this work employs a more comprehensive formulation, similar to approaches in Gosselin-Brisson et al. (2009); Hassan et al. (2023), to ensure a full representation of the ARB's effect. This formulation explicitly considers the relative vertical displacement between the suspension attachment points, leading to an ARB force contribution expressed as:

$$F_{\mathrm{ARB}} = k_r\left(z_{\mathrm{susp},r} - z_{\mathrm{susp},l}\right) = k_r\left(a\theta + z_{u,r} + z_s - (-a\theta + z_{u,l} + z_s)\right) = k_r\left(2a\theta + z_{u,r} - z_{u,l}\right)$$

Here, (k_r) denotes the ARB's equivalent vertical stiffness, which implicitly includes the effects of the installation ratio and torque arm. Then, the equations of motion of the system can be expressed in matrix form as:

$$M\{\ddot{z}\}(t) + C\{\dot{z}\}(t) + K\{z\}(t) = f_1 r_1(t) + f_2 r_2(t) \tag{4.1}$$

Where,

$$M = \mathrm{diag}[m_u\ m_u\ m_s\ I_x]\ , \quad f_1 = [k_t\ 0\ 0\ 0]^{\mathrm{T}}\ , \quad f_2 = [0\ k_t\ 0\ 0]^{\mathrm{T}}\ ,$$

$$C = \begin{bmatrix} c_s & 0 & -c_s & ac_s \\ 0 & c_s & -c_s & -ac_s \\ -c_s & -c_s & 2c_s & 0 \\ ac_s & -ac_s & 0 & 2a^2c_s \end{bmatrix}\ ,$$

$$K = \begin{bmatrix} k_t + k_s + k_r & -k_r & -k_s & ak_s + 2ak_r \\ -k_r & k_t + k_s + k_r & -k_s & -ak_s - 2ak_r \\ -k_s & -k_s & 2k_s & 0 \\ ak_s + 2ak_r & -ak_s - 2ak_r & 0 & 2a^2k_s + 4a^2k_r \end{bmatrix}$$

As in the procedure applied in the previous chapter, the state-space formulation of the system in its differential form is used. Thus, two external disturbances, which are not necessarily correlated, are considered, and the following is obtained:

$$\ddot{x}(t) = A\dot{x}(t) + b_1\dot{r}_1(t) + b_2\dot{r}_2(t) = A\dot{x}(t) + Bw(t) \tag{4.2}$$

This forms a Multiple Input Multiple Output (MIMO) system, since it has two inputs. For this system with $n = 4$ degrees of freedom, the state-space formulation is represented by matrices of order $2n = 8$. Accordingly, the state vector $\dot{x}(t)$, the state matrix A, and the input matrix B are given by:

$$\dot{x}(t) = \begin{bmatrix} \dot{z}_{ur} & \dot{z}_{ul} & \dot{z}_s & \dot{\theta} & \ddot{z}_{ur} & \ddot{z}_{ul} & \ddot{z}_s & \ddot{\theta} \end{bmatrix}^T, \quad A = \begin{bmatrix} \mathbf{0}_{4\times4} & \mathbf{I}_{4\times4} \\ -M^{-1}K & -M^{-1}C \end{bmatrix} \tag{4.3}$$

$$b_1 = \begin{bmatrix} \mathbf{0}_{4\times1} \\ M^{-1}f_1 \end{bmatrix}, \quad b_2 = \begin{bmatrix} \mathbf{0}_{4\times1} \\ M^{-1}f_2 \end{bmatrix}, \quad B = \begin{bmatrix} b_1 & b_2 \end{bmatrix}, \quad w(t) = \begin{bmatrix} \dot{r}_1(t) \\ \dot{r}_2(t) \end{bmatrix} \tag{4.4}$$

4.3 Performance indices for the HCM

As discussed in Section **3.2**, the performance indices must be formally defined based on the motions of the particular model. As shown in (2.8), the indicator P_{C_2} quantifies linear acceleration in three orthogonal components. For the QCM, this is represented solely by the vertical acceleration of the suspended mass. However, in the HCM, the acceleration is influenced by both the vertical acceleration of the suspended mass $\ddot{z}_s(t)$ and its angular acceleration $\ddot{\theta}(t)$. Figure 4.2 illustrates the effects of vertical and angular accelerations on the driver's comfort in the two axle HCM.

Complementing this, the ISO standard [2131-4] Standarization (2001) recommends measuring accelerations at the driver's headrest. Therefore, an arbitrary distance l is defined between the driver's head and the center of gravity of the suspended mass, allowing the quantification of orthogonal accelerations in the vertical and lateral directions of the vehicle.

To keep the model as simple as possible, it is assumed that the driver's seat is vertically aligned with the chassis's center of mass. However, the model can be slightly modified to

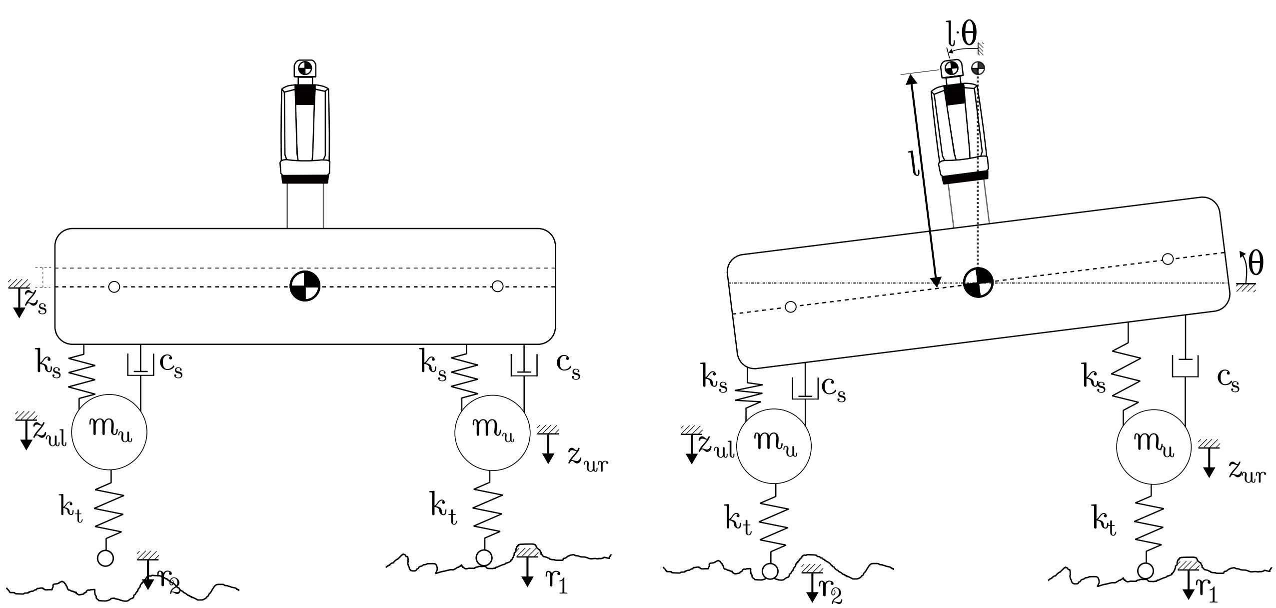

(a) Effect of the vertical accelerations of the suspended mass on the driver.

(b) Effect of the angular accelerations of the suspended mass on the driver.

Figure 4.2: Vertical and angular accelerations influencing driver comfort. The angular acceleration generates an effect on the driver's longitudinal acceleration.

evaluate comfort at different positions along the chassis. In (2.8), the performance index P_{C_2} is defined as the RMS of the vector sum of accelerations, Consequently, we propose the ride comfort index J_1 for the HCM, as the RMS resulting acceleration at the driver's head

$$P_{C_2} = \text{RMS}\left(\sqrt{(\ddot{z}_s(t))^2 + \left(l\ddot{\theta}(t)\right)^2}\right) = \sqrt{\text{RMS}(\ddot{z}_s(t))^2 + \text{RMS}\left(l\ddot{\theta}(t)\right)^2}. \tag{4.5}$$

The Eq (4.5) also makes the equality between the RMS of the resultant vector and the quadrature sum of the individual RMS components. Given the small displacements assumption, the vertical acceleration ($\ddot{z}_s$) and the lateral acceleration at the driver's head due to roll ($l\ddot{\theta}$) are treated as orthogonal components. Therefore, the magnitude (L2-norm) of the resultant acceleration vector, $\vec{a}(t)$, is given by:

$$|\vec{a}(t)|_2 = \sqrt{\ddot{z}_s(t)^2 + (l\ddot{\theta}(t))^2} \quad \Rightarrow \quad |\vec{a}(t)|_2^2 = \ddot{z}_s(t)^2 + (l\ddot{\theta}(t))^2.$$

For this reason,the RMS of vector acceleration is equivalent with the RMS equivalent to the quadrature sum of the RMS of its individual components. The formal proof is as follows:

$$\begin{aligned}\mathrm{RMS}^2(\vec{a}(t)) &= \frac{1}{n}\sum_{t=1}^{n}|\vec{a}(t)|_2^2 = \frac{1}{n}\sum_{t=1}^{n}\left[\ddot{z}_s(t)^2 + (l\ddot{\theta}(t))^2\right] \\ &= \frac{1}{n}\sum_{t=1}^{n}\ddot{z}_s(t)^2 + \frac{1}{n}\sum_{t=1}^{n}(l\ddot{\theta}(t))^2 \\ &= \mathrm{RMS}^2(\ddot{z}_s) + \mathrm{RMS}^2(l\ddot{\theta})\end{aligned}$$

On the other hand, the indicator P_{N_2} aims to quantify variations in the tire contact force. In the QCM, this depends on a single wheel, however, in the HCM, it is essential to consider the variation of the contact force in both tires simultaneously. Since these quantities are vibratory variables, they may be in phase or out of phase. Therefore, it is necessary to calculate the RMS of both contact forces separately and then combine them into a single performance indicator or, more precisely, an objective function to be minimized. Based on this requirement, a single performance indicator proportional to the grip in both tires is defined, based on the relative displacement between each unsprung mass and its respective road profile or irregularity. Thus, we propose the indicator P_{N_2} to be:

$$P_{N_2} = \mathrm{RMS}(F_{contact_r}) + \mathrm{RMS}(F_{contact_l}) = \mathrm{RMS}(k_t(r_1(t) - z_{ur}(t))) + \mathrm{RMS}(k_t(r_2(t) - z_{ul}(t))) \tag{4.6}$$

Based on the formulation of these indicators, a covariance analysis will be conducted to derive the analytical expressions for these performance indicators in the single axle HCM.

4.4 Response to a random excitation: Covariance Analysis to the single axle HCM

This section analyzes the system's response to two uncorrelated input excitations. The assumptions outlined in Section **2.1** are retained to model the excitations $r_1(t)$ and $r_2(t)$. Although these assumptions may not perfectly reflect real-world conditions, they offer a useful starting point for more advanced analyses using the half-car model.

As in the covariance analysis presented in the previous chapter, certain mathematical properties of the Gaussian distribution of the road profile are utilized to determine the variance of the system's response and, subsequently, its root mean square (RMS) value. This is achieved through algebraic operations involving the covariance matrix and weighting vectors, where the covariance matrix is obtained by solving the Lyapunov equation. Accordingly, for the HCM, the performance indicators are computed using the following formulation:

$$J_1 = \sqrt{\sigma^2_{\ddot{z}_s} + \sigma^2_{l\ddot{\theta}}} = \sqrt{w_z^T P_{\dot{x}} w_z + w_y^T P_{\dot{x}} w_y} \tag{4.7}$$

$$J_2 = J_{2,r} + J_{2,l} = \sigma_{k_t(r_1 - z_{ur})} + \sigma_{k_t(r_2 - z_{ul})} = \sqrt{w_r^T P_{\dot{x}} w_r} + \sqrt{w_l^T P_{\dot{x}} w_l} \tag{4.8}$$

where the subindex z and y are associated with vertical and effective tangential (due to roll) accelerations for comfort, respectively, while r and l are associated with the right and left wheels for road holding. Appropriate weighting vectors are defined to facilitate the transition from the state vector $\dot{x}(t)$, as defined in (4.3), to the performance indicators defined in (4.5) and (4.6). For the first index we derive w_z and w_y as follows:

$$\ddot{z}_s = [0_{1\times4} \quad 0 \quad 0 \quad 1 \quad 0] \begin{bmatrix} \dot{z}_{ur} & \dot{z}_{ul} & \dot{z}_s & \dot{\theta} & \ddot{z}_{ur} & \ddot{z}_{ul} & \ddot{z}_s & \ddot{\theta} \end{bmatrix}^T = w_z^T \dot{x} \tag{4.9}$$

$$l\ddot{\theta} = [0_{1\times4} \quad 0 \quad 0 \quad 0 \quad l] \begin{bmatrix} \dot{z}_{ur} & \dot{z}_{ul} & \dot{z}_s & \dot{\theta} & \ddot{z}_{ur} & \ddot{z}_{ul} & \ddot{z}_s & \ddot{\theta} \end{bmatrix}^T = w_y^T \dot{x} \tag{4.10}$$

For the second index, a slightly more in-depth analysis is required. As mentioned in (4.6), the variation in the contact force of both tires must be considered by calculating each force separately and then combining them into a single performance indicator. With this objective, the equations of motion (4.1) can be reformulated as follows:

$$m_u \ddot{z}_{ur} + F_{susp,r} + F_{ARB} = F_{tyre,r} \tag{4.11}$$

$$m_u \ddot{z}_{ul} + F_{susp,l} - F_{ARB} = F_{tyre,l} \tag{4.12}$$

$$m_s \ddot{z}_s - F_{susp,r} - F_{susp,l} = 0 \tag{4.13}$$

$$I_x \ddot{\theta} + aF_{susp,r} - aF_{susp,l} + 2aF_{ARB} = 0 \tag{4.14}$$

By applying an appropriate linear combination of equations (4.11), (4.12), (4.13), and (4.14), the contact force on each tire can be defined as a combination of the system's state variables:

$$m_u\ddot{z}_{ur} + \frac{1}{2}m_s\ddot{z}_s - \frac{I_x}{2a}\ddot{\theta} = k_t(r_1 - z_{ur}) \tag{4.15}$$

$$m_u\ddot{z}_{ul} + \frac{1}{2}m_s\ddot{z}_s + \frac{I_x}{2a}\ddot{\theta} = k_t(r_2 - z_{ul}) \tag{4.16}$$

In this way, the two weighting vectors required for the road-holding performance indicator are obtained as follows:

$$k_t(r_1 - z_{ur}) = \begin{bmatrix} 0_{1\times 4} & m_u & 0 & \frac{1}{2}m_s & -\frac{I_x}{2a} \end{bmatrix} \begin{bmatrix} \dot{z}_{ur} & \dot{z}_{ul} & \dot{z}_s & \dot{\theta} & \ddot{z}_{ur} & \ddot{z}_{ul} & \ddot{z}_s & \ddot{\theta} \end{bmatrix}^T = w_r^T\dot{x} \tag{4.17}$$

$$k_t(r_2 - z_{ul}) = \begin{bmatrix} 0_{1\times 4} & 0 & m_u & \frac{1}{2}m_s & \frac{I_x}{2a} \end{bmatrix} \begin{bmatrix} \dot{z}_{ur} & \dot{z}_{ul} & \dot{z}_s & \dot{\theta} & \ddot{z}_{ur} & \ddot{z}_{ul} & \ddot{z}_s & \ddot{\theta} \end{bmatrix}^T = w_l^T\dot{x} \tag{4.18}$$

Thus, based on the formulation for the comfort performance indicator (4.7) and the road-holding performance indicator (4.8), the following expressions are obtained in terms of the covariance matrix coefficients:

$$J_1 = \sqrt{w_z^T P_{\dot{x}} w_z + w_y^T P_{\dot{x}} w_y} = \sqrt{P_{77} + l^2 P_{88}} \tag{4.19}$$

$$J_2 = J_{2,r} + J_{2,l} \tag{4.8}$$

$$J_{2,r} = \sqrt{m_u^2 P_{55} + \left(\frac{1}{2}m_s\right)^2 P_{77} + \left(\frac{I_x}{2a}\right)^2 P_{88} + 2\left[\frac{m_s m_u}{2}P_{57} - \frac{I_x m_u}{2a}P_{58} - \frac{I_x m_s}{4a}P_{78}\right]} \tag{4.20}$$

$$J_{2,l} = \sqrt{m_u^2 P_{66} + \left(\frac{1}{2}m_s\right)^2 P_{77} + \left(\frac{I_x}{2a}\right)^2 P_{88} + 2\left[\frac{m_s m_u}{2}P_{67} + \frac{I_x m_u}{2a}P_{68} + \frac{I_x m_s}{4a}P_{78}\right]} \tag{4.21}$$

The main challenge of this approach lies in obtaining the covariance matrix. The procedure used to construct and derive the covariance matrix from the Lyapunov equation is outlined below. Both the construction of the equation and its resolution are analogous to the previous case. While the computational cost increases, the mathematical complexity remains unchanged, as long as the excitations remain uncorrelated. Thus, the following expression is obtained:

$$AP_{\dot{x}} + P_{\dot{x}}A^T + BQ_wB^T = 0 \Longleftrightarrow \underbrace{AP_{\dot{x}} + P_{\dot{x}}A^T}_{\textit{Left hand side}} = \underbrace{-q_{\dot{r}}BB^T}_{\textit{Right hand side}} \tag{4.22}$$

Where, the right side is simpler due to the uncorrelated excitations. The white noise intensity matrix Q_w becomes the same scalar $q_{\dot{r}}$ defined in the previous chapter, with a magnitude of $\pi G_{dd}V_x$. Consequently, since both vectors b_1 and b_2 are sparse, the product $q_{\dot{r}}BB^T$ also results in a sparse matrix. Specifically, the only non-zero terms are given by:

$$-q_{\dot{r}}BB^T{}_{55} = -q_{\dot{r}}BB^T{}_{66} = -q_{\dot{r}}\frac{k_t^2}{m_u^2} \tag{4.23}$$

On the other hand, the left side of the equation results in more terms. The covariance matrix $P_{\dot{x}}$, is an 8×8 symmetric and contains 64 terms in the form of P_{ij}. Performing the algebraic operations between A and $P_{\dot{x}}$ yields the left side of the equation. For this particular 4-oF system, the Lyapunov equation becomes a bilinear matrix equation, where the matrices are of order 8×8. Taking advantage of the symmetry of the covariance matrix, only 36 of its 64 elements need to be determined. In fact, it is sufficient to know only the ten P_{ij} elements that are part of (4.19), (4.20) and (4.21). To solve this, the direct method is employed.

In the direct method, the 8th-order bilinear matrix equation presented in Eq. (4.22) is transformed into a 36×36 linear system of equations, in the form $\hat{A}_{36\times36}\hat{x}_{36\times1} = \hat{b}_{36\times1}$. To further simplify the system we perform a reduction process which yields a new system with 26 unknowns. An analytical solution to this reduced system was obtained using the symbolic algebra software Maple™ 2024 Maplesoft (2024).For the sake of simplicity, only nine coefficientsP_{ij} of the covariance matrix are presented, as these are the ones used in the performance indicators given in (4.19), (4.20), and (4.21).

$$
\begin{aligned}
P_{55} &= q_{\dot{r}} \frac{I_x^2 k_t^2 m_s^2 + 2m_u^2\left(I_x^2 k_s^2 + a^4 m_s^2 (k_s + 2k_r)^2\right)}{2c_s m_u m_s^2 I_x^2} + \\
&\quad + \frac{2I_x^2 c_s^2 k_t + I_x^2 m_s k_s (k_s - 2k_t) + (2a^2 c_s^2 k_t + (2k_r + k_s - 2k_t)(2k_r + k_s) I_x)}{2c_s m_u m_s^2 I_x^2} \\
P_{57} &= q_{\dot{r}} \frac{2c_s^2 k_t + k_s^2 (m_s + 2m_u) - k_s k_t m_s}{2c_s m_s^2} \\
P_{58} &= -q_{\dot{r}} \frac{0.5(k_s + 2k_r)(k_s + 2k_r - k_t) I_x a + a^3\left(c_s^2 k_t + m_u (k_s + 2k_r)^2\right)}{c_s I_x^2} \\
P_{66} &= q_{\dot{r}} \frac{I_x^2 k_t^2 m_s^2 + 2m_u^2\left(I_x^2 k_s^2 + a^4 m_s^2 (k_s + 2k_r)^2\right)}{2c_s m_u m_s^2 I_x^2} + \\
&\quad + \frac{2I_x^2 c_s^2 k_t + I_x^2 m_s k_s (k_s - 2k_t) + (2a^2 c_s^2 k_t + (2k_r + k_s - 2k_t)(2k_r + k_s) I_x)}{2c_s m_u m_s^2 I_x^2} \\
P_{67} &= q_{\dot{r}} \frac{2c_s^2 k_t + k_s^2 (m_s + 2m_u) - k_s k_t m_s}{2c_s m_s^2} \\
P_{68} &= q_{\dot{r}} \frac{0.5(k_s + 2k_r)(k_s + 2k_r - k_t) I_x a + a^3\left(c_s^2 k_t + m_u (k_s + 2k_r)^2\right)}{c_s I_x^2} \\
P_{77} &= q_{\dot{r}} \frac{2c_s^2 k_t + k_s^2 (m_s + 2m_u)}{2m_s^2 c_s} \\
P_{78} &= 0 \\
P_{88} &= q_{\dot{r}} \frac{0.5\left(k_s + 2k_r\right)^2 I_x + a^2\left(c_s^2 k_t + m_u (k_s + 2k_r)^2\right)}{I_x^2 c_s}
\end{aligned}
$$

Certain parameter dependencies exhibit structural similarities to the expressions derived in the QCM. For example, the sprung mass acceleration variance, represented by P_{77}, closely mirrors the form of its quarter-car counterpart P_{33} (see Section **3.3**). Furthermore, the unsprung mass acceleration variances ($P_{55} = P_{66}$) differ significantly from their QCM equivalent P_{44}, due to the inclusion of rotational inertia effects and the influence of the anti-roll bar.

For instance, the cross-covariance $P_{78} = 0$ indicates that, within the structure of this model, the vertical and roll accelerations of the sprung mass are statistically uncorrelated. This result reinforces the equality shown in Equation (4.5), thereby verifying the formulation of the proposed ride comfort index. Moreover, the variance of the vertical acceleration P_{77} is independent of the ARB stiffness k_r, which is reasonable since the bar does not act during pure in-phase vertical (bounce) motions. Lastly, the roll acceleration variance component P_{88}

depends on k_r, which provides generalizing support to the claim made by several authors Smith et al. (2010); Xu et al. (2015) that the degradation in ride comfort associated with ARBs is primarily due to increased angular roll accelerations.

By systematically substituting these coefficients into the performance indicators for comfort and road holding, it is possible to derive an analytical expression for these metrics.

$$J_1 = \sqrt{\frac{\pi G_{dd} V_x \mathcal{N}_1}{2 I_x^2 c_s m_s^2}} \tag{4.24}$$

$$J_2 = \sqrt{\frac{\pi G_{dd} V_x \mathcal{N}_2}{I_x^2 c_s m_s^2 a^2}} \tag{4.25}$$

where $\mathcal{N}_1$ and $\mathcal{N}_2$ are given by

$$\mathcal{N}_1 = 2\Big(2\left(k_r + \frac{k_s}{2}\right)^2 I_x + a^2\big(c_s^2 k_t + (k_s + 2k_r)^2 m_u\big)\Big) l^2 m_s^2 + I_x^2\big(2c_s^2 k_t + k_s^2(m_s + 2m_u)\big)$$

and

$$\begin{aligned}
\mathcal{N}_2 = 0.125\, I_x^2 a^2 k_s^2 m_s^3 + \Bigg[&\big((4k_r k_s + 4k_r^2 + k_s^2)m_u^3 + c_s^2 k_t m_u^2\big)\, a^6 \\
&+ \big((1.5k_s^2 + (6k_r - k_t)k_s + 6k_r^2 - 2k_r k_t)m_u^2 + c_s^2 k_t m_u\big)\, I_x a^4 \\
&+ \big((1.5k_s^2 + (3k_r - k_t)k_s + 0.5k_t^2 + 3k_r^2 - k_r k_t)m_u + 0.5c_s^2 k_t\big)\, I_x^2 a^2 \\
&+ \big(0.5k_r k_s + 0.125k_s^2 + 0.5k_r^2\big)\, I_x^3 \Bigg] m_s^2 \\
&+ \big((1.5k_s^2 - k_s k_t)m_u^2 + c_s^2 k_t m_u\big)\, I_x^2 a^2 m_s + a^2 I_x^2 m_u^2 (c_s^2 k_t + k_s^2 m_u).
\end{aligned}$$

Similar to the work presented in the previous section, this section outlines the analytical derivation of the optimal suspension parameters. It should be noted that while the ARB is a component of the vehicle suspension system, its design parameters are typically determined based on vehicle requirements during cornering or under roll-over conditions. However, such scenarios fall outside the scope of the current model's assumptions (i.e., straight-line driving, steady-state conditions, and no driver inputs). For this reason, the optimization process detailed below focuses on identifying the optimal suspension stiffness k_s and damping c_s values as a function of the ARB selected for the vehicle. Furthermore, the analysis quantifies the deviation of these new optimal parameters from those obtained using the QCM.

4.4.1 Suspension optimization for comfort in the single axle HCM

By applying multivariable calculus, it is established that for $c_s \neq 0$, the performance indicator J_1, treated as the objective function, achieves an absolute minimum when:

$$\nabla J_1(k_s, c_s) = 0 \tag{4.26}$$

Solving the first partial derivative yields:

$$\frac{\partial J_1}{\partial k_s} = 0 \iff \frac{(2k_r + k_s)\left(2a^2 m_u + I_x\right) l^2 m_s^2 + I_x^2 k_s m_s + 2 I_x^2 k_s m_u}{I_x^2 c_s m_s^2} = 0 \iff$$

$$\iff k^\star_{s,J_1} = -\frac{2k_r l^2 m_s^2 \left(2a^2 m_u + I_x\right)}{(m_s + 2m_u) I_x^2 + l^2 m_s^2 I_x + 2a^2 l^2 m_s^2 m_u} \tag{4.27}$$

Since it is reasonable to assume that $k_r > 0$, it is observed that the optimal suspension stiffness for comfort would theoretically be negative. However, for practical purposes—just as in the —it is assumed that $k_s > 0$, and that the optimal stiffness for comfort corresponds to the smallest physically feasible value.

The second partial derivative gives the optimal damping coefficient for comfort as:

$$\frac{\partial J_1}{\partial c_s} = 0 \iff \frac{\left[a^2\left(c_s^2 k_t - m_u(2k_r + k_s)^2\right) - (2k_r + k_s)^2 I_x\right] l^2 m_s^2 + I_x^2 (2c_s^2 k_t - k_s^2 (m_s + 2m_u))}{2 I_x^2 c_s^2 m_s^2} = 0$$

$$\implies c^\star_{s,J_1} = \frac{2\sqrt{k_t\left(a^2 l^2 m_s^2 + I_x^2\right)\left(\left(a^2 m_u + 0.5 I_x\right)(k_r + 0.5k_s)^2 l^2 m_s^2 + I_x^2 k_s^2 \left(\frac{m_s}{8} + \frac{m_u}{4}\right)\right)}}{k_t\left(a^2 l^2 m_s^2 + I_x^2\right)} \tag{4.28}$$

where $c^\star_{s,J_1}$ denotes the damping coefficient that minimizes ride discomfort for a given non-zero suspension stiffness and ARB stiffness. When including the ARB, it is observed that the optimal damping is no longer linearly proportional to the suspension stiffness, as it now also depends on the ARB stiffness. Additionally, it is important to note that for $l = 0$ — that is, canceling the arm that makes accelerations due to roll, only vertical acc remain in the driver

— the original optimal damping formula for the is recovered:

$$c^{\star}_{s,J_1} = \frac{2\sqrt{k_t(I_x^2 + \cancel{a^2 l^2 m_s^2})\Big((a^2 m_u + 0.5 I_x)(k_r + 0.5k_s)^2 \cancel{l^2 m_s^2} + I_x^2 k_s^2(\frac{m_s}{8} + \frac{m_u}{4})\Big)}}{2k_t(\cancel{a^2 l^2 m_s^2} + I_x^2)} \iff$$

$$\iff c^{\star}_{s,J_1} = \frac{2\sqrt{k_t I_x^4 k_s^2\left(\frac{m_s}{8} + \frac{m_u}{4}\right)}}{k_t I_x^2} = k_s\sqrt{\frac{m_s + 2m_u}{2k_t}} \tag{4.29}$$

Figure 4.3 shows the comfort indicator J_1 against damping using the vehicle parameters specified in Table 4.1. This reference vehicle will be used for subsequent examples throughout this chapter. The figure compares scenarios with and without an anti-roll bar. The ARB stiffness value (k_r) for this comparison was selected based on values proposed by other authors for vehicles of similar dimensions Hassan et al. (2023).

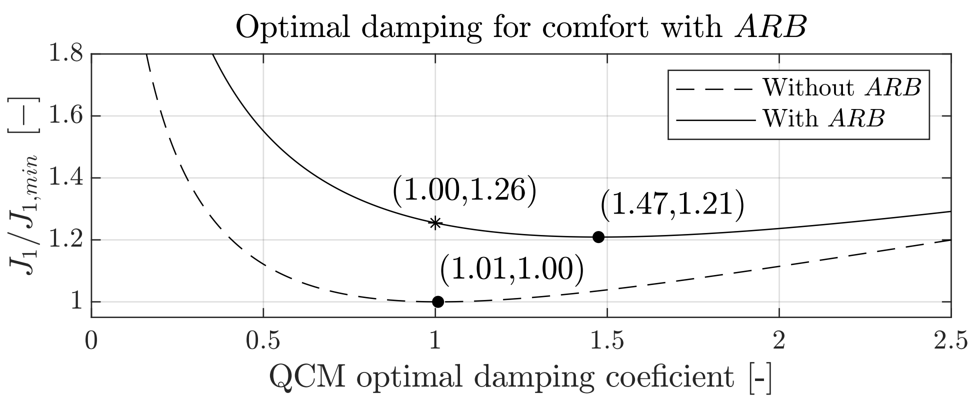

Figure 4.3: Comfort index J_1 normalized by the maximum achievable comfort $J_{1,min}$, as a function of damping c_s for $k_s = 10000$ $[N/m]$, shown without ARB and with ARB $k_r = 7500$ $[N/m]$. A black dot marks the optimal damping value c_{s,opt,J_1} for each curve. Dots mark the optimal c_s from the HCM; asterisks show the optimal value from the QCM.

Three important conclusions can be drawn from Figure 4.3. First, the results demonstrate that incorporating an anti-roll bar inevitably leads to an increase in driver discomfort (i.e., a higher J_1 value), even when suspension damping is optimized using the updated values. Second, including an anti-roll bar requires significantly higher suspension damping to achieve optimal comfort. Third, keeping the optimal damping value derived from the QCM, instead of the new optimum calculated for the case with ARB, results in a performance penalty of approximately 5%.

Table 4.1: Properties of the reference vehicle in the single axle Half Car Model.

Symbol	**Value**	**Description**
m_s	600 $[kg]$	Sprung mass
$I_{x,ref}$	1050 $[kg \cdot m^2]$	Sprung mass rotational inertia: Roll
m_u	40 $[kg]$	Unsprung mass
k_t	110 $[kN/m]$	Tyre vertical stiffness
a	1.25 $[m]$	Half track width
l	0.6 $[m]$	Distance from headrest to chassis center of mass

To further illustrate this trade-off, Figure 4.4 presents the variation of the comfort indicator J_1 as a function of the ARB stiffness k_r. This figure compares two scenarios: one using the optimal damping derived from the QCM, and the other using the optimal damping calculated by the methodology proposed in this research (which incorporates k_r). First, it is clear that as more ARB stiffness is introduced, comfort is only worsened, a conclusion already noted in the literature Chen et al. (2019). Second, by using the optimal damping for this case, this degradation can be attenuated, as compared here against the case of using the optimal damping of the QCM.

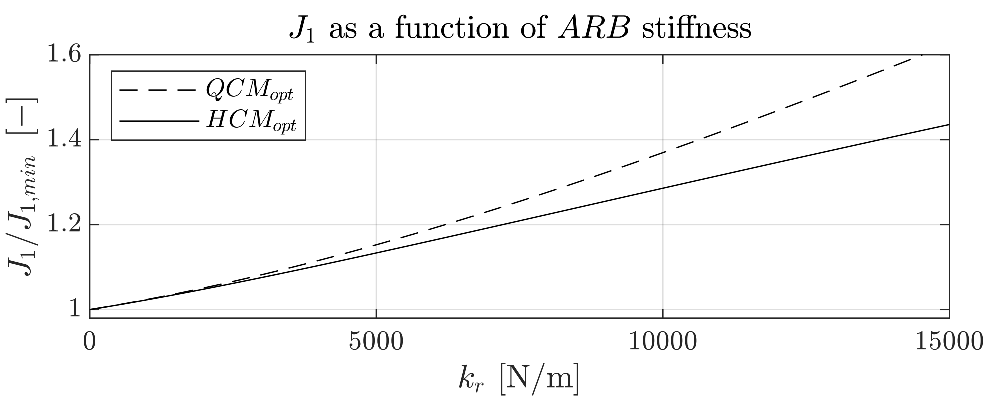

Figure 4.4: Comfort index J_1 normalized by the maximum achievable comfort $J_{1,min}$, as a function of ARB stiffness k_r. Solid line: optimal coefficients from this model (includes k_r); dashed line: from the QCM (neglects k_r).

4.4.2 Suspension optimization for road holding in the single axle HCM

Analogously to the comfort optimal, for $c_s \neq 0$, the performance indicator J_2 achieves a global minimum when:

$$\nabla J_2(k_s, c_s) = 0 \tag{4.30}$$

Each partial derivative is expressed as:

$$\frac{\partial J_2}{\partial k_s} = 0 \iff \frac{\begin{aligned}&\Big[(0.5\,k_r + 0.25\,k_s)\,I_x^3 + (3\,k_s + 3\,k_r - k_t)\,m_u I_x^2 a^2 \\ &\quad + (3\,k_s + 6\,k_r - k_t)\,m_u^2 I_x a^4 + (4\,k_r + 2\,k_s)\,m_u^3 a^6\Big]\,m_s^2 \\ &+ (3\,k_s - k_t)\,m_u^2 I_x^2 a^2 m_s + 2\,a^2 I_x^2 m_u^3 k_s + 0.25\,I_x^2 a^2 k_s m_s^3\end{aligned}}{I_x^2 a^2 c_s m_s^2} = 0$$

$$\frac{\partial J_2}{\partial c_s} = 0 \iff \frac{\begin{aligned}&-0.125\,I_x^2 a^2 k_s^2 m_s^3 \\ &+ \Big[\big((-4\,k_r^2 - k_s^2 - 4\,k_r k_s)\,m_u^3 + c_s^2 k_t m_u^2\big)a^6 \\ &\quad + \big((-1.5\,k_s^2 + (-6\,k_r + k_t)\,k_s + 2\,k_r k_t - 6\,k_r^2)\,m_u^2 + c_s^2 k_t m_u\big)I_x a^4 \\ &\quad + \big((-1.5\,k_s^2 + (-3\,k_r + k_t)\,k_s + k_r k_t - 0.5\,k_t^2 - 3\,k_r^2)\,m_u + 0.5\,c_s^2 k_t\big)I_x^2 a^2 \\ &\quad + (-0.125\,k_s^2 - 0.5\,k_r^2 - 0.5\,k_r k_s)\,I_x^3\Big]m_s^2 \\ &+ \big(k_s k_t - 1.5\,k_s^2\big)m_u^2 I_x^2 a^2 m_s + c_s^2 k_t m_u I_x^2 a^2 m_s \\ &+ \big(-k_s^2 m_u^3 + c_s^2 k_t m_u^2\big)I_x^2 a^2\end{aligned}}{c_s^2 m_s^2 I_x^2 a^2} = 0$$

and solving these two conditions simultaneously results in:

$$k_{s,J_2}^{\star} = \frac{4\,m_u^2\,I_x^2\,a^2\,m_s\,k_t - 2\,(k_r\,I_x^3 - (2\,k_t - 6k_r)\,m_u\,a^2\,I_x^2 - (2\,k_t - 12k_r)\,m_u^2\,a^4\,I_x + 8\,k_r\,m_u^3\,a^6)\,m_s^2}{I_x^2\,a^2\,m_s^3 + (8\,m_u^3\,a^6 + 12\,m_u^2\,I_x\,a^4 + 12\,I_x^2\,a^2\,m_u + I_x^3)\,m_s^2 + 12\,I_x^2\,a^2\,m_s\,m_u^2 + 8\,I_x^2\,a^2\,m_u^3} \tag{4.31}$$

and

$$c^{\star}_{s,J_2} = \frac{m_s I_x \mathcal{N}_3^{\frac{1}{2}}}{(k_t \mathcal{D}_1 \mathcal{D}_2)^{\frac{1}{2}}}. \tag{4.32}$$

where $\mathcal{N}_3$, $\mathcal{D}_1$, and $\mathcal{D}_2$ are defined as follows:

$$\begin{aligned}
\mathcal{N}_3 = & -4I_x a^4 k_r k_t m_s^3 m_u^2 - 2I_x^2 a^2 k_r k_t m_s^3 m_u + 12 I_x^3 k_r^2 m_s m_u^2 + I_x^3 k_t^2 m_s^2 m_u + 8a^6 k_r^2 m_s^3 m_u^3 \\
& + 48 a^6 k_r^2 m_s^2 m_u^4 + 96 a^6 k_r^2 m_s m_u^5 + 4a^6 k_t^2 m_s^2 m_u^4 + 96 I_x a^4 k_r^2 m_u^5 + 48 I_x^2 a^2 k_r^2 m_u^4 \\
& + 4I_x^2 a^2 k_t^2 m_u^4 + 6I_x^3 k_r^2 m_s^2 m_u + 64 a^6 k_r^2 m_u^6 + I_x^3 k_r^2 m_s^3 + 8I_x^3 k_r^2 m_u^3 \\
& + 16 a^6 k_r k_t m_s^2 m_u^4 + 32 a^6 k_r k_t m_s m_u^5 + 12 I_x a^4 k_r^2 m_s^3 m_u^2 + 72 I_x a^4 k_r^2 m_s^2 m_u^3 \\
& + 144 I_x a^4 k_r^2 m_s m_u^4 - 32 I_x a^4 k_r k_t m_u^5 + 4I_x a^4 k_t^2 m_s^2 m_u^3 - 8I_x a^4 k_t^2 m_s m_u^4 \\
& + 6I_x^2 a^2 k_r^2 m_s^3 m_u + 36 I_x^2 a^2 k_r^2 m_s^2 m_u^2 + 72 I_x^2 a^2 k_r^2 m_s m_u^3 - 16 I_x^2 a^2 k_r k_t m_u^4 \\
& + I_x^2 a^2 k_t^2 m_s^3 m_u + 8I_x^2 a^2 k_t^2 m_s^2 m_u^2 + 4I_x^2 a^2 k_t^2 m_s m_u^3 + 2I_x^3 k_r k_t m_s^2 m_u \\
& + 4I_x^3 k_r k_t m_s m_u^2
\end{aligned}$$

$$\mathcal{D}_1 = I_x^3 m_s^2 + a^2 (m_s^3 + 12 m_s^2 m_u + 12 m_u^2 m_s + 8 m_u^3) I_x^2 + 12 m_s^2 m_u^2 a^4 I_x + 8a^6 m_s^2 m_u^3$$

$$\mathcal{D}_2 = 2m_s^2 m_u^2 a^4 + 2m_s^2 m_u I_x a^2 + m_s^2 I_x^2 + 2m_u I_x^2 m_s + 2I_x^2 m_u^2$$

The extensive nature of these analytical expressions is immediately apparent. To effectively illustrate the influence of the anti-roll bar (ARB) on the optimal suspension stiffness, Figure 4.5 shows the road holding indicator against stiffness, for the reference vehicle, comparing scenarios with and without an ARB.

Several observations can be made from Figure 4.5. First, incorporating an ARB without modifying the suspension stiffness k_s degrades road holding performance. Second, the optimal parameters derived from the QCM do not necessarily align with those for the HCM, even when no ARB is present. Thirdly, comparing the performance achieved using the QCM optima versus the true HCM optima for the ARB-equipped case reveals a relatively small performance penalty of approximately 2% for road holding in this specific configuration.

Furthermore, analysis of Eq. (4.31) reveals an important characteristic: the suspension stiffness should decrease as the ARB stiffness increases, leading to $k^{\star}_{s,J_2}$ becoming negative after a

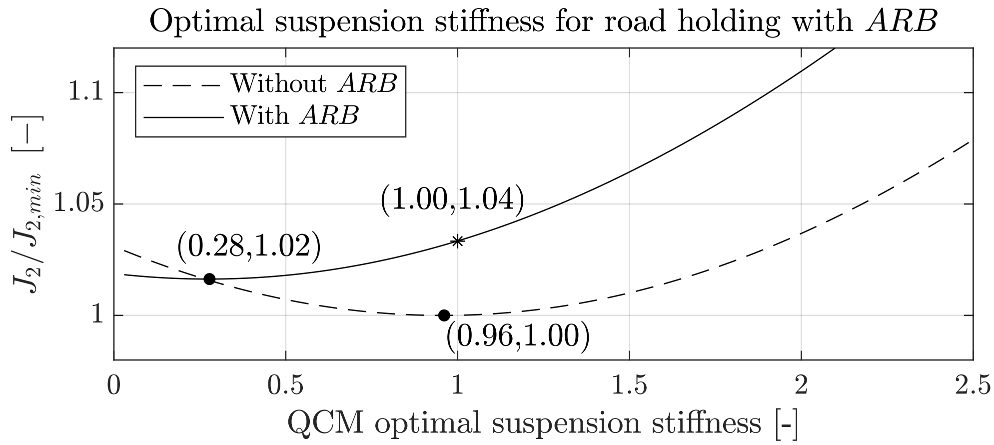

Figure 4.5: Road holding index J_2 as a function of suspension stiffness k_s, with and without an ARB. Dots mark the optimal k_s from the HCM; asterisks show the value from the QCM.

critical point. However, springs with negative stiffness are not physically realizable in passive suspensions, therefore we define the maximum usable ARB stiffness, i.e. the critical value, as the one that results in $k^{\star}_{s,J_2} = 0$, given by Eq. (4.33)

$$k_{r,\text{crit}} = \frac{2\left((m_s + m_u)I_x + a^2 m_s m_u\right) I_x m_u k_t a^2}{m_s \left(I_x + 2m_u a^2\right)^3}. \tag{4.33}$$

For ARB stiffness values below this critical point ($k_r < k_{r,\text{crit}}$), a unique, positive optimal suspension stiffness $k^{\star}_{s,J_2}$ exists, while for $k_r \geq k_{r,\text{crit}}$, the optimal stiffness is non-positive. In the latter, to minimize the road holding indicator J_2, the minimum feasible suspension stiffness (e.g., $k_s = 0$ or another practical lower bound) should be employed.

Regarding the optimal damping, examining Eq. (4.32) reveals that c_{s,opt,J_2} remains independent of the main suspension stiffness k_s, similar to the QCM result for road holding. However, unlike the QCM case, the optimal damping now explicitly depends on the anti-roll bar stiffness k_r. To illustrate this effect, Figure 4.6 shows the J_2 against damping for the same vehicle, comparing the cases with and without an anti-roll bar.

Analogous to the observations for suspension stiffness, incorporating an ARB while keeping the damping coefficient constant leads to degraded road holding performance. When comparing the QCM and HCM, their optimal damping values are very similar in the absence of an ARB. However, when the ARB is included, the HCM suggests that the suspension requires a slightly higher optimal damping coefficient. Nevertheless, this increase in optimal damping yields

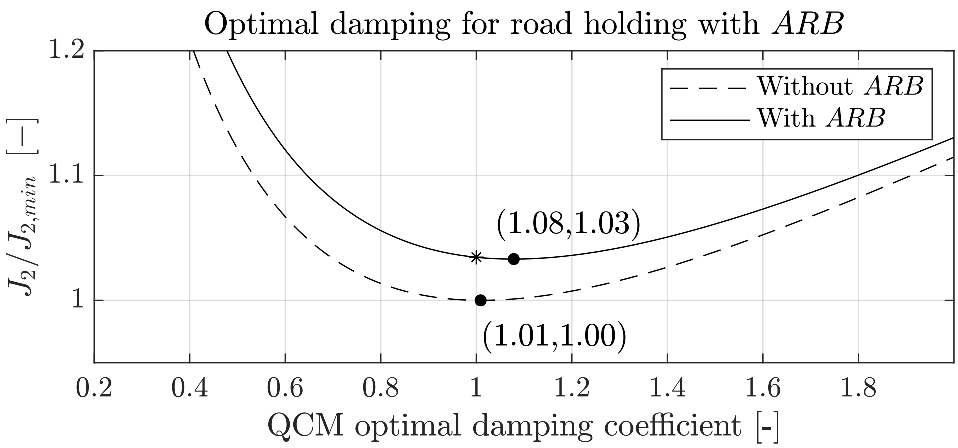

Figure 4.6: Road holding index J_2 as a function of suspension damping c_s, with and without an ARB. Dots mark the optimal c_s from the HCM; asterisks show the value from the QCM.

only a minimal improvement in the J_2 indicator (less than 1%), offering slight mitigation of the performance degradation caused by the ARB.

Furthermore, comparing the minimum achievable J_2 values (black dots) between the cases with and without ARB for both Figures, it reveals that including the ARB increases the minimum possible J_2, leading to a performance penalty in road holding. To quantify this relationship broadly, Figure 4.7 shows the road holding indicator J_2 as a function of the anti-roll bar stiffness k_r. Two scenarios are presented: one utilizing the optimal k_s and c_s derived from the QCM (neglecting k_r), and another using the optimal parameters derived from this HCM analysis (which accounts for k_r):

Figure 4.7 leads to two important conclusions. First, it reinforces that incorporating an ARB necessitates different optimal suspension coefficients (k_s and c_s) compared to those derived from the simpler QCM (which overlooks k_r), generally requiring slightly lower suspension stiffness and slightly higher damping. Second, and perhaps more significantly, the figure demonstrates that increasing the ARB stiffness (k_r) consistently elevates the road holding indicator (J_2), thereby highlighting a conflict between the ARB's established cornering benefits and its detrimental impact on road holding performance under the evaluated straight-line, steady-state operating conditions.

Finally, recapping the overall impact of the ARB based on the results of this research: while its detrimental effect on ride comfort (J_1) is well established in the literature, this research

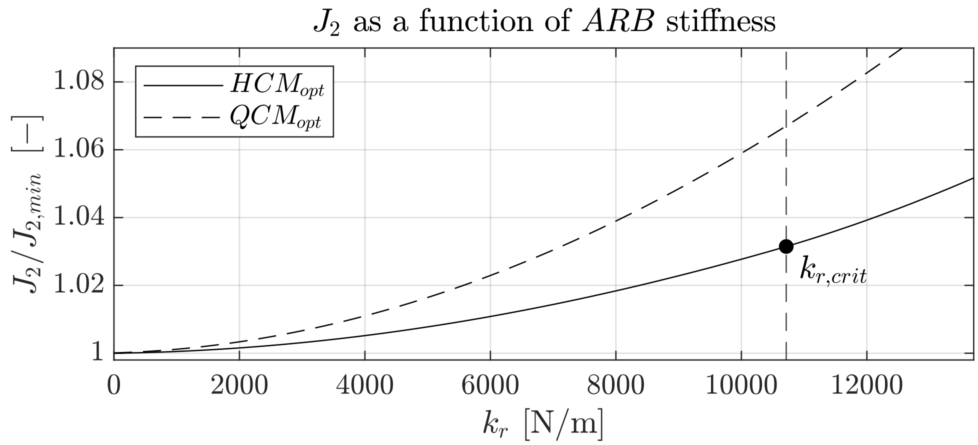

Figure 4.7: Road holding index J_2 as a function of ARB stiffness k_r. Solid line: optimal coefficients from this model (includes k_r); dashed line: from the QCM (neglects k_r).

analytically demonstrates that increasing ARB stiffness also degrades potential road holding performance (J_2) under the evaluated straight-line conditions. This latter finding appears less intensively addressed or quantified analytically in existing literature compared to the well-known comfort trade-off.

4.5 Summary

In this chapter, the Half Car Model was developed as an extension of the Quarter Car Model (QCM), incorporating the rotational dynamics of the chassis and allowing the inclusion of interconnection elements such as anti-roll bars, which are not representable within the QCM due to its limited structure.

After formulating the dynamic equations and establishing the state-space representation for the single-axle HCM, the performance indices for ride comfort and road holding were redefined. The system's stationary response to uncorrelated random excitations was analyzed using covariance analysis, yielding explicit expressions for both indicators, explicitly accounting for the presence of an ARB.

Based on these expressions, an optimization procedure was conducted to determine the optimal suspension stiffness and damping values, while also comparing them to those obtained from the QCM. The influence of anti-roll bar stiffness on these optima was examined, revealing that its inclusion significantly alters the optimal values of both parameters. Furthermore, it was shown that incorporating an ARB leads to a reduction in both ride comfort and road holding performance under the conditions defined by this model.

These findings correspond to the first and most significant results of this research. In the next chapter, the two-axle Half Car Model is analyzed in order to evaluate the impact of different correlation types between road disturbances.

Chapter 5

Suspension optimization for the two axle Half Car Model

This chapter extends the suspension analysis to the two-axle Half Car Model (HCM), enabling the evaluation of pitch dynamics and interactions between the front and rear axles. Unlike the single-axle configuration, this formulation introduces the effects of correlated road inputs between axles, modeled through a time delay in the covariance analysis. Due to the analytical intractability of the resulting system, a numerical approach is employed to solve the Lyapunov equation and determine the optimal suspension parameters for both comfort and road holding. Through a series of numerical optimization studies—considering both symmetric and asymmetric vehicle configurations—and a final sensitivity analysis, the chapter aims to: evaluate how the optimal tuning in the two-axle HCM deviates from that predicted by the simpler QCM; quantify the influence of inter-axle time delay on suspension performance; and assess the relative importance of model fidelity versus parameter accuracy in suspension design.

5.1 Mathematical formulaiton of the two axle *HCM*

This chapter formally introduces the two-axle Half-Car Model. Whereas the single-axle model presented in the Chapter 4, inherently assumes symmetry with respect to the vehicle's roll axis (center of mass in the frontal view), the two-axle model accommodates potential asymmetries between the front and rear axles (e.g., different unsprung masses, suspension parameters, or distances to the center of gravity). This added capability increases the model's representativeness of pitch dynamics but also its mathematical complexity compared to the single-axle case.

Figure 5.1 shows a schematic representation of the two-axle HCM (lateral view), including its key parameters. The sprung mass (m_s) and its pitch moment of inertia (I_y) represent half of the vehicle chassis. The unsprung masses, m_f (front) and m_r (rear), correspond to the equivalent mass of the wheels and associated suspension components for each axle. These axles are separated by the wheelbase $L = b_1 + b_2$, where b_1 and b_2 are the longitudinal distances from the vehicle's center of gravity (CG) to the rear and front axles, respectively. Each axle's suspension is modeled independently[1] using stiffness parameters (k_f, k_r) and damping coefficients (c_f, c_r). The tires are represented as simple linear vertical springs with stiffness values k_{tf} and k_{tr}. Road disturbances, $r_1(t)$ (acting on the front axle) and $r_2(t)$ (acting on the rear axle), serve as the excitations. The model thus involves 12 primary vehicle parameters ($m_s, I_y, m_f, m_r, k_f, k_r, c_f, c_r, k_{tf}, k_{tr}, b_1, b_2$) and potentially 3 driving scenario parameters (longitudinal velocity V_x, and the road profiles r_1, r_2).

A key aspect of the two-axle model is the relationship between the road irregularities encountered by the front and rear wheels. When the vehicle travels over a specific road feature, the front axle encounters it first, followed by the rear axle after a time delay (t_d) determined by the vehicle's speed (V_x) and wheelbase (L). Therefore, two correlation scenarios for the road inputs $r_1(t)$ and $r_2(t)$ are considered in this study:

- **In-phase inputs:** The first scenario assumes that $r_1(t)$ and $r_2(t)$ are identical and perfectly synchronized ($r_1(t) = r_2(t)$). This simplifies the analysis and approximates the vehicle's behavior at very high speeds, where the time delay between the axles encountering the same irregularity, $t_d = L/V_x$, becomes negligible ($t_d \approx 0$).
- **Inputs with time delay:** The second, more realistic scenario models the inputs as identical but phase-shifted, accounting for the exact time delay $t_d = L/V_x$ for the rear axle to reach the same point on the road profile as the front axle. That is, $r_2(t) = r_1(t - t_d)$. This approach offers a more accurate representation of the vehicle's

[1] Interconnection elements like anti-pitch bars are not considered in this specific chapter's baseline formulation but could be added following similar principles as in Chapter 4.

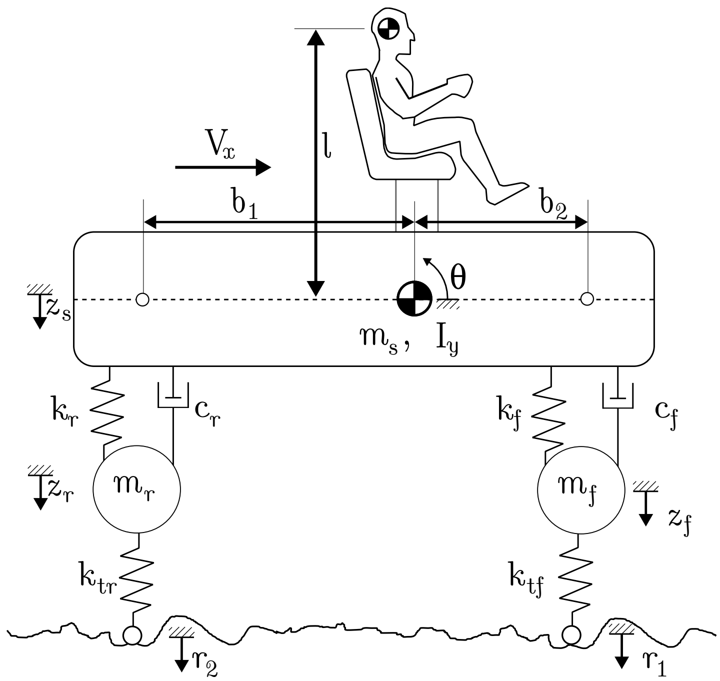

Figure 5.1: Schematic representation of the two-axle Half-Car Model (HCM) (lateral view), illustrating the sprung mass (m_s) with its pitch moment of inertia (I_y), and the unsprung masses (m_f, m_r) for the front and rear axles. Suspension stiffness (k_f, k_r) and damping coefficients (c_f, c_r), along with tire vertical stiffnesses (k_{tf}, k_{tr}), are included. The model allows analysis of vertical bounce and pitch dynamics under two road disturbances ($r_1(t)$ and $r_2(t)$).

behavior across a wider range of speeds, although it introduces greater mathematical complexity, particularly in the analytical treatment of the system inputs within the covariance framework.

The single-axle model analyzed in Chapter 4, primarily investigated the influence of interconnection elements (like anti-roll bars) on suspension performance and optimal tuning relative to the QCM baseline. However, interconnection elements linking the *front and rear* axles (e.g., anti-pitch mechanisms) are less common in standard vehicle configurations. Therefore, the analysis in this chapter will focus exclusively on the two-axle HCM equipped with independent suspension systems at both axles. The primary emphasis will shift towards understanding the influence of the inter-axle time delay (t_d) in road inputs on overall suspension performance and the resulting optimal parameters (k_f, k_r, c_f, c_r), while comparing these results to the QCM baseline.

The equations of motion for the two-axle HCM share similarities with the single-axle model but include terms related to the pitch motion and account for potential asymmetry ($b_1 \neq b_2$). They are presented below:

$$m_f \ddot{z}_f + c_f \dot{z}_f - c_f \dot{z}_s + b_2 c_f \dot{\theta} + (k_{tf} + k_f) z_f - k_f z_s + b_2 k_f \theta = k_{tf} r_1(t) \tag{5.1}$$

$$m_r \ddot{z}_r + c_r \dot{z}_r - c_r \dot{z}_s - b_1 c_r \dot{\theta} + (k_{tr} + k_r) z_r - k_r z_s - b_1 k_r \theta = k_{tr} r_2(t) \tag{5.2}$$

$$m_s \ddot{z}_s - c_f \dot{z}_f - c_r \dot{z}_r + (c_r + c_f) \dot{z}_s + (b_1 c_r - b_2 c_f) \dot{\theta} - k_f z_f - k_r z_r + (k_r + k_f) z_s + (b_1 k_r - b_2 k_f) \theta = 0 \tag{5.3}$$

$$I_y \ddot{\theta} + b_2 c_f \dot{z}_f - b_1 c_r \dot{z}_r + (b_1 c_r - b_2 c_f) \dot{z}_s + (b_2^2 c_f + b_1^2 c_r) \dot{\theta} + b_2 k_f z_f - b_1 k_r z_r + (b_1 k_r - b_2 k_f) z_s + (b_2^2 k_f + b_1^2 k_r) \theta = 0 \tag{5.4}$$

Expressed in matrix form, the system of equations can be expressed as:

$$M\{\ddot{z}\}(t) + C\{\dot{z}\}(t) + K\{z\}(t) = f_1 r_1(t) + f_2 r_2(t) \tag{5.5}$$

Where,

$$M = \text{diag}[m_f \; m_r \; m_s \; I_y] \,, \quad f_1 = [k_{tf} \; 0 \; 0 \; 0]^{\mathrm{T}} \,, \quad f_2 = [0 \; k_{tr} \; 0 \; 0]^{\mathrm{T}} \,,$$

$$C = \begin{bmatrix} c_f & 0 & -c_f & b_2 c_f \\ 0 & c_r & -c_r & -b_1 c_r \\ -c_f & -c_r & c_f + c_r & b_1 c_r - b_2 c_f \\ b_2 c_f & -b_1 c_r & b_1 c_r - b_2 c_f & b_2^2 c_f + b_1^2 c_r \end{bmatrix} ,$$

$$K = \begin{bmatrix} k_{tf} + k_f & 0 & -k_f & b_2 k_f \\ 0 & k_{tr} + k_r & -k_r & -b_1 k_r \\ -k_f & -k_r & k_f + k_r & b_1 k_r - b_2 k_f \\ b_2 k_f & -b_1 k_r & b_1 k_r - b_2 k_f & b_2^2 k_f + b_1^2 k_r \end{bmatrix}$$

The state matrix A and the input matrix B for the state-space representation are defined analogously to the single-axle case presented in the previous chapter, using the updated system matrices M, C, K and input vectors. However, certain aspects related to the performance indicators and the covariance analysis require reformulation for the two-axle model, as detailed below.

5.1.1 Covariance Analysis for the Two-Axle HCM

Compared to the single-axle model (frontal view analysis), analyzing the half-vehicle from a lateral view (two-axle model) necessitates modifications to the covariance analysis setup. While the physical quantities of interest (comfort, road holding) remain conceptually similar, the specific performance indicators and their corresponding weighting vectors are affected by the model's structure, particularly the potential asymmetry ($a \neq b$) relative to the pitch axis (center of gravity). The performance indicators for this model are thus defined as:

$$J_1 = \sqrt{\sigma^2_{\ddot{z}_s} + \sigma^2_{l\ddot{\theta}}} = \sqrt{w_z^T P_{\dot{x}} w_z + w_x^T P_{\dot{x}} w_x} \tag{5.6}$$

$$J_2 = J_{2,f} + J_{2,r} = \sigma_{k_{tf}(r_1 - z_f)} + \sigma_{k_{tr}(r_2 - z_r)} = \sqrt{w_f^T P_{\dot{x}} w_f} + \sqrt{w_r^T P_{\dot{x}} w_r} \tag{5.7}$$

For the comfort indicator (J_1), similar to the single-axle case, the arbitrary distance l is used to represent the vertical distance from the sprung mass CG to the driver's head, allowing the pitch acceleration's contribution to perceived acceleration to be weighted (similar to 4.2b. Furthermore, simplifying the analysis, it is assumed that the driver's seat is located directly above the chassis CG (zero longitudinal offset). This assumption allows the use of the same comfort weighting vectors, w_z (for vertical acceleration $\ddot{z}_s$) and w_x (for pitch acceleration $\ddot{\theta}$ scaled by l), as defined in the previous chapter, adapted to the 8×8 state-space structure.

However, the weighting vectors for the road holding indicator (J_2) differ. By applying an appropriate linear combination of equations (5.1), (5.2), (5.3) and (5.4), the contact force on each tire can be defined as a combination of the system's state variables:

$$m_f \ddot{z}_f + \frac{b_1}{L} m_s \ddot{z}_s - \frac{I_y}{L} \ddot{\theta} = k_{tf}(r_1 - z_f) \tag{5.8}$$

$$m_r \ddot{z}_r + \frac{b_2}{L} m_s \ddot{z}_s + \frac{I_y}{L} \ddot{\theta} = k_{tr}(r_2 - z_r) \tag{5.9}$$

From these relationships, the two weighting vectors required for the road-holding performance indicator (J_2) are obtained. Assuming the state derivative vector used for covariance is

$\dot{x} = [\dot{z}_{uf}, \dot{z}_{ur}, \dot{z}_s, \dot{\theta}, \ddot{z}_{uf}, \ddot{z}_{ur}, \ddot{z}_s, \ddot{\theta}]^T$:

$$w_f^T \dot{x} = k_{tf}(r_1 - z_f) \implies w_f^T = \begin{bmatrix} 0 & 0 & 0 & 0 & m_f & 0 & \frac{b_2}{L} m_s & -\frac{I_y}{L} \end{bmatrix} \tag{5.10}$$

$$w_r^T \dot{x} = k_{tr}(r_2 - z_r) \implies w_r^T = \begin{bmatrix} 0 & 0 & 0 & 0 & 0 & m_r & \frac{b_1}{L} m_s & \frac{I_y}{L} \end{bmatrix} \tag{5.11}$$

Note that when $b_1 = b_2$, the weighting vectors proposed for the previous model are recovered. Thus, based on the formulation of the comfort performance indicator (5.6) and the road-holding performance indicator (5.13), the following expressions are obtained in terms of the covariance matrix coefficients:

$$J_1 = \sqrt{w_z^T P_{\dot{x}} w_z + w_x^T P_{\dot{x}} w_x} = \sqrt{P_{77} + l^2 P_{88}} \tag{5.12}$$

$$J_2 = J_{2,f} + J_{2,r} \tag{5.13}$$

$$J_{2,f} = \sqrt{m_f^2 P_{55} + \left(\frac{b_1}{L} m_s\right)^2 P_{77} + \left(\frac{I_y}{L}\right)^2 P_{88} + 2\left[\frac{b_1 m_s m_f}{L} P_{57} - \frac{I_y m_f}{L} P_{58} - \frac{I_y b_1 m_s}{L^2} P_{78}\right]} \tag{5.14}$$

$$J_{2,r} = \sqrt{m_r^2 P_{66} + \left(\frac{b_2}{L} m_s\right)^2 P_{77} + \left(\frac{I_y}{L}\right)^2 P_{88} + 2\left[\frac{b_2 m_s m_r}{L} P_{67} + \frac{I_y m_r}{L} P_{68} + \frac{I_y b_2 m_s}{L^2} P_{78}\right]} \tag{5.15}$$

The main challenge, as before, lies in obtaining the covariance matrix $P_{\dot{x}}$. The procedure to set up and solve the Lyapunov equation is detailed below. The primary difference compared to the previous analyses arises in the *right-hand side* of the Lyapunov equation when dealing with time-correlated inputs between the front and rear axles. While previously the white noise intensity matrix Q_w could be treated as diagonal (or scalar for single input), for time-correlated inputs, the formulation involves the input autocorrelation matrix $R_w(\tau)$, as described by Popp & Schiehlen (2010):

$$AP_{\dot{x}} + P_{\dot{x}}A^T + BQ_wB^T = 0 \iff \underbrace{AP_{\dot{x}} + P_{\dot{x}}A^T}_{\text{Left hand side}} = \underbrace{-q_{\dot{r}}BB^T}_{\text{Right hand side}} \tag{5.16}$$

Where the matrix Q_w depends on the autocorrelation matrix $R_w(\tau)$ of the white noise input vector process $w(t) = [\dot{r}_1(t)\ \dot{r}_2(t)]^T$ Popp & Schiehlen (2010), represents the correlation of a function with itself at points separated by different times τ Wijker (2009). Assuming the rear wheel input $\dot{r}_2(t)$ is identical to the front wheel input $\dot{r}_1(t)$ but delayed by the transit time $t_d = L/V_x$, the autocorrelation matrix is given by:

$$R_w(\tau) = \mathbb{E}\{w(t)w^T(t-\tau)\} = q_{\dot{r}} \begin{bmatrix} \delta(\tau) & \delta(\tau + t_d) \\ \delta(\tau - t_d) & \delta(\tau) \end{bmatrix} \tag{5.17}$$

Where $q_{\dot{r}} = 2\pi G_{vv} V_x$ is the intensity of the road velocity white noise (assuming G_{vv} is the single-sided PSD level), and $\delta(\tau)$ is the Dirac delta function. The Dirac delta function represents an idealized function that is zero for all values of τ except at $\tau = 0$, where it is infinitely large such that the area under the function equals 1. For further details, refer to Wijker (2009).

For the first scenario of interest, with zero time delay $t_d = 0$ (zero lag), τ is also zero, indicating the maximum correlation between the signals, which are identical and correlate with themselves at a specific instant. Under these conditions, the autocorrelation matrix simplifies to:

$$R_w(0) = q_{\dot{r}} \begin{bmatrix} 1 & 1 \\ 1 & 1 \end{bmatrix} \tag{5.18}$$

Thus, the right-hand side of the Lyapunov equation (5.16) for this in-phase scenario is given by:

$$\underbrace{-BR_wB^T}_{Rigth-side} = -q_{\dot{r}}[b_1b_1^T + b_2b_2^T + b_1b_2^T + b_2b_1^T] \tag{5.19}$$

Examining the components of the right-hand side in detail, since both vector b_1 and vector b_2 (columns of B) are sparse, $-BR_wB^T$ will also be sparse. In particular, the only non-zero terms are given by:

$$-BR_wB^T{}_{55} = -q_{\dot{r}}\frac{k_{tf}^2}{m_f^2} \quad -BR_wB^T{}_{66} = -q_{\dot{r}}\frac{k_{tr}^2}{m_r^2} \quad -BR_wB^T{}_{56} = -BR_wB^T{}_{65} = -q_{\dot{r}}\frac{k_{tf}k_{tr}}{m_fm_r}$$

For the second scenario, the introduction of a time delay enables a more accurate representation of real-world conditions and the dynamic interaction between axles. While this approach more closely approximates reality, it inevitably increases both the model's complexity and the intricacy of its solutions. The stationary solution to the differential equation can be derived by integrating over the autocorrelation matrix definition (5.17):

$$-BR_wB^T = Q = q_{\dot{r}}\left[b_1b_1^T + b_2b_2^T + e^{At_d}b_1b_2^T + b_2b_1^Te^{A^Tt_d}\right] \tag{5.20}$$

Where e^{At_d} represents the matrix exponential, also known as the state transition matrix. This matrix describes how the system state propagates after a time interval t_d. It can be computed using the Taylor series expansion as:

$$e^{At_d} = \sum_{k=0}^{\infty}\frac{(At_d)^k}{k!} = I + At_d + \frac{(At_d)^2}{2!} + \frac{(At_d)^3}{3!} + \cdots \tag{5.21}$$

It is important to note that although the summation extends to infinity, for practical vehicle speeds and wheelbases, t_d is often small enough that the series converges rapidly, and higher-order terms ($k > N$ for some N) become increasingly negligible, allowing for accurate numerical approximation.

As detailed in Appendix **Annex A: Analytical covariance analysis to the two axle Half Car Model**, attempts to solve the Lyapunov equation (5.16) analytically for these two correlation scenarios revealed that obtaining exact, closed-form solutions for the covariance matrix $P_{\dot{x}}$ (and thus for the optimal parameters) is generally infeasible due to the algebraic complexity. Achieving analytical results would likely require significant model simplifications. For this reason, the subsequent analysis in this chapter adopts a numerical approach to solve the Lyapunov equation and perform the suspension optimization for specific vehicle parameter sets, aiming to draw generalizable conclusions from these case studies.

5.2 Numerical Suspension Optimization for the Two-Axle HCM

Given the limitations associated with an analytical approach for the two-axle HCM, this section focuses on numerical optimization of the comfort and road-holding indicators. The main objective is to evaluate how well the optimal predictions derived from the QCM translate to the two-axle HCM, and to characterize the origin of potential deviations.

As previously discussed, two types of correlation between road disturbances are considered. Additionally, since the two-axle HCM involves twelve parameters, the space of possible configurations is theoretically infinite. To manage this complexity, the analysis is restricted to three representative cases, complemented by a sensitivity study. These cases are constructed under symmetry conditions and proportional relationships to enable the formulation of conclusions with broader applicability. Each case introduces new considerations that progressively depart from the assumptions underlying the QCM. The three analyzed cases are defined as follows:

- Case 1: Two simultaneous in-phase inputs on a symmetrical vehicle.
- Case 2: Two simultaneous in-phase inputs on an asymmetrical vehicle.
- Case 3: Two identical inputs with a time delay on a symmetrical vehicle.

To initiate this optimization exploration, an arbitrary baseline case is defined. Based on the order of magnitude indicated in the work by Gandhi et al. (2017), a common baseline case with symmetrical configuration is defined. The properties of this baseline case are presented in Table 5.1.

Table 5.1: Properties of the reference vehicle in the two axle Half Car Model.

Symbol	Value	Description
L	2.5 $[m]$	Wheelbase
$b_{1,ref}$	1.25 $[m]$	Front unsprung mass position
$b_{2,ref}$	1.25 $[m]$	Rear unsprung mass position
m_s	600 $[kg]$	Sprung mass
$I_{y,ref}$	1100 $[kg \cdot m^2]$	Sprung mass rotational inertia: Pitch
$m_{f,ref}$	40 $[kg]$	Front unsprung mass
$m_{r,ref}$	40 $[kg]$	Rear unsprung mass
$k_{tf,ref}$	110 $[kN/m]$	Front tyre vertical stiffness
$k_{tr,ref}$	110 $[kN/m]$	Rear tyre vertical stiffness

To establish an equivalence between the suspended mass of half the chassis used in the HCM and the suspended mass of a quarter of the chassis used in the QCM, the chassis mass is divided into two parts, proportional to the ratios b_2/L and b_1/L, as expressed by:

$$m_{s,f} = m_s \frac{b_1}{L} \tag{5.22}$$

$$m_{s,r} = m_s \frac{b_2}{L} \tag{5.23}$$

The following subsections provide a detailed description of the three proposed cases, each simulated on a Class B road (as defined by the ISO standard referenced in Chapter 2) at a speed of 25 $[m/s]$. While these parameters, as explained in the previous chapter, proportionally influence the RMS value, they do not affect the magnitude of the optimal values that minimize the objective function, at least not until the time delay between $r_1(t)$ and $r_2(t)$ is introduced. For each case, the QCM optimal values are calculated using (3.30), (3.34), and (3.35), while the HCM optimal values are determined through an exhaustive grid search of the coefficients that minimize the indicators in (5.6) and (5.13). For each case, contour plots are presented, varying two of the four optimization variables while keeping the other parameters constant. Both the stiffness and damping coefficients are normalized with respect to the optimal values obtained from the QCM. This normalization serves the purpose of evaluating how closely the QCM optimal parameters align with those of the HCM.

5.2.1 Two simultaneous in-phase inputs on a symmetrical vehicle

This case examines half of the vehicle from a longitudinal perspective, where the vertical stiffness of the tires and the distribution of both sprung and unsprung masses are identical for both wheels ($k_{tf} = k_{tr}$, $m_f = m_r$, $b_1 = b_2$), consistent with the symmetry condition. Additionally, two simultaneous inputs are assumed, where $r_1(t) = r_2(t)$, simulating a scenario with no time delay between disturbances.

Numerical optimization for comfort

Figure 5.2 illustrates the variation of the comfort index for different combinations of stiffness coefficients k_f and k_r, while using the optimal damping for this objective.

As observed in the 2-oF model shown in (3.29), comfort is maximized when J_1 is minimized at $k_r = k_f = 0$. However, this value is not feasible for practical applications. Therefore, for this case and subsequent comfort analyses, a suspension stiffness is selected such that the natural frequency of the unsprung mass is 0.5 $[Hz]$. Since this value is arbitrary, we approximate the

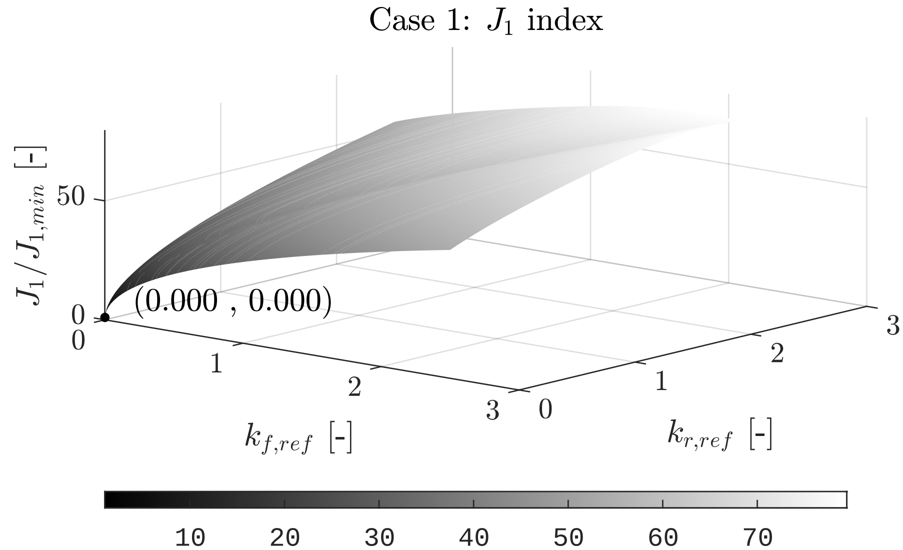

Figure 5.2: Variation of the comfort index J_1 as a function of the normalized stiffness coefficients k_f and k_r, under the condition of simultaneous and in-phase inputs for a symmetrical vehicle. The grayscale gradient indicates the optimal parameter combinations, with the darkest point representing the global minimum at (0.000, 0.000).

natural frequency calculation with the sprung mass as a single degree of freedom oscillator:

$$0.5 \cdot 2\pi = \sqrt{\frac{k_{susp}}{m_{s,i}}} \Longleftrightarrow k_{susp} = \pi^2 m_{s,i} \tag{5.24}$$

While more precise methods exist for calculating the natural frequencies of an N-oF system, this approximation sufficiently establishes a reference value, as using $k_r = k_f = 0$ is impractical. For this stiffness configuration, Figure 5.3 shows the variation of the comfort index for different combinations of damping coefficients c_f and c_r. Furthermore, both comfort and adherence analyses employ figures with a 0.1% accuracy resolution (three decimal places).

Numerical optimization for road holding

Figure 5.4 illustrates the variation of the road-holding index for different combinations of damping and stiffness. Specifically, Figure 5.4a shows the variation of the J_2 index for different combinations of k_f and k_r, using the optimal damping coefficients obtained from the QCM. On the other hand, Figure 5.4b illustrates the variation of the J_2 index for different combinations of c_f and c_r, while using the optimal stiffness coefficients of the QCM.

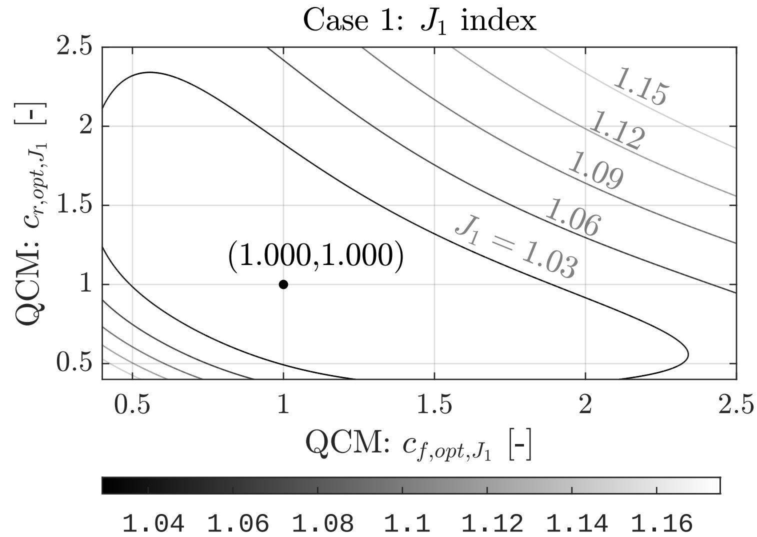

Figure 5.3: Case 1: Variation of the J_1 index as a function of the damping coefficients c_f and c_r, normalized with respect to the QCM optimal values for J_1. The reference stiffness configuration corresponds to k_{susp}, which provides a natural frequency of 0.5 Hz. The grayscale gradient highlights the combinations of parameters, where the darkest point indicates the global minimum at (1.000, 1.000).

From Figures 5.2, 5.3, and 5.4, the following conclusions can be drawn. First, it is observed that for both the comfort and road-holding indicators, the optimal values of the QCM, exactly satisfy the HCM. This indicates that for vehicles with symmetrical mass distribution and operating at speeds where $t_d \approx 0$, the optimal values predicted by the QCM are closely aligned with those of the HCM and, consequently, with the true optimal values (noting that a real vehicle's suspension will obviously be more complex than a 4-oF mathematical model). Furthermore, it is concluded that, under these specific conditions, the optimal stiffness and damping values for comfort and road-holding are independent of the rotational pitch inertia I_y.

Finally, under these symmetrical conditions with simultaneous in-phase inputs, the results were anticipated. However, numerically evaluating this scenario serves to validate the methodology used to characterize the correlation in the excitations, as well as the representativeness of the performance indicators extrapolated from the QCM to the HCM.

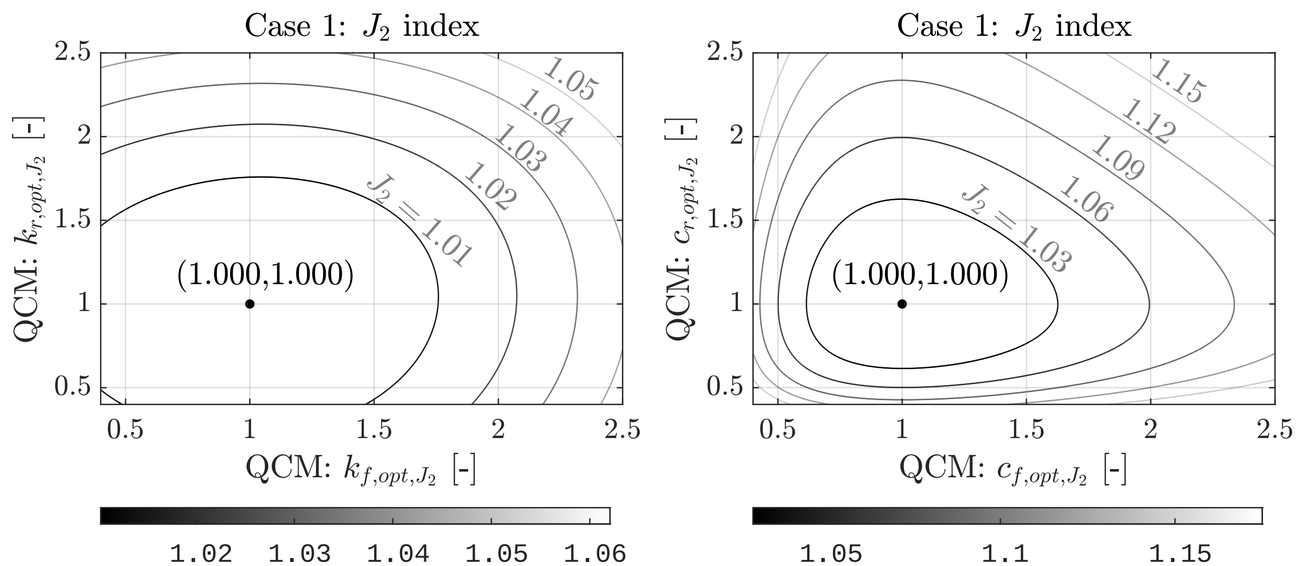

(a) J_2 index as a function of k_f and k_r, using the optimal damping coefficients of the QCM.

(b) J_2 index as a function of c_f and c_r, using the optimal stiffness coefficients of the QCM.

Figure 5.4: Case 1: Variation of the J_2 index for different combinations of normalized stiffness (k_f, k_r) and damping (c_f, c_r) coefficients with respect to the QCM optimal values for J_2, under symmetrical vehicle and zero-lag input conditions. The grayscale gradient highlights the optimal parameter combinations, with the darkest point representing the global minimum.

5.2.2 Two simultaneous in-phase inputs on an asymmetrical vehicle

This case builds upon the previous one but introduces asymmetry in the distribution of masses,which also leads to asymmetry in the vertical stiffness of the tires between the front and rear wheel. A configuration with a 60% front / 40% rear mass distribution is analyzed, where the parameters are adjusted as follows: $k_{tf} = 1.2 \cdot k_{tf,ref}$, $k_{tr} = 0.8 \cdot k_{tr,ref}$, $m_f = 1.2 \cdot m_{f,ref}$, $m_r = 0.8 \cdot m_{r,ref}$, $b_1 = 1.2 \cdot b_{1,ref}$, and $b_2 = 0.8 \cdot b_{2,ref}$.

Numerical Optimization for Comfort

Figure 5.5 shows the variation of the comfort index (J_1) for different combinations of the damping coefficients. It is worth noting that, due to the asymmetrical mass distribution, the suspension stiffness is also asymmetrical to maintain the same natural frequency ratio for both axles, as described in (5.24). Since the optimal damping for comfort is proportional to the suspension stiffness, the optimum observed at (1.000, 1.000) indicates that the comfort-optimal configuration corresponds also to an asymmetrical setup.

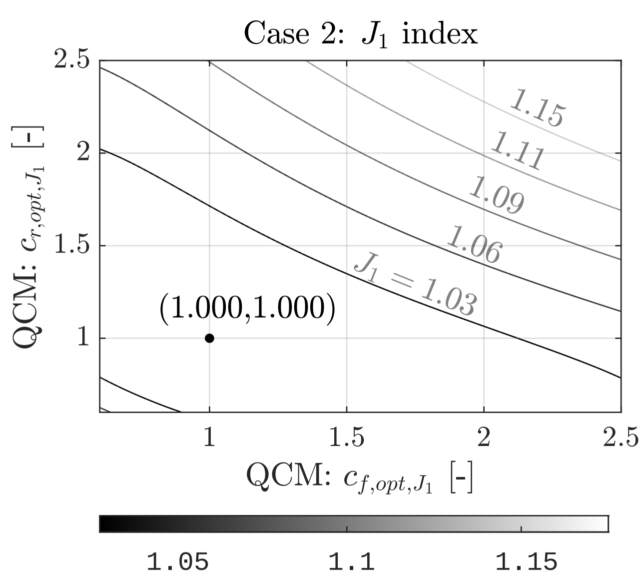

Figure 5.5: Case 2: Variation of the J_1 index as a function of the damping coefficients c_f and c_r, normalized with respect to the QCM optimal values for J_1. The reference stiffness configuration corresponds to k_{susp}, which provides a natural frequency of 0.5 Hz. The grayscale gradient highlights the combinations of parameters, where the darkest point indicates the global minimum at (1.000, 1.000).

Numerical optimization for road holding

Figure 5.6 illustrates the variation of the road-holding index (J_2) for different combinations of damping and stiffness. The methodology used in Figures 5.4a and 5.4b is consistently applied to Figures 5.6a and 5.6b.

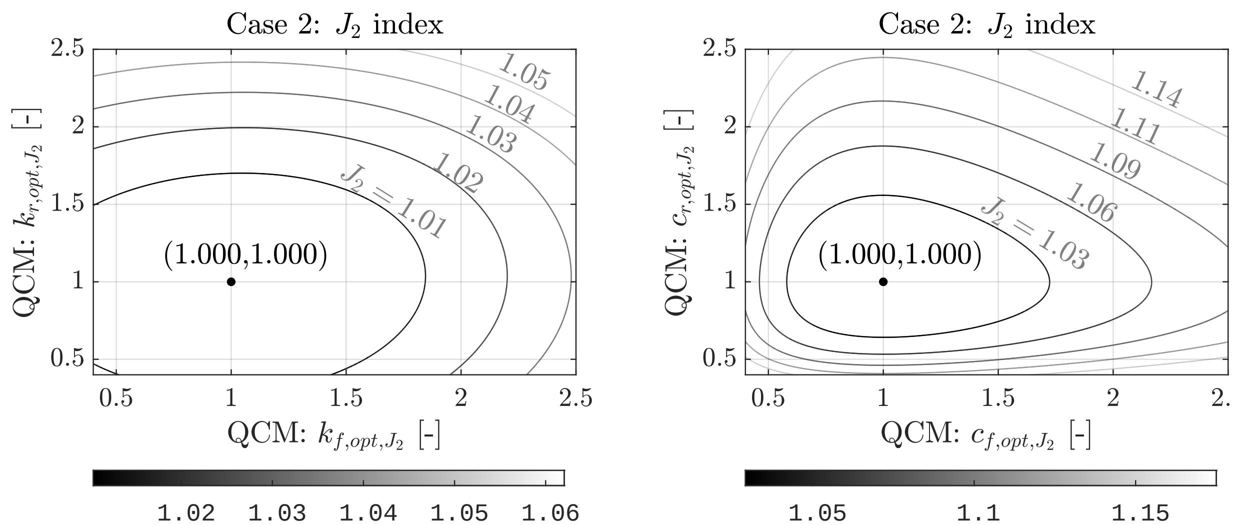

(a) J_2 index as a function of k_f and k_r, using the optimal damping coefficients of the QCM.

(b) J_2 index as a function of c_f and c_r, using the optimal stiffness coefficients of the QCM.

Figure 5.6: Case 2: Variation of the J_2 index for different combinations of normalized stiffness (k_f, k_r) and damping (c_f, c_r) coefficients with respect to the QCM optimal values for J_2, under asymmetrical vehicle and zero-lag input conditions. The grayscale gradient highlights the optimal parameter combinations, with the darkest point representing the global minimum.

For both comfort and road-holding, it is observed that the optimal values align exactly with those predicted by the QCM. Unlike the previous case, this conclusion was neither expected nor predictable. Additionally, since the QCM optimal coefficients also satisfy this case, there is no need for an analytical solution of the HCM for this scenario or the previous one. This case further underscores the effectiveness of the QCM as a reliable tool for suspension optimization.

It is important to emphasize that these conclusions are valid under the specific assumptions of this case, which include proportional asymmetry for the sprung and unsprung masses, as well as the vertical tire's stiffness, alongside the imposed correlation of simultaneous road inputs. In subsequent cases, less idealized scenarios will be explored to investigate conditions that are more generalized and representative of real-world configurations.

5.2.3 Two identical inputs with a time delay on a symmetrical vehicle

This case is an extrapolation of the initial analysis. The aim is to examine the inherent effect caused by the time delay between the road impact on the front axle and, after a time interval t_d, the rear axle. To simplify the analysis, a lateral view of the vehicle is assumed, maintaining symmetry conditions between both axles ($k_{tf} = k_{tr}$, $m_f = m_r$, $b_1 = b_2$). The time delay is modeled according to the approach described in the previous chapter. For this analysis, an arbitrary Class B road was used at a constant speed of 25 $[m/s]$.

Numerical optimization for comfort

Figure 5.7 illustrates the variation of the comfort index (J_1) for different combinations of the damping coefficients at a specific speed.

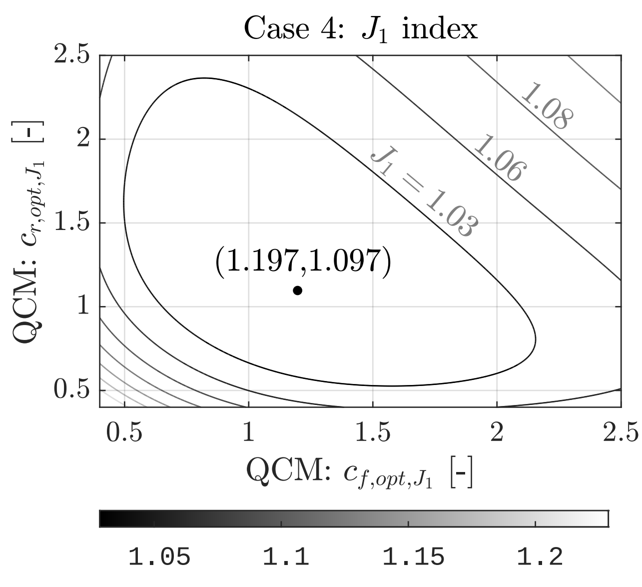

Figure 5.7: Case 3: Variation of the J_1 index as a function of the damping coefficients c_f and c_r, normalized with respect to the QCM optimal values for J_1. The reference stiffness configuration corresponds to k_{susp}, which provides a natural frequency of 0.5 Hz. The grayscale gradient highlights the combinations of parameters, where the darkest point indicates the global minimum at (1.197, 1.097).

Unlike previous cases, despite optimizing a symmetrical vehicle, asymmetric damping coefficients were obtained. This result is particularly interesting considering that symmetrical stiffness was assumed between both axles. This phenomenon is attributed to the time delay imposed between the two disturbances.

To further explore the impact of the time delay, a sensitivity analysis was conducted as a function of speed. Figure 5.8 presents the optimal damping values for speeds ranging from 1 to 70 [m/s].

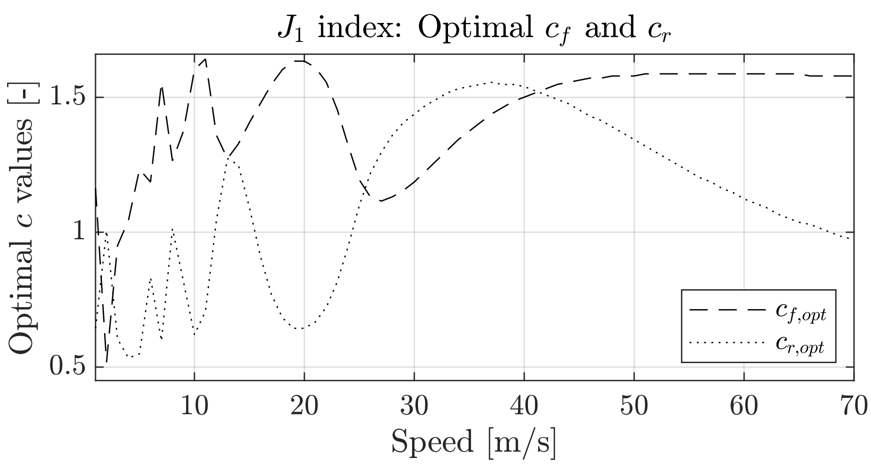

Figure 5.8: Variation of optimal damping coefficients c_f and c_r as a function of speed for the comfort index (J_1). The analysis highlights the asymmetric behavior of the damping coefficients, with c_f generally being slightly higher than c_r at most speeds.

A significant variation in the optimal values is observed as a function of speed. A general trend is identified where c_f is slightly higher than c_r, although there are also segments where c_r exceeds c_f. For practical applications focusing solely on optimizing suspension for comfort, this asymmetric damping effect should be complemented by an asymmetric suspension stiffness, as this analysis assumes $k_f = k_r$.

The key conclusions from this comfort analysis are, first, that contrary to what is derived in (3.30), the optimal suspension configuration for comfort depends on speed, although it remains independent of road roughness. Second, optimizing for comfort requires an asymmetric configuration of damping coefficients between the two axles.

Numerical optimization for road holding

Figure 5.9 illustrates the variation of the road-holding index (J_2) for different combinations of damping and stiffness, assuming a time delay of $t_d = L/V_x = 0.1\,[s]$. Specifically, Figure 5.9a shows the variation of the J_2 index with respect to the suspension stiffness, and Figure 5.9b depicts the variation of the J_2 index with respect to the suspension damping.

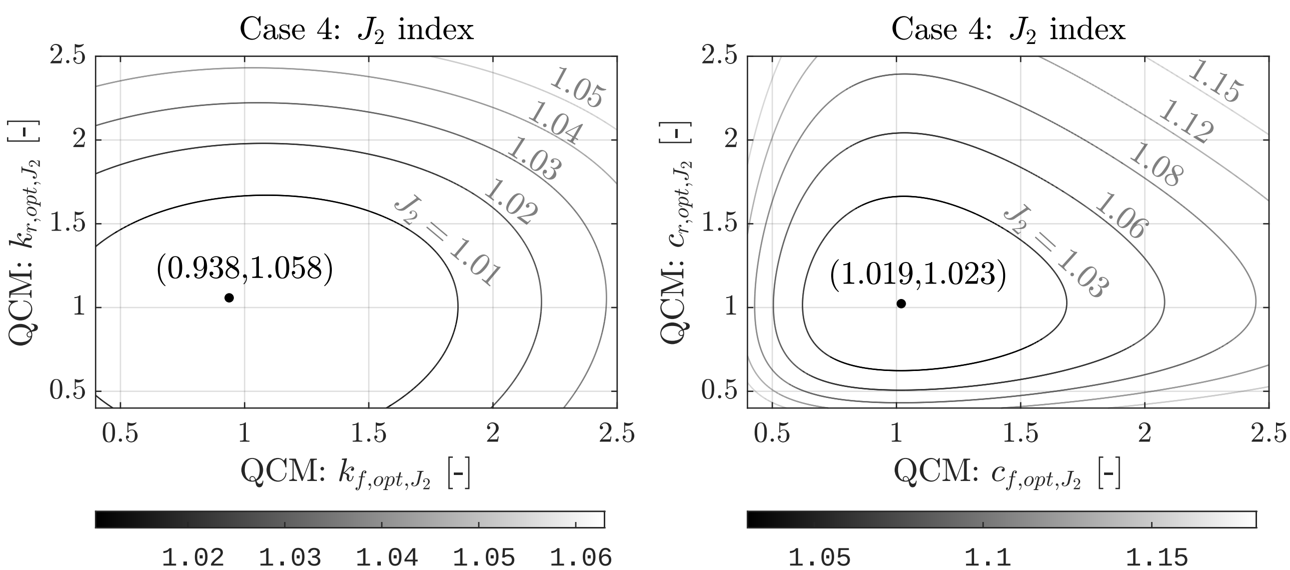

(a) J_2 index as a function of k_f and k_r, using the optimal damping coefficients of the QCM.

(b) J_2 index as a function of c_f and c_r, using the optimal stiffness coefficients of the QCM.

Figure 5.9: Case 3: Variation of the J_2 index for different combinations of normalized stiffness (k_f, k_r) and damping (c_f, c_r) coefficients with respect to the QCM optimal values for J_2, under asymmetrical vehicle and zero-lag input conditions. The grayscale gradient highlights the optimal parameter combinations, with the darkest point representing the global minimum.

As for comfort, even though the distribution is symmetrical, the optimal values obtained from the QCM do not exactly match those from the HCM. Similar to the analysis performed in the previous optimization, this asymmetry is attributed to the time delay.

To better understand the impact of the time delay, a sensitivity analysis was conducted as a function of speed. Figure 5.10 presents the optimal stiffness and damping values for speeds ranging from 1 to 70 [m/s]. Specifically, Figure 5.10a shows the sensitivity analysis for different combinations of stiffness, while Figure 5.10b illustrates the sensitivity analysis for damping, using the remaining optimal parameters of the QCM.

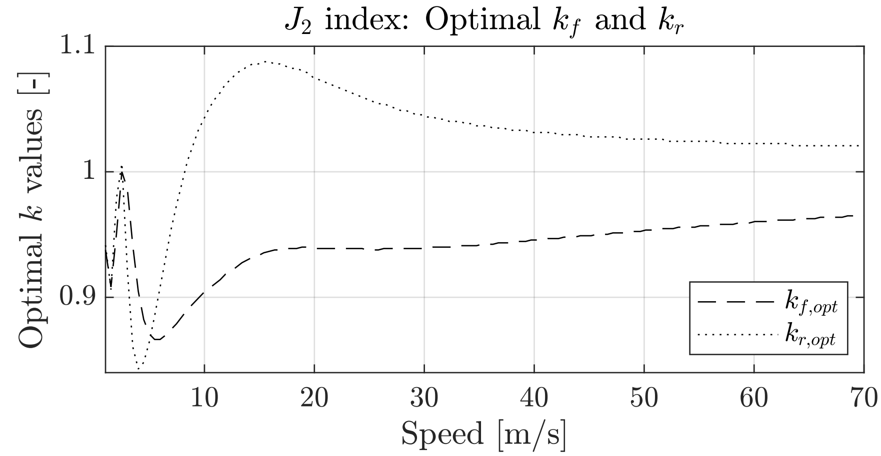

(a) Optimal stiffness coefficients as a function of speed.

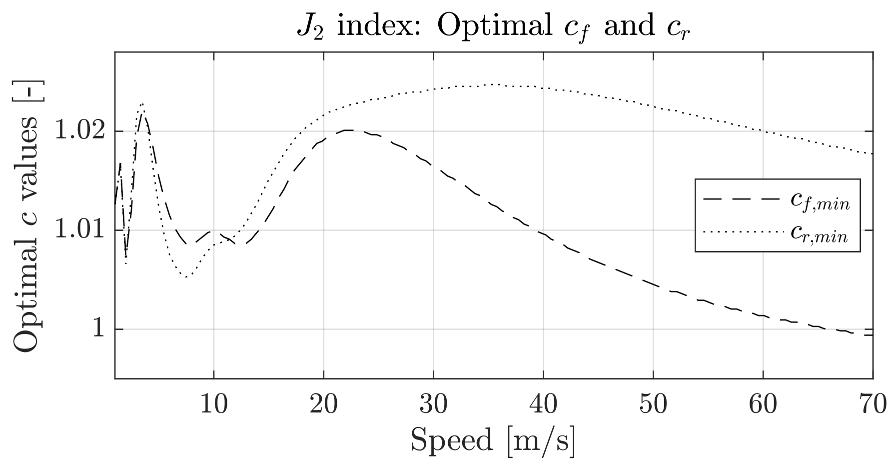

(b) Optimal damping coefficients as a function of speed.

Figure 5.10: Variation of the optimal stiffness and damping coefficients as a function of speed for the road-holding index (J_2). The analysis highlights an asymmetrical behavior, where the optimal *rear* values are slightly higher than the *front*, across most speed ranges.

Comparing Figures 5.8 and 5.10, a smaller deviation from the QCM optimal values is observed for the road-holding index. Contrary to what was concluded in (3.34) and (3.35), the optimal road-holding values are speed-dependent, although they remain independent of road roughness (at least for the way disturbances are defined in this model).

Examining the trends observed in the figures, it is noted that while the behavior is variable for speeds below 10 [m/s], for speeds exceeding this threshold, both the optimal stiffness and damping values are higher for the rear axle than for the front axle.

Specifically, for speeds above approximately 5 $[m/s]$, the magnitude of the optimal stiffness is greater for the rear axle than for the front axle, even when considering a symmetrical mass distribution. This result aligns with the recommendations of several authors, such as Milliken & Milliken (1994) and Kumar et al. (2021), who suggest that the ride frequency of the rear axle should be slightly higher (between 5% and 15%) than that of the front axle to minimize the pitch effect. This provides a mathematical basis to corroborate design recommendations derived from qualitative analysis by certain authors. Conversely, this conclusion contradicts some design guidelines, such as those from Pütz & Serné (2022), which propose equal natural frequencies for both axles to enhance road-holding performance.

This effect persists for speeds exceeding 70 $[m/s]$, indicating that the first case analyzed in this chapter, where no time delay ($t_d = 0$) was considered, represents an oversimplification of reality when compared to this case, specially at lower speeds.

5.3 Sensitivity analysis and discussion of results

The previous sections focused on idealized scenarios, primarily symmetric or with controlled asymmetry proportions,where the optimal values of the QCM closely approximate those that satisfy exactly the HCM. While these cases represented simplified scenarios within a broader range of possible combinations, each allowed for the extraction of conclusions that can be generalized to specific situations. However, the analysis conducted so far has been limited to comparing the deviations of the optimal values between the 4-oF model and the 2-oF model. This section aims to evaluate how these variations impact performance indicators, with the objective of quantifying the improvement achieved by using the HCM over the QCM to optimize suspension's .

The vehicle parameters used in this section are presented in Table 5.2. Although these parameters are similar to the reference values shown in Table 5.1, factors of asymmetry are introduced in different proportions to simulate a less idealized scenario. Regarding the suspension coefficients, their derivation using the HCM with time delay is detailed in **Appendix B: Two identical inputs with a time delay and asymmetrical weight**

distribution.

Table 5.2: Vehicle parameters for the HCM results analysis.

Symbol	Value	Proportion
L	2.6 $[m]$	$1.04 \cdot L_{ref}$
b_1	1.062 $[m]$	$0.85 \cdot b_{1,ref}$
b_2	1.25 $[m]$	$1.23 \cdot b_{2,ref}$
m_s	600 $[kg]$	$m_{s,ref}$
I_y	1100 $[kg \cdot m^2]$	$I_{y,ref}$
m_f	26 $[kg]$	$0.65 \cdot m_{f,ref}$
m_r	56 $[kg]$	$1.40 \cdot m_{r,ref}$
k_{tf}	105 $[kN/m]$	$0.95 \cdot k_{tf,ref}$
k_{tr}	121 $[kN/m]$	$1.10 \cdot k_{tr,ref}$
$k_{f,QCM,J_1} = k_{f,HCM,J_1}$	2420 $[N/m]$	$[-]$
$k_{r,QCM,J_1} = k_{r,HCM,J_1}$	3502 $[N/m]$	$[-]$
c_{f,QCM,J_1}	123.3 $[Ns/m]$	$[-]$
c_{r,QCM,J_1}	204.4 $[Ns/m]$	$[-]$
c_{f,HCM,J_1}	182.2 $[Ns/m]$	$1.48 \cdot c_{f,QCM,J_1}$
c_{r,HCM,J_1}	207.5 $[Ns/m]$	$1.01 \cdot c_{f,QCM,J_1}$
k_{f,QCM,J_2}	9058 $[N/m]$	$[-]$
k_{r,QCM,J_2}	14246 $[N/m]$	$[-]$
c_{f,QCM,J_2}	1417 $[Ns/m]$	$[-]$
c_{r,QCM,J_2}	2089 $[Ns/m]$	$[-]$
k_{f,HCM,J_2}	8497 $[N/m]$	$0.94 \cdot k_{f,QCM,J_2}$
k_{r,HCM,J_2}	14944 $[N/m]$	$1.05 \cdot k_{r,QCM,J_2}$
c_{f,HCM,J_2}	1440 $[Ns/m]$	$1.02 \cdot c_{f,QCM,J_2}$
c_{r,HCM,J_2}	2125 $[Ns/m]$	$1.02 \cdot c_{f,QCM,J_2}$

Figure 5.11 shows the variation of the comfort index as a function of speed. The goal is to compare how comfort varies with speed when using a suspension optimized with the HCM at a speed of 25 $[m/s]$, compared to a suspension optimized using the QCM.

The Root Mean Square (RMS) value of the system's vibratory response, utilized for performance indicators J_1 and J_2, is theoretically proportional to the square root of the vehicle's forward velocity ($\sqrt{V_x}$). This relationship stems from the road input model, where the road velocity Power Spectral Density (G_{vv}) scales linearly with V_x (as discussed in Chapter 2), and the RMS response is derived from the integral of the output PSD, which is influenced by $\sqrt{G_{vv}}$. Consequently, plotting J_1 or J_2 directly against parameters at varying speeds can result in graphs where the dominant $\sqrt{V_x}$ trend obscures the underlying influence of the

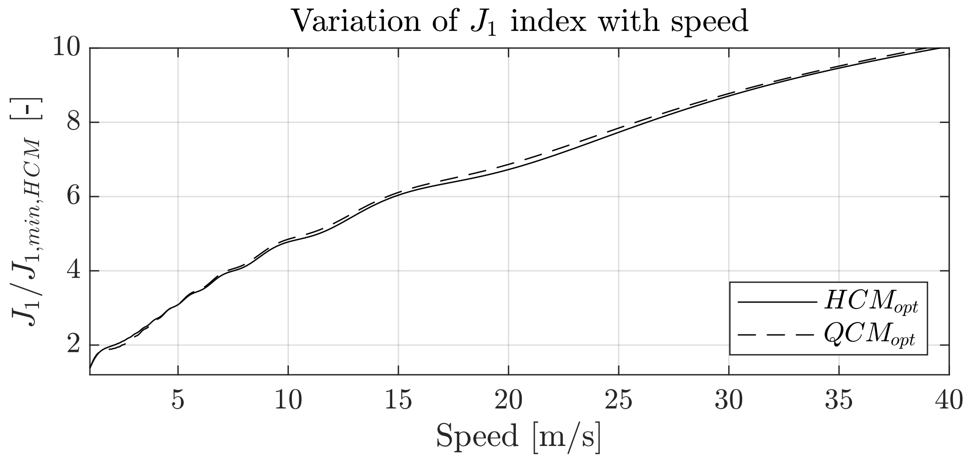

Figure 5.11: Variation of the comfort index J_1 as a function of speed. The solid line represents the variation of J_1 using the optimal parameters from the HCM at a speed of 25 $[m/s]$, while the dashed line shows the variation of J_1 using the QCM optimal parameters.

suspension parameters being investigated, an effect illustrated in Figure 5.11. To mitigate this scaling effect and enhance visualization, the performance indicators presented in Figures 5.12 and 5.13 (and subsequent relevant analyses throughout this chapter) have been normalized by dividing by $1/\sqrt{V_x}$. This normalization allows for a clearer representation and comparison of how suspension parameters affect comfort and road holding, independent of the primary speed dependency.

A significant difference in magnitude is observed between the two performance indicators. The comfort indicator shows variations of approximately 20%, while the road-holding indicator exhibits minimal differences, on the order of 0.5%, as a function of speed. For speeds greater than 10 $[m/s]$, the use of the HCM with time delay results in a 2% reduction in acceleration magnitudes compared to the QCM.

The road-holding indicator displays even smaller variations, reducing the variation in contact force by approximately 0.01%. This small variation is attributed to the time delay, which models the effect of applying an external force to the front axle first, followed by the rear axle after a time interval t_d. This phenomenon predominantly affects the pitch vibration mode of the vehicle and consequently the comfort indicator, while having limited physical relevance to the road-holding indicator, as reflected in its low sensitivity to the inclusion of the time delay.

Although the suspension optimization using the HCM brings measurable improvements, their

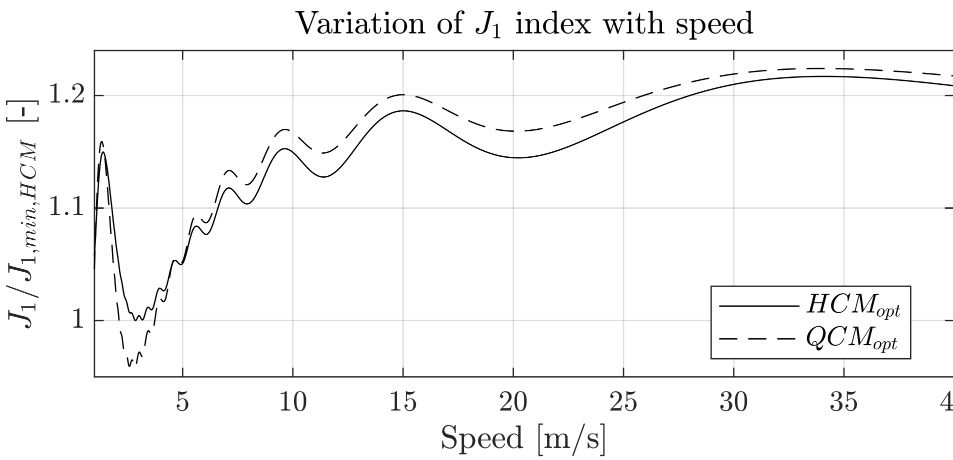

Figure 5.12: Variation of the comfort index J_1 as a function of speed. The solid line represents the variation of J_1 using the optimal parameters from the HCM at a speed of 25 $[m/s]$, while the dashed line shows the variation of J_1 using the QCM optimal parameters. Both outputs are scaled by $1/\sqrt{V_x}$ to avoid the velocity-dependent factor obscuring the differences between the two models.

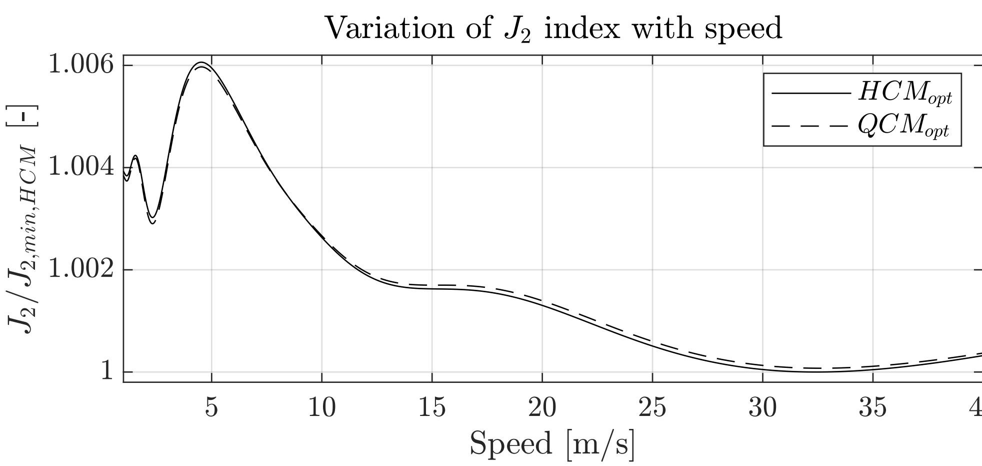

Figure 5.13: Variation of the comfort index J_2 as a function of speed. The solid line represents the variation of J_2 using the optimal parameters from the HCM at a speed of 25 $[m/s]$, while the dashed line shows the variation of J_2 using the QCM optimal parameters. Both outputs are scaled by $1/\sqrt{V_x}$ to avoid the velocity-dependent factor obscuring the differences between the two models.

magnitude is so small (at least for this vehicle) that other factors, such as the accurate determination of lumped parameters or the consideration of nonlinearities, could have a greater impact on the overall system performance.

To assess whether the reduction in performance indicators is significant, the effects of varying both the suspended mass and the vertical stiffness of the tires are analyzed. Changes in suspended mass simulate scenarios like variations in passenger count or fuel levels, while adjustments to tire vertical stiffness model the effect of slightly deflated tires. These analyses aim to quantify whether the performance gains achieved through HCM optimizations over the QCM are as significant as accurate parameter measurements.

In Figure 5.14, the variation in performance indicators is presented for a case where the suspended mass is reduced by 40 $[kg]$, while maintaining the optimization based on the HCM described in Table 5.2.

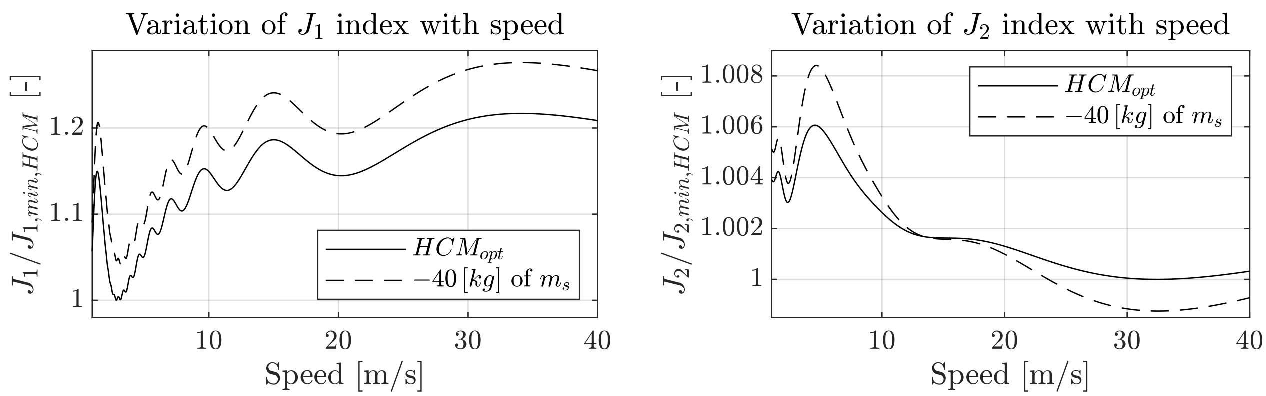

(a) Variation of J_1 index as a function of speed. **(b)** Variation of J_2 index as a function of speed.

Figure 5.14: Variation of performance indicators with speed for a case where the suspended mass is reduced by 40 [kg]. The solid line represents the variation using the optimal parameters of the HCM, while the dashed line corresponds to the configuration with reduced suspended mass.

In the case of the comfort indicator, an increase of approximately 4% in accelerations is observed across the entire speed range, following a trend similar to the baseline case. On the other hand, the road-holding indicator exhibits a different behavior, showing not only changes in the magnitude of the indicator but also variations in its trend with respect to speed. Zones are identified where the indicator increases and others where it decreases compared to the baseline case. When comparing these variations with those produced by the QCM optimization, it is concluded that, for comfort, the magnitudes are similar. However, for the road-holding indicator, the variations are significantly larger. This underscores the importance of accurate vehicle parameterization over the complexity of the model employed.

Continuing the analysis of the effects of changes in vehicle hyperparameters, Figure 5.15 illustrates the variation in performance indicators under a 15% reduction in the vertical stiffness of the tires, representing a scenario of slightly deflated tires.

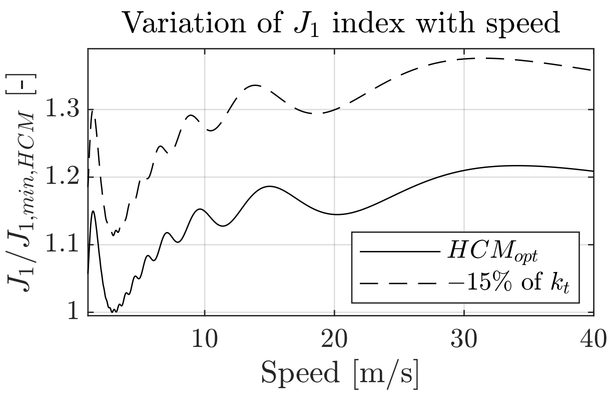

(a) Variation of J_1 index as a function of speed.

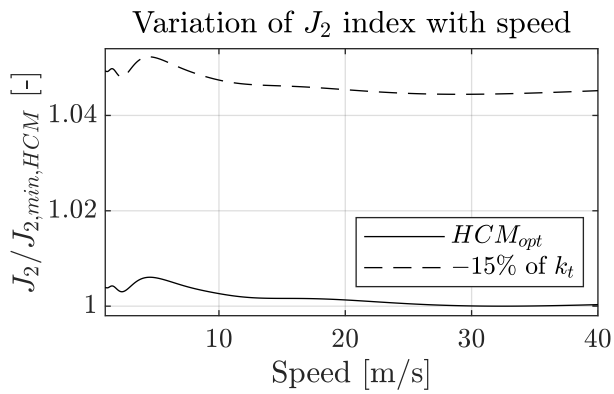

(b) Variation of J_2 index as a function of speed.

Figure 5.15: Variation of performance indicators with speed for a case where the tire stiffness is reduced 15%. The solid line represents the variation using the optimal parameters of the HCM, while the dashed line corresponds to the configuration with reduced tire stiffness.

For both performance indicators, similar trends are identified, showing nearly invariant contour curves. This result reinforces the previous conclusion, indicating that accurate vehicle parametrization is more critical than relying on more complex optimization models, especially for the road-holding indicator, which was shown to be less sensitive to time delay effects.

In general, across all analyzed cases, it was observed that although the optimal coefficients of the QCM deviate slightly (never more than 5%) from those of the HCM, this deviation does not result in significant differences in the performance indicators. Instead, a representative parametrization of the vehicle in the lumped-parameter model plays a far more dominant role.

5.4 Summary

This chapter analyzed the two-axle Half Car Model (HCM), incorporating pitch dynamics and inter-axle interaction through time-delayed road inputs ($t_d = L/V_x$). Due to the analytical intractability of the model—particularly in the presence of time delay—three vehicle configurations with different input correlation types were examined. Using covariance analysis, the optimal suspension parameters (k_f, k_r, c_f, c_r) were determined for both comfort

(J_1) and road holding (J_2).

The first two cases, involving simultaneous inputs, showed that the optimal values obtained from the *QCM* also satisfy this *HCM* configuration, even under certain asymmetric parameter conditions (see **Section 5.2.2**). In these scenarios, analytical solutions were deemed unnecessary, and also supports the arbitrary approach adopted to quantify comfort and road holding in the *HCM*.

In the third case, which included time delay in a symmetric vehicle, small differences emerged between the *QCM* and *HCM* optimal values. Unexpectedly, asymmetric optimal configurations appeared despite vehicle symmetry, and a dependency on vehicle speed was observed. For road holding, the results aligned with existing design recommendations on axle ride frequencies, providing a mathematical basis for previously qualitative guidelines.

Finally, a sensitivity analysis revealed larger discrepancies between the optimal parameters of the *QCM* and *HCM*. While comfort improvements of approximately 2% were achieved, road-holding gains remained minimal (around 0.01%). These results suggest that accurate parameterization of the lumped model plays a more decisive role in suspension optimization than the level of model complexity.

Chapter 6

Conclusion

This thesis presented the application of covariance analysis to Half-Car Models (HCM) to determine optimal suspension coefficients aimed at enhancing ride comfort and road holding, modeling the road profile as a white noise disturbance. A primary objective was the development of analytical expressions for these optimal coefficients, specifically incorporating the influence of an anti-roll bar as an interconnection element. The key findings and conclusions derived from this investigation are summarized below.

For the Quarter Car Model, covariance analysis was successfully employed to analytically derive algebraic expressions for the *RMS* vertical acceleration (comfort metric, J_1) and the *RMS* dynamic tire load variation (road holding metric, J_2). A comparative evaluation of time-domain (covariance) and frequency-domain (*PSD*) analysis methods was performed to assess their suitability for extension to the *HCM*. It was concluded that covariance analysis best aligns with the objectives of this investigation.

Regarding the application of covariance analysis to the Half-Car Model, two primary configurations were investigated. First, for the single-axle HCM, an analytical solution to the optimization problem was successfully derived taking into account an anti-roll bar. Second, for the two-axle HCM, it was found that obtaining a fully analytical solution is impractical due to the system's complexity, thus requiring simplifying assumptions or the use of a numerical approach.

For the single-axle *HCM* with ARB, novel analytical expressions were derived for the performance indicators (J_1, J_2) and optimal suspension parameters ($k_s^\star$, $c_s^\star$), under the assumption of uncorrelated road inputs. The results shown that incorporating an ARB significantly alters the optimal suspension design. Specifically, for comfort requires higher damping (c_s) compared to the QCM. While for road holding, it requires slightly high damper, and lower spring stiffness (k_s) to re-optimize performance.

Concerning the general impact of ARBs, the literature extensively documents that ARBs reduce ride comfort (J_1) to improve roll stability, this research makes a notable contribution by demonstrating they also degrade road-holding performance (J_2) under straight-line conditions. Thus, while an anti-roll bar improves the vehicle's performance when cornering, the automotive design process should be aware that it also consistently degrades its performance during straight-line motion.

For the two-axle HCM, scenarios with simultaneous in-phase inputs showed that the optimal coefficients of the QCM also apply to the HCM, both for symmetric vehicles and for those with defined asymmetries. While not a new finding, this result support the extrapolation of principles from the 2-oF SISO model to the 4-oF MIMO framework and supported the performance indicators adopted in the HCM formulation.

However, when introducing a time delay between the front and rear axle inputs (a more realistic scenario), the optimal coefficients for the two-axle *HCM* deviated from the *QCM* predictions. For the comfort indicator (J_1), differences in optimal damping coefficients reached up to 40%, whereas road-holding (J_2) optima showed smaller deviations (around 5%). Optimising using the 4-*DOF* time-delay model yielded noticeable reductions in predicted driver accelerations compared to using *QCM* parameters. Nonetheless, the magnitude of these improvements was found to be comparable to the potential impact of uncertainties in vehicle parameterization.

For the road-holding indicator specifically, the performance improvements gained by using *HCM*-derived optimal values (over *QCM* values) were minimal in the time-delay case, at least for the parameter sets analyzed. Interestingly, the time-delay results provided a quantitative basis supporting certain design guidelines regarding relative axle ride frequencies. Ultimately, for road-holding optimization, the accurate determination of the vehicle's lumped parameters appears more critical than transitioning from the *QCM* to the more complex *HCM*.

As a next step, this optimization framework could be verified through numerical simulation in a dedicated software environment. Such a study would serve to support the representativeness of the proposed models under less idealized conditions, bridging the gap between theoretical optimization and real-world application.

Bibliography

(2006). *Tyre and Vehicle Dynamics*.

Baumal, A., McPhee, J., & Calamai, P. (1998). Application of genetic algorithms to the design optimization of an active vehicle suspension system. *Computer Methods in Applied Mechanics and Engineering*, *163*, 87–94.

Bavafa-Toosi, Y. (2017). *Introduction to Linear Control Systems*. Elsevier Science.

Bideleh, S. M. M., Berbyuk, V., & Persson, R. (2016). Wear/comfort Pareto optimisation of bogie suspension. *Vehicle System Dynamics*, *54*, 1053–1076.

Chen, Y., Peterson, A. W., & and, M. A. (2019). Achieving anti-roll bar effect through air management in commercial vehicle pneumatic suspensions. *Vehicle System Dynamics*, *57*, 1775–1794. arXiv:https://doi.org/10.1080/00423114.2018.1552005.

Drehmer, L. R. C., Casas, W. J. P., & and, H. M. G. (2015). Parameters optimisation of a vehicle suspension system using a particle swarm optimisation algorithm. *Vehicle System Dynamics*, *53*, 449–474. arXiv:https://doi.org/10.1080/00423114.2014.1002503.

Frömmig, L. (2023). *Basic Course in Race Car Technology*. Springer Nature.

Gandhi, P., Adarsh, S., & Ramachandran, K. (2017). Performance Analysis of Half Car Suspension Model with 4 DOF using PID, LQR, FUZZY and ANFIS Controllers. *Procedia Computer Science*, *115*, 2–13.

Georgiou, G., Verros, G., & Natsiavas, S. (2007). Multi-objective optimization of quarter-car models with a passive or semi-active suspension system. *Vehicle System Dynamics*, *45*, 77–92.

Gobbi, M., Haque, I., Papalambros, P. Y., & Mastinu, G. (2005). Optimization and integration of ground vehicle systems. *Vehicle System Dynamics*, *43*, 437–453.

GOBBI, M., & MASTINU, G. (2001). Analytical description and optimization of the dynamic behaviour of passively suspended road vehicles. *Journal of Sound and Vibration*, *245*, 457–481.

Gobbi, M., Mastinu, G., & Doniselli, C. (1999a). Optimising a Car Chassis. *Vehicle System Dynamics*, *32*, 149–170.

Gobbi, M., Mastinu, G., Doniselli, C., Guglielmetto, L., & Pisino, E. (1999b). Optimal amp; Robust Design of a Road Vehicle Suspension System. *Vehicle System Dynamics*, *33*, 3–22.

Gosselin-Brisson, S., Bouazara, M., & Richard, M. (2009). Design of an active anti-roll bar for off-road vehicles. *Shock and Vibration*, *16*, 155–174.

Green, M., & Limebeer, D. J. N. (2012). *Linear robust control*. Courier Corporation.

Guiggiani, M. (2014). *The Science of Vehicle Dynamics: Handling, Braking, and Ride of Road and Race Cars*.

Hassan, M., Elsayed, A., El-Souhily, B., Elgamal, H., & Elshabasy, M. M. (2023). Investigating the effect of augmenting the anti-roll-bar with a torsional-dynamic-absorber on the handling-stability and the ride-comfort of the off-road-vehicles. *Alexandria Engineering Journal*, *81*, 29–45.

ISO (1997). *International Standard ISO 2631-1*.

Jazar, R. N. (2008). *Vehicle Dynamics: Theory and Application*.

Jonasson, M., & Roos, F. (2008). Design and evaluation of an active electromechanical wheel suspension system. *Mechatronics*, *18*, 218–230.

Kaldas, M. M., & Soliman, A. (2014). Influence of active suspension preview control on vehicle ride and braking performance. *Submitted to SAE World Congress*, *7*.

Karnopp, D. (2013). *Vehicle Dynamics, Stability, and Control*.

Kreyszig, E. (2010). *Advanced Engineering Mathematics*. John Wiley Sons.

Kumar, Y., Siddiqui, R. A., Upadhyay, Y., & Prajapati, S. (2021). Kinematic and Structural Analysis of Independent type suspension system with Anti-Roll bar for Formula Student Vehicle. *Materials Today Proceedings*, *56*, 2672–2679.

Le, K. C., & Pieper, A. (2014). Damping of roll vibration of vehicle suspension. *Vehicle System Dynamics*, *52*, 562–579.

Limebeer, D. J. N., & Massaro, M. (2018). *Dynamics and Optimal Control of Road Vehicles*.

Lot, R., & Sadauckas, J. (2021). *Motorcycle design*. Roberto Lot.

Lu, Y., Huang, Y., Zhen, R., Yue, Z., Pazooki, A., Soltani, A., Sun, C., & Khajepour, A. (2024). Modelling and experimental validation of an adaptive interconnected suspension with adjustable roll stiffness (AIS-ARS). *Vehicle System Dynamics*, (pp. 1–19).

Maplesoft (2024). Maple. Computer software for symbolic and numeric computation, visualization, and modeling.

Milliken, W. F., & Milliken, D. L. (1994). *Race car vehicle dynamics*.

Múčka, P., Stein, G. J., & Tobolka, P. (2019). Whole-body vibration and vertical road profile displacement power spectral density. *Vehicle System Dynamics*, *58*, 630–656.

Müller, P., & Schiehlen, W. (2012). *Linear vibrations*. Springer Science Business Media.

Popp, K., & Schiehlen, W. (2010). *Ground vehicle dynamics*. Springer Science Business Media.

Pütz, R., & Serné, T. (2022). *Race car handling Optimization*.

Ramakrishna, S., Reddy, B., Akhil, B., & Kumar, B. (2017). A review on anti-roll bar used in locomotives and vehicles, . *7*.

Robson, J. D., & Kamash, K. M. A. (1977). Road Surface Description in Relation to Vehicle Response. *Vehicle System Dynamics*, *6*, 153–157.

Scheibe, F., & Smith, M. C. (2009). Analytical solutions for optimal ride comfort and tyre grip for passive vehicle suspensions. *Vehicle System Dynamics*, *47*, 1229–1252.

Segers, J. (2014). *Analysis Techniques for Racecar Data Acquisition - Second Edition*.

Sherman, M. (2011). *Spatial Statistics and Spatio-Temporal Data*. John Wiley Sons.

Slotine, J., & Li, W. (1991). *Applied Nonlinear Control*. Prentice Hall.

Smith, W. A., Zhang, N., & and, J. J. (2010). Hydraulically interconnected vehicle suspension: theoretical and experimental ride analysis. *Vehicle System Dynamics*, *48*, 41–64. `arXiv:https://doi.org/10.1080/00423110903243190`.

Standardization, I. O. F. (1995). *ISO 8608 : Mechanical Vibration, Road Surface Profiles, Reporting of Measured Data*.

Standarization, I. O. F. (2001). *International Standard ISO 2631-4: Mechanical vibration and shock — Evaluation of human exposure to whole-body vibration*.

Tan, B., Wang, S., Zhang, B., Li, B., Zhang, N., & and, H. Q. (2022). Sensitivity stratification concept and hierarchical multi-objective optimisation for an ambulance with hydraulically interconnected suspension and stretcher-human body model. *Vehicle System Dynamics*, *60*, 540–568. `arXiv:https://doi.org/10.1080/00423114.2020.1823432`.

Trzesniowski, M. (2023). *Suspension system*.

Wang, Z., Dong, M., Qin, Y., Du, Y., Zhao, F., & Gu, L. (2017). Suspension system state estimation using adaptive kalman filtering based on road classification. *Vehicle System Dynamics*, *55*, 371–398.

Wijker, J. (2009). *Random Vibrations in Spacecraft Structures Design: Theory and Applications*. Solid Mechanics and Its Applications. Springer Netherlands.

Wijker, J. (2018). *Miles' Equation in Random Vibrations: Theory and Applications in Spacecraft Structures Design*. Solid Mechanics and Its Applications. Springer International Publishing.

Xu, G., Zhang, N., & and, H. M. R. (2015). Roll and pitch independently tuned interconnected suspension: modelling and dynamic analysis. *Vehicle System Dynamics*, *53*, 1830–1849. `arXiv:https://doi.org/10.1080/00423114.2015.1103375`.

Yaghoubi, S., & Ghanbarzadeh, A. (2024). Modeling and optimization of car suspension system in the presence of magnetorheological damper using simulink-pso hybrid technique. *Results in Engineering*, *22*, 102065.

Zhang, N., Smith, W., & Jeyakumaran, J. (2010). Hydraulically interconnected vehicle suspension: Background and modelling. *Vehicle System Dynamics - VEH SYST DYN*, *48*, 17–40.

Zhao, L., Zhou, C., Yu, Y., & and, F. Y. (2016). Hybrid modelling and damping collaborative optimisation of five-suspensions for coupling driver-seat-cab system. *Vehicle System Dynamics*, *54*, 667–688. `arXiv:https://doi.org/10.1080/00423114.2016.1151902`.

Appendix A

Analytical covariance analysis to the two axle Half Car Model

This appendix details the attempt made to find a purely analytical solution to the Lyapunov equation for the two-axle Half Car Model, specifically focusing on the first scenario considered in Chapter 5: In-phase road inputs (zero time lag, $t_d = 0$). As will be shown, obtaining a manageable closed-form solution proved infeasible using the direct algebraic method.

As established previously, for this 4 degree of freedom (oF) system, the state space representation results in an 8×8 state matrix A, and the Lyapunov equation becomes a matrix equation of the same dimension. For the zero-lag scenario ($t_d = 0$), the white noise intensity matrix corresponds to $R_w(0)$ (Eq. (5.18)), and the right-hand side of the Lyapunov equation simplifies due to the sparsity of the input matrix columns b_1 and b_2 (forming $B = [b_1\ b_2]$). Specifically, the only non-zero elements in the resulting 8×8 right hand side matrix are:

$$-BR_wB^T{}_{55} = -q_{\dot{r}}\frac{k_{tf}^2}{m_f^2} \quad -BR_wB^T{}_{66} = -q_{\dot{r}}\frac{k_{tr}^2}{m_r^2} \quad -BR_wB^T{}_{56} = -BR_wB^T{}_{65} = -q_{\dot{r}}\frac{k_{tf}k_{tr}}{m_f m_r} \tag{A.1}$$

where $q_{\dot{r}} = 2\pi G_{vv} V_x$.

On the other hand, the left-hand side of the Lyapunov equation involves the 8×8 state matrix A and the unknown 8×8 symmetric covariance matrix $P_{\dot{x}}$. The state matrix is derived from the system matrices M, C, K (defined in Chapter 5) as :

$$
A=\begin{bmatrix}
0 & 0 & 0 & 0 & 1 & 0 & 0 & 0 \\
0 & 0 & 0 & 0 & 0 & 1 & 0 & 0 \\
0 & 0 & 0 & 0 & 0 & 0 & 1 & 0 \\
0 & 0 & 0 & 0 & 0 & 0 & 0 & 1 \\
-\frac{k_{tf}+k_f}{m_f} & 0 & \frac{k_f}{m_f} & -\frac{bk_f}{m_f} & -\frac{c_f}{m_f} & 0 & \frac{c_f}{m_f} & -\frac{bc_f}{m_f} \\
0 & -\frac{k_{tr}+k_r}{m_r} & \frac{k_r}{m_r} & \frac{ak_r}{m_r} & 0 & -\frac{c_r}{m_r} & \frac{ac_r}{m_r} & -\frac{ac_r}{m_r} \\
\frac{k_f}{m_s} & \frac{k_r}{m_s} & -\frac{k_f+k_r}{m_s} & -\frac{b_1k_r-b_2k_f}{m_s} & \frac{c_f}{m_s} & \frac{c_r}{m_s} & -\frac{c_f+c_r}{m_s} & -\frac{b_1c_r-b_2c_f}{m_s} \\
-\frac{b_2k_f}{I_y} & \frac{b_1k_r}{I_y} & -\frac{b_1k_f-b_2k_f}{I_y} & -\frac{b_2^2k_r+b_1^2k_f}{I_y} & -\frac{b_2c_f}{I_y} & \frac{b_1c_r}{I_y} & -\frac{b_1c_f-b_2c_f}{I_y} & -\frac{b_2^2c_r+b_1^2c_f}{I_y}
\end{bmatrix}
\tag{A.2}
$$

The covariance matrix contains 64 elements (P_{ij}), though only 36 are unique due to symmetry.

Performing the algebraic operations for the left hand side, $AP_{\dot{x}} + P_{\dot{x}}A^T$, yields expressions involving the unknown P_{ij} terms. As discussed in Chapter 5, obtaining the performance indicators (Eqs. (5.12), (5.14), (5.15)) requires solving for specific elements of $P_{\dot{x}}$. To achieve this analytically, the direct method was employed.

The direct method transforms the 8th-order matrix Lyapunov equation into an equivalent system of $n(n+1)/2 = 36$ linear algebraic equations for the unique elements of $P_{\dot{x}}$, represented as $\hat{A}_{36\times36} \cdot \hat{x}_{36\times1} = \hat{b}_{36\times1}$. Attempting to solve this system directly using the symbolic computation software Maple™yielded an intermediate symbolic solution approximately 2.6 billion characters in length, which is clearly intractable for deriving meaningful analytical expressions.

To proceed, system reduction techniques were necessary. Observing the sparsity pattern of the coefficient matrix $\hat{A}_{36\times36}$ (illustrated schematically in Figure A0.1) and noting that the system is nearly homogeneous (most elements of $\hat{b}_{36\times1}$ are zero, derived from the sparse right hand side Eq. (A.1)), a substitution method was implemented to simplify the system.

The substitution method involves iteratively solving one equation for a specific unknown (P_{ij})

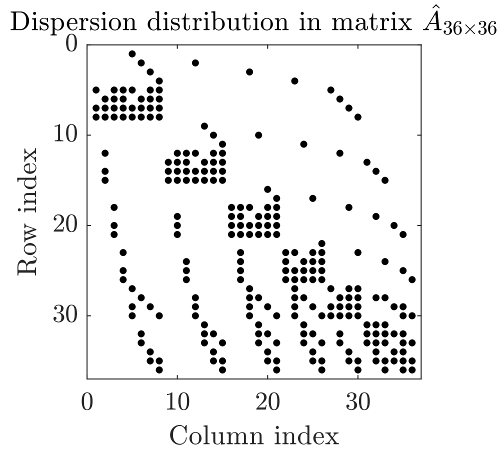

Figure A0.1: Schematic representation of the sparsity pattern in the coefficient matrix $\hat{A}_{36\times 36}$ arising from the direct method applied to the Lyapunov equation. The predominance of white space highlights the sparse nature, where most elements are zero.

and substituting this expression into the remaining equations. Leveraging the homogeneity of most equations (equated to zero), each equation can be multiplied or divided by common factors or constants during the process, aiming to simplify expressions and reduce the overall character count of the symbolic representation. A custom algorithm implementing this symbolic substitution and simplification strategy was developed in Maple™.

Applying this methodology, the original 36×36 system was successfully reduced to a 26×26 linear system, $\hat{A}_{26\times 26}\hat{x}_{26\times 1} = \hat{b}_{26\times 1}$. The density distribution of the resulting coefficient matrix $\hat{A}_{26\times 26}$ is depicted in Figure A0.2.

Solving this 26×26 system in Maple™still resulted in excessively large symbolic expressions (approximately 200 million characters). Although representing progress, this remained impractical for deriving usable analytical formulas. Therefore, the symbolic substitution and simplification process was continued iteratively until the system was further reduced to an 8×8 system, $\hat{A}_{8\times 8}\hat{x}_{8\times 1} = \hat{b}_{8\times 1}$. During this reduction, while the number of equations decreased, the density of the coefficient matrix and the complexity (character count) of its individual components generally increased. Equation (A.3) schematically represents the 8×8 system structure, where the matrix entries indicate the approximate symbolic character count for each corresponding element in $\hat{A}_{8\times 8}$ and the non-zero elements in $\hat{b}_{8\times 1}$. An example of one complex component ($\hat{A}_{8\times 8,(5,2)}$) is given in Equation (A.4). Figure A0.3 illustrates the

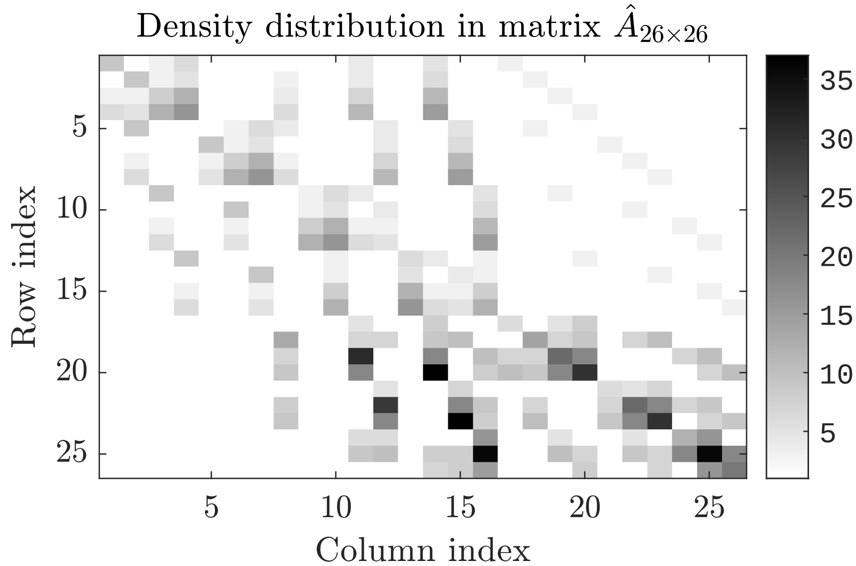

Figure A0.2: Density distribution visualization for the reduced coefficient matrix $\hat{A}_{26\times26}$. The grayscale intensity may represent the magnitude or complexity (e.g., character count) of the non-zero elements, showing increased density compared to the initial sparse matrix.

density pattern of the final $\hat{A}_{8\times8}$ matrix.

$$\begin{bmatrix} 5325 & 101 & 4297 & 4718 & 4230 & 3034 & 4005 & 4199 \\ 4225 & 1 & 3154 & 2810 & 3479 & 1918 & 2397 & 3178 \\ 6340 & 102 & 5615 & 5657 & 5410 & 3912 & 4634 & 4810 \\ 4415 & 1 & 3377 & 3210 & 3525 & 2041 & 2755 & 3555 \\ 8030 & 136 & 7108 & 6802 & 7070 & 5128 & 6085 & 6150 \\ 2279 & 71 & 1681 & 1886 & 1705 & 1091 & 1424 & 1619 \\ 1554 & 1 & 1111 & 1000 & 1084 & 621 & 827 & 837 \\ 22 & 1 & 20 & 1 & 1 & 1 & 1 & 1 \end{bmatrix} \begin{bmatrix} P_{36} \\ P_{44} \\ P_{46} \\ P_{47} \\ P_{67} \\ P_{68} \\ P_{77} \\ P_{78} \end{bmatrix} = \begin{bmatrix} 1 \\ 1 \\ 1 \\ 1 \\ 1 \\ 1 \\ 13 \\ 13 \end{bmatrix} \tag{A.3}$$

$$\hat{A}_{8\times8_{52}} = \frac{(a+b)^2(k_{tr}+k_r)k_r\left(\left(a\left(k_{tf}+k_f\right)k_r - bk_fk_{tf}\right)k_{tr} - bk_fk_rk_{tf}\right)k_{tf}k_fk_{tr}}{\left(\left(\left(k_{tf}+k_f\right)k_r + k_fk_{tf}\right)k_{tr} + k_fk_rk_{tf}\right)^2} \tag{A.4}$$

A final attempt was made to solve this reduced 8×8 system symbolically in Maple™. However, the computation could not be completed due to excessive memory requirements (exhausting 16 GB of available RAM) and impractically long processing times (exceeding eight days of continuous computation). This outcome, combined with the observed complexity of the

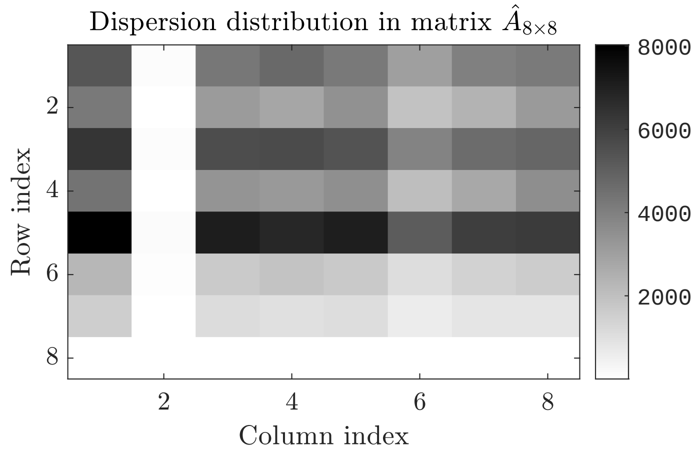

Figure A0.3: Density distribution visualization for the reduced coefficient matrix $\hat{A}_{8\times8}$. The grayscale gradient likely represents the character count or complexity of the components, showing a dense matrix with complex terms.

matrix components even in the reduced systems (e.g., Eq. (A.4)), strongly indicates that obtaining a manageable, closed-form analytical solution for the covariance matrix elements (and thus the optimal suspension parameters) for the two-axle HCM using this direct algebraic approach is not feasible with current symbolic computation capabilities and standard hardware. Consequently, deriving an analytical solution would necessitate significant model simplification, or alternatively, adopting the numerical approach pursued in Chapter 5.

Appendix B

Two identical inputs with a time delay and asymmetrical weight distribution

Figure B0.1 illustrates the variation of the comfort indicator for the vehicle parameters defined in Table 5.2, considering different damping coefficients c_f and c_r at a speed of 25 $[m/s]$. Similarly, Figure B0.2 shows the variation of the road-holding indicator for the same vehicle parameters, also defined in Table 5.2, considering different suspension parameters k_f, k_r, c_f, and c_r at a speed of 25 [m/s].

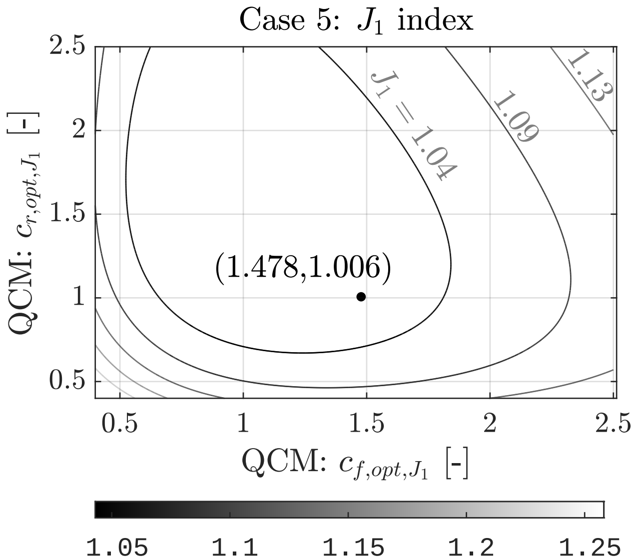

Figure B0.1: Variation of optimal damping coefficients c_f and c_r as a function of speed for the comfort index (J_1). The analysis highlights the asymmetric behavior of the damping coefficients, with c_f generally being higher than c_r.

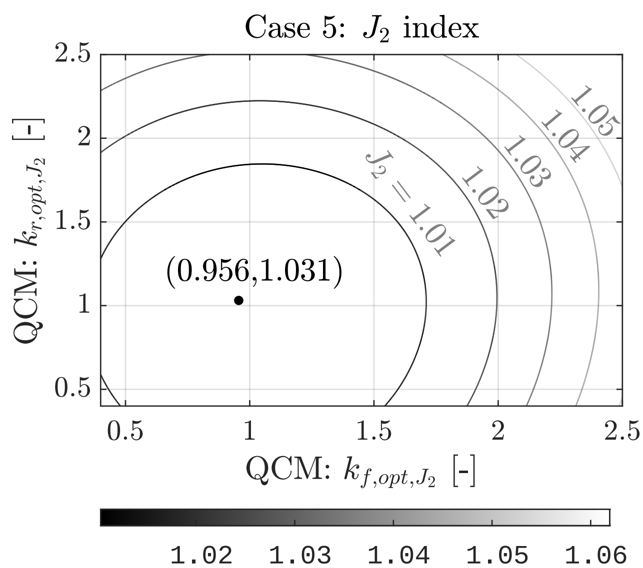

(a) J_2 index as a function of k_f and k_r, using the optimal damping coefficients of the QCM.

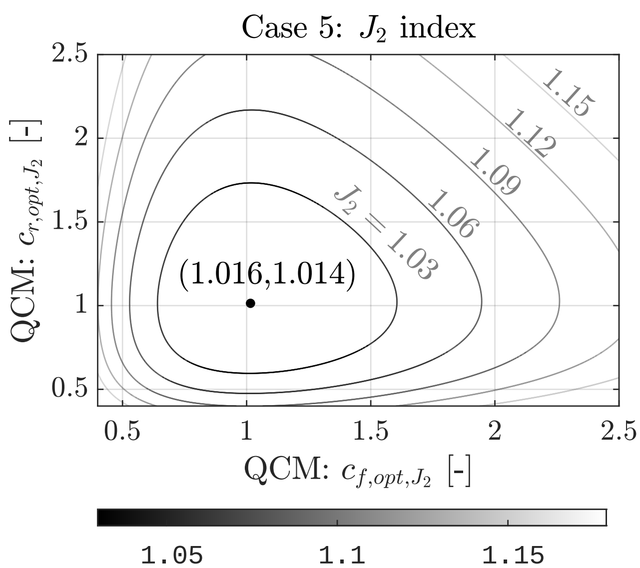

(b) J_2 index as a function of c_f and c_r, using the optimal stiffness coefficients of the QCM.

Figure B0.2: Variation of the J_2 index for different combinations of stiffness (k_f, k_r) and damping (c_f, c_r) coefficients under symmetrical weight distribution and two identical inputs with time delay. The gray scale gradient indicates the optimal parameter combinations, with the darkest point representing the global minimum.